

UNIVERSITY OF NAPLES FEDERICO II



DEPARTMENT OF PHARMACY

PhD program in Pharmaceutical Sciences

**Targeting cancer with inorganic multifunctional
nanoparticles**

**PhD Student
Chiara Tramontano**

**Coordinator
Prof. Rosaria Meli**

**Tutor
Prof. Nicola Borbone
Dr. Ilaria Rea**

XXXV CYCLE (2019-2022)

*“The real voyage of discovery consists
not in seeing new insights
but looking with new eyes”*

Marcel Proust

*“Il vero viaggio di scoperta non consiste
nel cercare nuove terre,
ma nell’aver nuovi occhi.”*

*Marcel Proust,
free translation*

Abstract

Treating cancer disease is an enormous challenge, especially when metastases outbreak the primary tumor site spreading to many different organs, either sequentially or synchronously. The majority of the currently available anti-cancer drugs target physiological pathways that are upregulated in cancer, among whom the transforming growth factor (TGF) and protein death (PD) receptor/ligand-mediated signaling. These proteins are actively involved in physiological functions, such as cell proliferation, differentiation, migration, adhesion, and apoptosis. The attack of physiological pathways by traditional anti-cancer drugs often results in unspecific and distressing treatments, painful side effects, and poor quality of life. Therefore, it is of utmost importance to develop novel treatments targeting the cancer microenvironment and improving therapeutic outcomes. Over the years, nanoparticles (NPs) emerged with great potential to carry and deliver anti-cancer drugs (*i.e.*, small molecules, proteins, oligonucleotides) in a precisely tuned and controllable manner. The encapsulation of NPs in polymers exhibiting a pH and *stimuli*-responsive dissolution has been shown to enable delivering drugs upon exposure to specific *stimuli* in cancer cells. Among the inorganic nanocarriers, diatomite NPs (DNPs) have secured their seat in the race of nanomedicine due to their porosity, cost-effective production from diatoms, biocompatibility and, nonetheless, ease of surface functionalization. DNPs with a mean size of 400 nm are obtained by ultrasonication of the diatom frustules, which are composed of mesoporous biosilica considered safe by the food and drug administration. Thus, the increasing knowledge of DNPs' surface chemistry has contributed to the

development of hybrid DNPs exhibiting multifunctional features, among whom drug delivery and biosensing are the main purposes. The combination of the plasmonic features of gold NPs (AuNPs) with the drug-loading capacity of DNPs allows for the design of hybrid nanosensors for the real-time quantification of intracellular drug release and dose-response correlation studies. The opportunity to attach antibodies on the surface of drug-loaded DNPs allows for targeting cancer cells expressing specific surface antigens, thus increasing the local accumulation of the drug and reducing the likelihood of side effects. Furthermore, the blast of microfluidic approaches already used for the mass production of nanotherapeutics has shed a light on the potentiality of DNPs as oral nanocarriers for the treatment of colorectal cancer.

The following dissertation describes the development of DNPs designed *ad hoc* to load and deliver anti-cancer drugs in cancer cells with release profiles controlled by *stimuli*-responsive polymeric coatings. The successful delivery of the TGF- β inhibitor galunisertib from gelatin-covered DNPs is demonstrated in multiple CRC cell lines, showing the enhanced antimetastatic effect of the delivered drug compared to conventional approaches. The decoration of DNPs with AuNPs allows for the quantification of released galunisertib in CRC cells with a sub-femtogram scale resolution by surface-enhanced Raman scattering, outlining the potentiality of hybrid DNPs as both nanocarriers and nanosensors. Furthermore, the plasmonic properties of hybrid DNPs are exploited for the design of a theoretical model for the estimation of polymer coating thicknesses on the DNPs, exceeding the shortcomings of costly microscopy equipment. Herein, polymeric coatings made of gelatin

and derivatized cellulose are shown to affect both the drug-loading efficiency of DNPs and release kinetics, offering unprecedented solutions to the delivery of drugs with a fast degradation rate. Throughout this work, DNPs are also shown as efficient nanocarriers of immunological checkpoint-targeting peptide nucleic acids (PNAs), of whom the DNPs enhance cell uptake and membrane permeability. We demonstrate the ability of redox-sensitive DNPs to release PNAs in breast and lung cancer cells upon specific exposure to altered levels of glutathione, which is the main character of the redox balance in human beings. Moreover, the outstanding advantages of microfluidics over bulk mixing are exploited for the development of gastro-resistant DNPs targeting metastatic cells for the oral treatment of colorectal cancer. For the first time, the oral administration of DNPs is considered a valid route to overcoming the challenges of intravenous injection, including the risk of vessel clogging. The vast subset of functionalization described herein (polymer coatings, antibody grafting, decoration with AuNPs, loading of different drugs) demonstrates the possibility to design DNPs targeting the cancer microenvironment specifically, improving both drug pharmacokinetics and efficacy. The reported results and *in vitro* investigations in multiple cell lines, both in monolayers and three-dimensional 3(D) structures, suggest that DNPs hold great promise as nanocarriers of various drugs and for the treatment of different diseases, among whom cancer has been thoroughly exploited.

Acknowledgments

First and foremost, I would like to express my warmest acknowledgments to the doctoral program in Pharmaceutical Science of the Department of Pharmacy of the University of Naples Federico II for allowing me to pursue my studies in such a challenging and motivating environment. Since I graduated in 2019, the Department of Pharmacy and the brilliant professors working inside accompanied me throughout my personal and scientific career. I also would like to thank the coordinator of the XXXV doctoral cycle in Pharmaceutical Science, Prof. Rosaria Meli, for her tireless efforts and firm support. I have long wished to express my deepest gratitude to Prof. Isabel Maria Gomez Monterrey for being a mentor, a protective figure, an enduring listener, and a trusted advisor. I owe you the way I started and still walk doing research. My sincere gratitude goes to my academic supervisor, Prof. Nicola Borbone, and co-supervisor Dr Ilaria Rea. I admire the way you watched over me during these years, with unwearied diligence, willful encouragement, and accurate severity. For this, I am in your debt. You both have contributed to shaping the inspired researcher I have become during these years and supported me till the finish line. Thank you, Ilaria, for your concerns about my plans, your supportive words, your valuable pieces of advice, and for the trust, you have placed in me.

Special thanks go to the Institute of Applied Sciences and Intelligent Systems of the National Research Council of Naples, and all the affectionate workers. Having been part of your institute for 4 years has always been a reason to brag. Several years in this institute have allowed me to come across dozens (if not hundreds) of people from different

divisions, backgrounds, and cultures. I would like to take this opportunity to thank each person that has crossed paths with me and taught me something, or just simply made me smile on those not-so-easy days. I am grateful to the NanoBioSYstem Group (NBSY), all its members and founders, especially Dr Luca de Stefano and Dr Ilaria Rea for supporting me during these years and allowing me to become part of such a dynamic superfamily. Thank you for sharing your knowledge and expertise with me. I am deeply thankful to all the collaborators and co-authors of my publications, for your cooperation and expertise, invaluable scientific input and text revision. This thesis would not have been possible without your help. Particularly, I would like to thank Dr Anna Chiara de Luca, Dr Enza Lonardo, Dr Donatella Delle Cave, and Dr João Pedro Martins. Your readiness to help and cheerful spirit is also very commendable. I would like to express my heartfelt gratitude to Giovanna Chianese for her priceless friendship, honesty and mutual esteem, for being the colleague and friend everyone would like to meet in their life. You are one of the few persons I could always count on during my doctoral studies. You shared my fears, wiped my tears while hiding your concerns, watched my temper and helped me improve it. I hope you may feel my honest gratitude through these simple words. Just saying thank you will never repay your kindness. An affectionate thanks to the Department of Pharmaceutical Chemistry and Technology of the University of Helsinki for allowing me to carry out my research in such a prestigious environment. Thank you Prof. Hélder Santos for hosting me in your highly stimulating and international lab. Without you, I wouldn't have experienced the beautiful Finnish culture. I would like to thank the reviewers of this doctoral dissertation, Prof. Hélder

Santos and Prof. Fabio Zobi (University of Freiburg). Your positive feedback was key to strengthening the scientific accomplishments described herein.

Finally, I would like to express my most heartfelt gratitude to my family and beloved ones, Franco, Loredana, Giulia, Mario e Francesco, for your continued love and support during these uncertain years. Thank you all for giving me the strength to reach for the stars and chase my dreams. You have been my inspiration and motivation through what have been the hardest moments of my personal growth and scientific career. None of this would have been possible without you by my side. My sister and little brother deserve my wholehearted thanks as well. I hope I have made you proud.

Faithfully,

A handwritten signature in cursive script, appearing to read "Chiara Zannoni".

Table of contents

Abstract.....	6
Acknowledgments.....	9
Table of contents.....	12
List of publications	16
Abbreviations.....	18
1 Introduction.....	24
1.1 Nanomedicine – new ways to face old challenges.....	24
1.2 Nanoparticles: classification, advantages, and applications	27
1.3 Mesoporous silica NPs: the case of natural biosilica from fossil diatoms	32
1.4 Bioengineered DNPs as novel nanotherapeutics.....	36
1.5 Metastatic colorectal cancer (CRC): current approaches and limitations.....	41
1.6 Controlled delivery of anti-cancer agents from DNPs	47
1.6.1 Sustained release of galunisertib from polymer-coated functionalized DNPs.....	49
1.6.2 Gelatin: a pH-sensitive coating for targeting L1-CAM ⁺ metastatic cells.....	50
1.6.3 Hydroxy-propyl-methyl cellulose: an enteric coating for oral administration of DNPs	54
1.6.4 Redox-controlled release of anticancer peptide nucleic acid by diatomite nanoparticles.....	57
1.7 Hybrid multifunctional DNPs as label-free drug monitoring platforms.....	59
2. Aims.....	64
3. Methods.....	68

3.1 Sonication, purification, production, and aminosilanization of diatomite nanoparticles (DNPs).....	68
3.2. Preparation of galunisertib-loaded gelatin-covered hybrid DNPs (DNPs-AuNPs-LY@Gel) modified with the anti-L1-CAM antibody...	68
3.3 Improvement of the galunisertib loading capacity of plasmonic DNPs via the formation of gelatin shells of varying thicknesses	70
3.4 Development of redox-responsive DNPs for the GSH-triggered release of PNA in cancer cells.....	71
3.5 Fabrication of the microfluidic platform for the encapsulation of antibody-modified DNPs (DNPs-Gel-Ab) in enteric coatings.....	72
3.6 Production of encapsulated-DNPs via glass capillary-based microfluidic technology.....	72
3.7 Evaluation of the binding efficiency of protein and antibody anti-L1-CAM to the active-targeted DNPs-LY@Gel-Ab.....	73
3.8 Physicochemical characterization of the developed formulations	74
3.9 NMR Spectroscopy standard ¹ H NMR experiments.....	75
3.10 In vitro drug-loading capacity and release studies	76
3.11 Stability studies of encapsulated-DNPs.....	80
3.12 Raman and SERS microscopy: set up experiment and SERS gain measurement.....	80
3.13 Galunisertib release from the DNPs-AuNPs-LY@Gel in vitro and living cells by SERS.....	81
3.14 Cell lines and culture conditions	82
3.15 Cell viability assays.....	83
3.16 RNA preparation and real-time PCR	85
3.17 Confocal fluorescence imaging.....	85
3.18 Internalization of DNPs-AuNPs-LY@Gel in CRC cells by Raman spectroscopy.....	87
3.19 Cell uptake studies by fluorescence-assisted cell sorting (FACS)	88

3.20 Quantification of the expression levels of the cell surface antigen L1-CAM.....	89
3.21 Migration assay.....	90
3.22 Hemotoxicity study	91
3.23 Suspension cultures assay	91
4. Results and discussion	94
4.1 Delivery and real-time monitoring of galunisertib in colorectal cancer cells by plasmonic-assisted DNPs	94
4.1.1 DNPs-AuNPs-LY@Gel nanosystem preparation and characterization	94
4.1.2 Evaluation of the loading and release capacity of the DNPs-AuNPs-LY@Gel	99
4.1.3 SERS monitoring and real-time quantification of the delivered galunisertib in living CRC cells.....	101
4.1.4 Evaluation of MET induced by DNPs-AuNPs-LY@Gel in CRC cells.....	107
4.1.5 Targeting L1-CAM on CRC cells with anti-L1-CAM modified DNPs-AuNPs-LY@Gel-Ab	117
4.1.6 Inhibition of the TGF- β mediated metastatic pathway in CRC cell lines by DNPs-AuNPs-LY@Gel-Ab	121
4.2 Enhancement of the galunisertib loading capacity of gelatin-capped plasmonic DNPs for drug delivery applications	127
4.2.1 Fabrication and characterization of plasmonic DNPs with gelatin shells of varying thickness	127
4.2.2 Correlation of gelatin concentration and shell thickness of the AuDNPs-LY@Gel _x based on a validated optical model.....	132
4.2.3 Evaluation of the galunisertib loading capacity of the AuDNPs-LY@Gel _x with different gelatin thicknesses	137
4.2.4 Application of the developed optical nanosystem for the monitoring of galunisertib release by absorption studies.....	141
4.3 Microfluidic-assisted production of gastro-resistant active-targeted diatomite nanoparticles for the local release of galunisertib in metastatic CRC cells.....	144

4.3.1 Production, physicochemical characterization, and microfluidic encapsulation of L1-CAM-targeting DNPs-Gel for oral administration.	144
4.3.2 Drug-loading, release, and dissolution studies of the encapsulated-DNPs.....	152
4.3.3 Quantification of L1-CAM expression on Caco-2, HT29-MTX, and SW620 cells and cell viability studies.....	156
4.3.4 Cell-DNP interaction studies by confocal microscopy	162
4.3.5 Specificity of the antibody-labeled DNP uptake in cells by FACS.....	166
4.3.6 Encapsulated-DNPs inhibit the migration of the metastatic cell line SW620.....	168
<i>4.4 Development of redox-responsive DNPs for on-demand intracellular release of an anticancer antisense peptide nucleic acid</i>	173
4.4.1 Multistep chemical approach for the development of redox-responsive DNPs	173
4.4.2 One-pot chemical strategy for the development of redox-responsive DNPs	177
4.4.3 PNA loading and release and cell viability studies.....	180
4.4.4 Cell uptake and activity studies of the developed DNPs-PNA	184
5. Conclusions and future perspective	189
Funding and grants.....	193
References.....	193

List of publications

The following list includes first-author and co-author works published between 2019 and 2022 and sorted here by reverse chronological order.

1. C. Tramontano, J. P. Martins, L. De Stefano, M. Kemell, A. Correia, M. Terracciano, N. Borbone, I. Rea, H. A. Santos, Microfluidic-Assisted Production of Gastro-Resistant Active-Targeted Diatomite Nanoparticles for the Local Release of Galunisertib in Metastatic Colorectal Cancer Cells, *Adv. Healthcare Mater*, 2022, 2202672. <https://doi.org/10.1002/adhm.202202672M>.
2. M. Terracciano, F. Fontana, C. Tramontano, I. Rea, L. De Stefano, G. Oliviero, N. Borbone and H. A. Santos; Development of Surface Chemical Strategies for Synthesizing Redox-Responsive Diatomite Nanoparticles as a Green Platform for On-Demand Intracellular Release of an Antisense Peptide Nucleic Acid Anticancer Agent, *Small* 2022, 2204732. <https://doi.org/10.1002/sml.202204732>
3. V. Nocerino, B. Miranda, C. Tramontano, G. Chianese, P. Dardano, I. Rea, L. De Stefano; Plasmonic Nanosensors: Design, Fabrication, and Applications in Biomedicine, *Chemosensors*, 2022, 10, 150, <http://doi.org/10.3390/chemosensors10050150>
4. C. Tramontano, L. De Stefano, M. Terracciano, G. Chianese, I. Rea; Diatomite-based nanoparticles: Fabrication strategies for medical applications, in *Algal Biotechnology* (Eds.: Ahmad, A.; Banat, F.; Taher, H.), *Elsevier*, 2022, pp. 427–446, <https://doi.org/10.1016/B978-0-323-90476-6.00005-4> (Book chapter)
5. C. Tramontano, B. Miranda, G. Chianese, L. De Stefano, C. Forestiere, M. Pirozzi, I. Rea; “Design of Gelatin-Capped Plasmonic-Diatomite

- Nanoparticles with Enhanced Galunisertib Loading Capacity for Drug Delivery Applications”, *Int. J. Mol. Sci.*, 2021, 22, <https://doi.org/10.3390/ijms221910755>
6. C. Tramontano[§], S. Managò[§], D. Delle Cave, G. Chianese, G. Zito, L. De Stefano, M. Terracciano, E. Lonardo, A.C. De Luca, I. Rea, SERS quantification of Galunisertib Delivery in Colorectal Cancer Cells by Plasmonic-Assisted Diatomite Nanoparticles, *Small*, 2021, 2101711. <https://doi.org/10.1002/sml.202101711>
 7. A. Verde, M. Mangini, S. Managò, C. Tramontano, I. Rea, D. Boraschi, P. Italiani and A.C. De Luca; SERS sensing of bacterial endotoxin on gold nanoparticles, *Front. Immunol.*, 2021, <http://doi.org/10.3389/fimmu.2021.758410>
 8. M. Terracciano, C. Tramontano, R. Moretta, B. Miranda, N. Borbone, L. De Stefano, I. Rea; Protein-modified porous silicon optical devices for biosensing in Porous Silicon for Biomedical Applications, 2nd Edition, *Woodhead Publishing*, 2021 (Book chapter)
 9. C. Tramontano, G. Chianese, M. Terracciano, L. De Stefano, I. Rea, Nanostructured Biosilica of Diatoms: From Water World to Biomedical Applications, *Appl. Sci.* 2020, 10 (19), 6811; <https://doi.org/10.3390/app10196811>
 10. Rea, P. Dardano, R. Moretta, C. Schiattarella, M. Terracciano, M. Casalino, M. Gioffrè, T. Cresci, G. Chianese, C. Tramontano, N. Borbone, L. De Stefano; Hybrid organic/inorganic nanomaterials for biochemical sensing in *Sensors and Microsystems: Proceedings of the AISEM 2020 Regional Workshop* (p.93), *Springer Nature*. <https://doi.org/10.1007/978-3-030-69551-4>

Abbreviations

Ab	Antibody
CAN	Acetonitrile
ANOVA	Two-way analysis of variance
APC	Allophycocyanin
APTES	(3-)Amino-propyltriethoxysilane
ATR	Attenuated total reflectance
ATCC	American Type Culture Collection
BF	Bright field
C	Carbon
<i>ca.</i>	Circa
Caco-2	Human colon adenocarcinoma (cell line)
COOH	Carboxylic acid
CRC	Colorectal cancer
CSC	Cancer stem cells
D_i	Inner diameter
DAPI	4',6-Diamidino-2-phenylindole
DLS	Dynamic laser scattering
DMEM	Dulbecco's modified Eagle's medium
DMF	N, N-dimethylformamide
DMSO	Dimethyl sulfoxide
DNPs	Diatomite nanoparticles
D-PBS	Dulbecco's phosphate-buffered saline
<i>e.g.</i>	For example,
EDC	1-Ethyl-3-(3-dimethyl aminopropyl)-carbodiimide

EDTA	Ethylenediaminetetraacetic acid
EDX	Energy dispersive X-ray
EMA	European medical agency
EMC	Extracellular matrix
EMT	Epithelial-to-mesenchymal transition
Eq.	Equation
EtOH	Ethyl alcohol
Fab	Fragment antigen binding
FACS	Fluorescence-assisted cell sorting
FaSSIF	Fasted-state simulated intestinal fluid
FBS	Fetal bovine serum
FCM	Flow cytometry
FTIR	Fourier transform infrared spectroscopy
FDA	Food and drug administration
Fig.	Figure
FITC	Fluorescein isothiocyanate
GSH	Glutathione
GRAS	Generally regarded as safe
HBSS	Hanks' balanced salt solution
HEPES	4-(2-hydroxyethyl)-1-piperazineethanesulfonic acid
HPLC	High-performance liquid chromatography
HPMC	Hydroxy-propyl-methyl cellulose
Ig	Immunoglobulin
IV.	Intravenous
L1-CAM	Ligand 1 cell-adhesion molecule
LC	Loading capacity

LY	Galunisertib
LSPR	Localized surface plasmon resonance
MET	Mesenchymal-to-epithelial transition
MES	2-(N-Morpholino) ethane sulfonic acid hemisodium salt
MP	Microparticles
MRI	Magnetic resonance imaging
N	Nitrogen
NEEA	Non-essential amino acids
NHS	N-hydroxy succinimide
NH ₂	Amino group
Nm	Nanometer
NMR	Nuclear magnetic resonance
NPs	Nanoparticles
OSHA	Occupational safety and health administration
PBS	Phosphate-buffered saline
PDI	Polydispersity index
PEG	Polyethylene glycol
Pen/Strep	Penicillin/Streptomycin
PFA	Paraformaldehyde
Pr-A	Protein-A
PVA	Polyvinyl alcohol
qPCR	Quantitative real-time PCR
RBC	Red blood cells
RNA	Ribonucleic acid
ROS	Reactive oxygen species
RP	Reversed phase

RPMI	Roswell Park Memorial Institute 1640 medium
RT	Room temperature
S	Silicon
SGF	Simulated gastric fluid
SDS	Sodium dodecyl sulphate
SERS	Surface-enhanced Raman scattering
SiO ₂	Silica
SiRNA	Small interfering ribonucleic acid
TEM	Transmission electron microscopy
TEOS	Tetraethyl orthosilicate
TGF	Transforming growth factor
TMOS	Tetramethyl orthosilicate
UV	Ultraviolet-
Vis	Visible
w/w	Weight for weight
α	Alpha
β	Beta
ζ	Zeta

CHAPTER I

Introduction

1 Introduction

1.1 Nanomedicine– new ways to face old challenges

To manipulate matter on the atomic/molecular scale on needs was an old dream of natural science but it became true in 1960 with the production of the first nanomaterials.^[1] Ever since, nanotechnology has been introduced into our daily routine, opening alternative approaches in optics, electronics, chemistry, pharmaceutical industry, engineering, and medicine.^[2] The application of nanotechnology to medicine has been defined as nanomedicine, which consists of the use of nanomaterials for the prevention, diagnosis, follow-up, and treatment of disease. The use of nanotechnology in medicine has been considered a key-enabling technology capable of providing new tools for old challenges and unmet medical needs.^[3] So far, 50 nanomedicine formulations reached the market and 3 new products (Onpattro[®], Hensify[®] and Vyxeos[®]) have been recently approved, showing that nanomedicine overcomes critical barriers in conventional medicine and improves patients' lives.^[4] The secret behind nanomedicine success is the nanomaterial, which possesses unique physicochemical properties exceeding those of the conventional bulk equivalent, due to a smaller size.^[5] The European Medicines Agency (EMA) defines nanomedicines as products with at least one component at the nanometer (10^{-9} m) scale with (i) specific properties defined by medical needs (*e.g.*, administration route), and (ii) associated with the clinical advantages of nano-engineering (site-specific effect).^[6] Nanomaterials differ from their bulk counterpart due to the high volume-to-surface area *ratio* and generation of possible quantum effects, yielding a wide variety of applications in medicine. Nanomedicine, often combined

with other technologies (*e.g.*, microfluidics and robotics), has the potential to enable early detection through a novel technology for imaging and sensing, facilitating the follow-up with real-time monitoring of crucial parameters.^[7-12] From a therapeutic point of view, nanomedicine enables administering drug delivery systems capable of increasing drug availability and improving the efficacy of treatments. Recently, theranostics has emerged as a promising approach offering diagnosis and therapy simultaneously within the same system.^[13] Overall, biosensing, diagnostics, and targeted drug delivery represent the core disciplines of nanomedicine, and, therefore, they are the main objects of this thesis and the included works. The success of nanotechnologies in drug delivery can be explained by the recognized advantages in clinics, such as increased drug distribution, improved pharmacokinetics, and escape of critical barriers, including kidney filtration and clearance *via* the reticuloendothelial system.^[14] A drug delivery system is generally designed to encompass two elements: (i) control over the time of release, and (ii) targeting ability that ensures the release of the drug to the site of disease. As consequence, nanomedicine provides conventional drugs with the information to reach the destination, reducing premature loss of drugs in critical barriers and related side effects. Due to the hyper-growth of patients being diagnosed with cancer and requiring more effective treatments, almost 50% of nanomedicine market revenue is for anticancer products.^[15] Emerging nanotherapeutics have been successfully investigated also for chronic respiratory disease, anti-inflammatory syndromes, regenerative medicine, vascular disease, anti-infective, and diabetes. The impact of nanotechnology on therapeutic strategies is

flagged by the number of papers, grants, and companies in the field, which portray one common desire: bringing nanomedicine into the clinic.

Moreover, science has proven that some diseases, such as cancer, diabetes, and chronic inflammation, can turn into silent killers if diagnosed too late.

These health issues are translated into technological challenges that can be solved by fabricating cheap, accurate, and sensitive biosensors with advanced nanotechnologies. Biosensors are composed of a biorecognition element that selects the analyte from the sample, and a transducer that can be a nanoscale material of any shape (*e.g.*, particles, rods, stars, rattles).^[16]

The transducer can be electrochemical, optical, piezoelectric, electronic, and gravimetric, allowing for transducer-based classifications. The intelligent use of nano-objects in the development of biosensors has led to several improvements in diagnostics, such as increased device sensitivities, stability, response rate, and reduced limits of detection.^[17]

The high surface area of nanomaterials, that is the total area per unit mass, drives the enhancement of the sensitivity of field-effect transistor-based biosensors, as it enables the immobilization of a larger amount of biorecognition units. Moreover, some nanomaterials are characterized by magnetic properties, catalytic activity, electrochemical properties, and mechanical strength that are important for biosensing applications.^[18]

Among all the available biosensors used in nanomedicine, optic sensors based on gold nanoparticles are widely used for the fabrication of SARS-Cov-2, glucose, and pregnancy point-of-care tests.^[19] The key advantage of optical sensors is their low cost for volume production and mass use, which skyrocketed their applications in the pharmaceutical industry. Overall, the global nanotechnology-based biosensors market has grown up

fast in recent years due to a combination of nanotechnology, chemistry, physics, and medical sciences. Undoubtedly, with the expanding research on nanomaterials, their use in biosensing is expected to offer more innovations in the years to come.

1.2 Nanoparticles: classification, advantages, and applications

The identification of immunologically inert materials eliciting the desired functions resulted in the fabrication of a vast collection of nanoparticles (NPs), which are usually classified by their composition as organic, inorganic, and hybrid.^[20] In the word “nanoparticles”, the prefix “nano” has greek origins and means “midget”, or something that is considerably tiny, such as particles one thousand millionth of a meter (10^{-9}) in size.^[21] NPs are the most famous nanomaterials used as either drug carriers for therapy or components of bioimaging and diagnostic platforms. Each class of NPs includes, in turn, different subclasses with peculiar physicochemical and biological properties.^[22] The world of NPs can be depicted as a big library with shelves: each shelf contains products (NPs) classified by properties (*e.g.*, size, composition, surface area, surface chemistry, suitable applications), and researchers can take from the library the most appropriate product for the desired therapeutic outcome. Some of the most common subsets of NPs are reported in **Figure 1**.

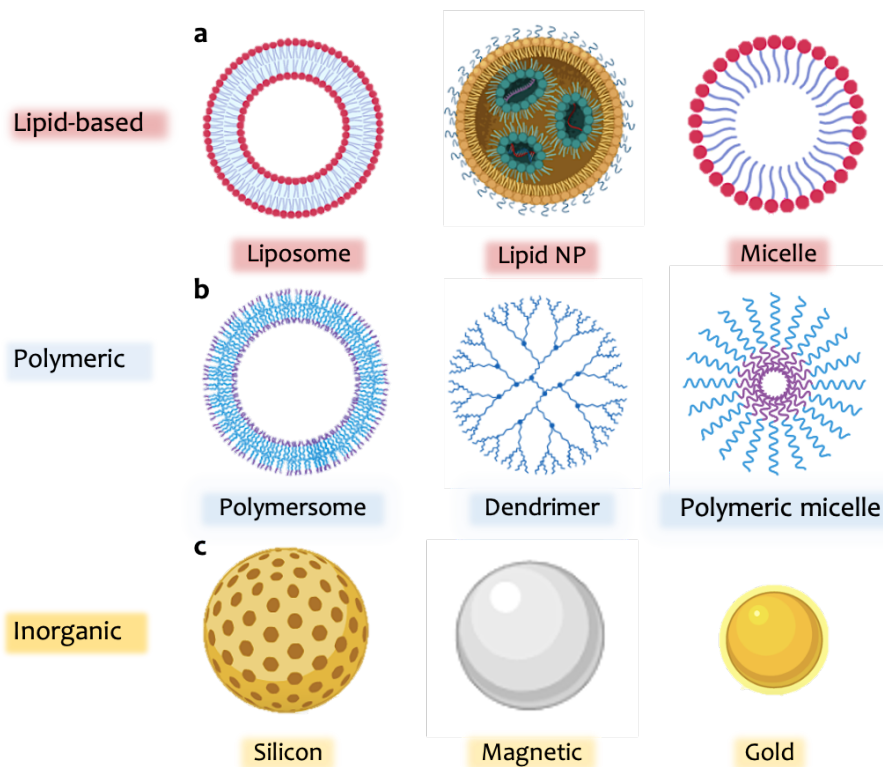


Figure 1. The library of NPs. **a)** Lipid-based, **b)** Polymeric, and **c)** Inorganic NPs are the most investigated types in nanomedicine, with peculiar properties depending on size, morphology, physical and chemical features. Image realized with Biorender tools.

From the combination of organic and inorganic NPs, researchers also developed a set of hybrid systems, which display advantages over non-hybrid NPs.^[23] Lipid-based NPs including liposomes and micelles are constituted of phospholipids at the interface of an internal aqueous compartment (**Fig. 1-a**). Due to their structure, these NPs can load both hydrophobic and hydrophilic drugs, therefore they represent the most common class of Food and Drug Administration (FDA)-approved

nanomedicine products.^[24] Polymeric NPs, such as polymersomes and polymeric micelles, are core/shell systems formed by monomers of natural or synthetic polymers, or constituted by pre-formed blocks (**Fig. 1-b**). Recently, there has been an increasing trend in the production of polymeric NPs as drug carriers, due to their stability *in vivo* and capability of increasing the solubility of insoluble pharmaceutical agents.^[25] The first polymeric NPs for intravenous administration were approved in 1989 for the sustained release of Leuprorelin (Lupron Depot[®]) for endometriosis (**Fig. 2**). A few years later, liposomes encapsulating doxorubicin joined the global race of nanomedicine and were approved for the treatment of Kaposi's sarcoma.^[26] Ever since, the market of nanotherapeutics has been enriched by novel products, including emulsions, hydrogels, and polymer micelles, most of which are administered intravenously (**Fig. 2**). The loudest and most recent demonstrations of nanomedicine breakout are lipid NPs delivering the messenger RNA (mRNA), which are administered as vaccines to fight against COVID-19 infection.^[27]

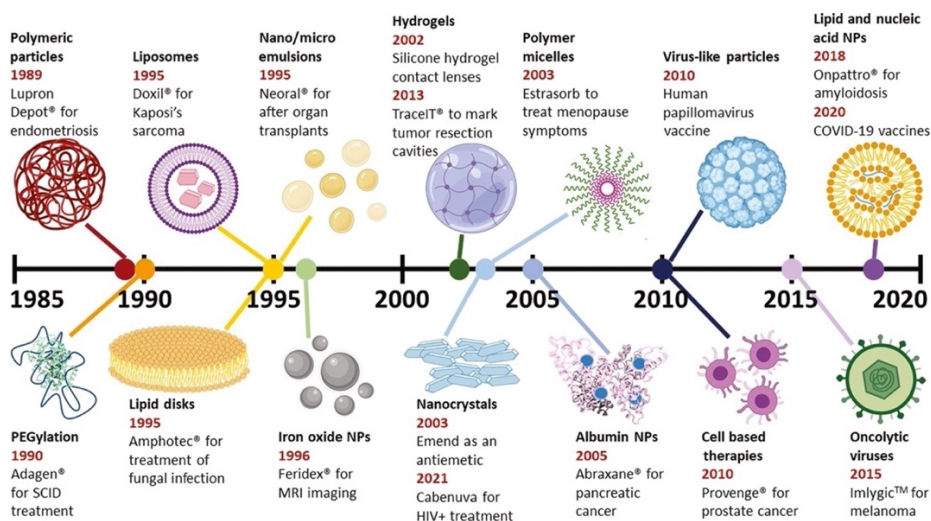


Figure 2. Timeline of nanomedicine-based products approved by FDA from 1985 to 2020. Adapted with permission of Elsevier, Copyright © 2021.^[28]

The exploration of more robust nanomaterials for drug delivery purposes turned the spotlight on inorganic nanomaterials, such as silicon, gold, and iron NPs (Fig. 1-c), which were first approved as imaging tools. Later on, the peculiar properties of inorganic NPs promoted their use as drug carriers, especially for cancer therapy.^[29,30] Among all, silicon (Si) and silica (SiO₂)—the oxidized form of Si —, NPs found wide application in drug delivery due to their porous structure, which allows for the entrapment of a higher amount of drug cargo than organic NPs.^[31] Moreover, due to their robustness, most inorganic NPs are stable in body fluids for longer periods, serving purposes otherwise unattainable by other types of nanomaterials.^[32] The clinical application of inorganic NPs, however, still represents a major issue due to toxicity concerns, and, as consequence, a few inorganic nanocarrier-based products have been

accepted by the FDA.^[33] On the contrary, inorganic NPs, especially gold NPs, are widely accepted as signal reporters in biosensing or as contrast agents for magnetic resonance imaging (MRI), due to their physicochemical properties and ease of production.^[33] Inorganic NPs allow for the detection of relevant analytes through colorimetric (gold), magnetic (iron oxide), or fluorescent (quantum dots) signals. The first example of an FDA-approved inorganic formulation for healthcare application consisted of a combination of silica and gold NPs known as AuroLase[®]. This formulation is composed of silica-gold nanoshells coated with (poly) ethylene glycol (PEG) and designed to penetrate tumor tissues.^[34] NPs in AuroLase[®] represent the exogenous absorber of a near-infrared laser: they convert laser energy into heat, enabling both tumor imaging and ablation.^[34]

By combining the advantages of organic NPs as drug carriers with the robustness of inorganic NPs, researchers developed a collection of hybrid NPs.^[35] The combination of different systems within a single hybrid platform enabled improvement in bloodstream half-life, premature elimination from the body and low encapsulation rates.^[36] Moreover, these hybrid NPs serve as theranostic platforms for sustained drug release and diagnosis, covering both therapeutic and imaging purposes. Overall, regardless of composition, NPs-based approaches possess common advantages over conventional methods as they: (i) enable the delivery of insoluble drugs previously considered undevelopable due to water instability; (ii) protect drug cargo from enzymatic degradation or pH inactivation, increasing drug availability; (iii) allow for targeted drug

delivery while reducing side effects; (iv) enable detecting low concentrations of analytes for early diagnosis of disease.

1.3 Mesoporous silica NPs: the case of natural biosilica from fossil diatoms

Mesoporous silica NPs represent a key example of innovation in material science to develop nanotechnology-based drug delivery systems. The increasing demand for NPs carrying a consistent amount of payload placed the attention of academic and industrial communities on porous NPs. Among them, mesoporous silica NPs represent one of the most influential type.^[37] These inorganic systems have attracted increasing attention due to their unique properties, such as a large surface area ($\sim 500 \text{ m}^2 \text{ g}^{-1}$), 2-50 nm sized pores, customizable surface chemistry, and extensive multifunctionality.^[38] Furthermore, silica is highly biocompatible and degradable, recognized by the FDA as “generally regarded as safe” (GRAS), and, therefore, it holds promises for clinical purposes.^[39] The main advantage of mesoporous silica over organic NPs is the ordered pore network, which enables the loading of a large number of drug molecules with a controlled release kinetics.^[39] The possibility to modify the surface of mesoporous silica by targeting ligands *via* chemical strategies resulted in the fabrication of NPs for *stimuli*-responsive, light-sensitive, sustained, and controlled release.^[40] Mesoporous silica nanocarriers represent a valid alternative to conventional therapeutic approaches, overcoming issues related to multi-drug resistance phenomena, metabolization, and untargeted effects. However, the synthesis of mesoporous silica is hardly scalable due to the costs and time required for mass production, hindering the translation of NPs into clinics. The current synthetic approach for

mesoporous silica is based on the sol-gel method, which involves: (i) silica precursors or sodium silicate tetraethyl orthosilicate (TEOS), (ii) the use of surfactants as structure directing agents, (iii) acid or basic catalysis.^[41] In general, the synthetic process involving precursors requires high pressure, temperature, and long reactions to remove the precursors and organic matter. To make this process easier and faster for mass production, researchers replaced TEOS with tetramethyl orthosilicate (TMOS), which accommodates the reaction's speed.^[42] However, TMOS is considered a hazardous material by the Occupational Safety and Health Administration (OSHA), highly toxic by inhalation and very irritating to skin and eyes. Furthermore, mice exposed to inhalation of both TEOS and TMOS showed lesions in the nasal mucosa, kidney damage, and cytolysis in the red and white pulp of the spleen.^[43] The challenge for researchers is, therefore, to find a less toxic approach for the production of mesoporous silica NPs or an alternative source of silica.

Fortunately, an alternative material to synthetic mesoporous silica for biomedical purposes has been offered by nature and consists of biogenic nanostructured porous silica derived from diatoms.^[44] These unicellular algae represent the main source of natural silica in the aquatic environment and the undisputed characters of bio-silification, the process by which microorganisms absorb Si and convert that into SiO₂.^[45] Due to this process, diatoms' shell exhibit a unique 3D hierarchical structure termed *frustule*, which is rich in porous biosilica and displays a surface area of ~200 m² g⁻¹. The pore size can vary from 10–100 nm and from species to species: there are more than 200.000 different types of diatoms classified by their unique morphology (centric or pennate) and size (2–2000 nm).^[46]

The beautifully ordered porous array of diatoms represents an endless resource of green natural porous silica, which can replace the expensive and time-consuming synthetic mesoporous counterpart. **Figure 3** compares the characteristics of synthetic and natural silica, highlighting both common traits and differences.

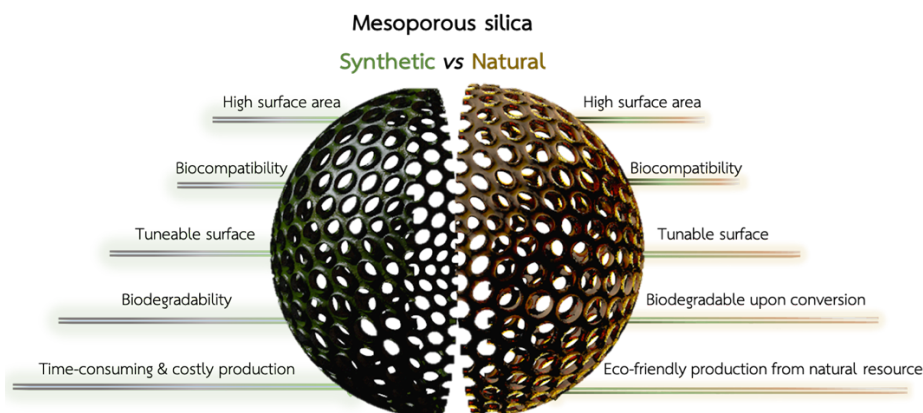


Figure 3. Synthetic mesoporous silica (green) *versus* silica from diatoms (brown). Synthetic and natural silica show common advantages, such as high surface area, tunable surface chemistry, and biocompatibility for drug delivery purposes. However, the production of NPs from diatom biosilica is cheaper, eco-friendly, and, overall, more convenient.

Surface area is a crucial parameter for the design of drug delivery systems as it influences the drug-loading capacity (LC), which is generally described by the following equation:

$$LC (\%) = \frac{\text{mass of entrapped drug}}{\text{mass of NPs}} \times 100$$

A larger surface area allows for a higher LC as it facilitates the entrapment of drug molecules within the porous structure of NPs. Both synthetic and biogenic mesoporous silica shows a considerable surface area of ~500 and

200 m² g⁻¹, respectively, suggesting that they are a valid material for the production of efficient drug delivery systems (**Fig.3**). Moreover, their surface is rich in reactive silanol groups, which can be further conjugated to biological moieties (*e.g.*, proteins and antibodies) for targeted NPs' uptake and drug release. Both types of silica were generally recognized as safe (GRAS) for food and pharmaceutical production, but their safety for clinical application is still under debate.^[47] Specifically, while synthetic silica is converted into orthosilicic acid (H₄SiO₄) in the body and filtered by kidneys, the biogenic counterpart obtained from diatom frustules is not degradable that easily.^[48] Diatom biosilica is mainly obtained from diatomaceous earth (also known as diatomite), which is a sediment record of fossilized diatom frustules.^[49] Due to its sedimentary feature, biosilica is not degradable as it is, but it can be converted into biodegradable silicon through a magnesium-thermic approach.^[50,51] The great advantage of diatom biosilica over mesoporous synthetic silica is represented by the facile, cheap, and scalable process of NPs' production (**Fig.3**). Nanostructured diatom biosilica can be obtained by mechanical crushing, filtration, and ultrasonication of a diatomite powder, which has a paltry price (\$1000 per ton, approximately).^[46] Through this first step, diatomite is reduced into NPs that preserve the porous structure of the original frustule with an average size between 200-400 nm. Afterwards, the obtained diatomite NPs (DNPs) are purified with acidic solutions to remove organic and metal residues and make the material harmless for biomedical applications.^[52] The whole process allows for the production a large amount of DNPs in 2 days, without expensive techniques and toxic reagents, which, instead, are needed for mesoporous silica production

(**Fig.3**). The advantageous features of diatom biosilica and DNPs have been extensively investigated by researchers in the last years, as marked by the increasing number of papers in the field.^[53,54] Both microparticles (MPs) and NPs have been studied as drug carriers, whereas, not infrequently, DNPs or frustules have been investigated also as cheap biosensing platforms.^[29,50,55–58] The following paragraphs describe the potential of DNPs either as nanocarriers, or biosensing platforms, or both. The expanding knowledge of surface chemical approaches to modify the surface of DNPs has also favored the production of DNPs with multifunctional capabilities of both drug release and biosensing.

1.4 Bioengineered DNPs as novel nanotherapeutics

Surface chemistry is the major factor influencing the properties of NPs as drug carriers, such as the ability to entrap drugs, cell uptake, and targeting features. The presence of reactive groups on the surface of NPs is of paramount importance when designing nanocarriers as it enables the attachment of compounds (polymers, antibodies, or proteins) to create smart nanotherapeutics. Various approaches to DNPs' functionalization have been proposed for drug delivery or biosensing purposes, including: (i) polymer conjugation for increased LC, (ii) silanization and pegylation to modify the surface of NPs with reactive amino (—NH_2) or carboxylic (—COOH) groups; (iii) attachment of gold NPs for optical purposes, (iv) encapsulation in a polymeric matrix for pH-sensitive drug release, (v) peptide conjugation for electrostatic drug-loading.^[52,55,59–61]

The first step in the fabrication of DNP-based drug delivery systems is the production of DNPs from diatomite powder, which is a standardized process from micrometric diatoms to DNPs (**Fig. 4**). Diatomite powder is

commercially available but can also be harvested from mines in quantities. The initial powder consists of fossilized porous diatom skeletons (frustules) with a micrometer size, which are ground by mechanical crushing in ethanol (**Fig. 4**). Later on, the dispersion of ground frustules undergoes a high-amplitude ultrasonication approach to obtain nanostructured silica.^[62] This step can take from 3 h to 2 days according to the equipment power, but it allows obtaining a large quantity of DNPs that could satisfy the lab needs for up to 1 year. The process of sonication is concluded when DNPs with an average size between 200 and 400 nm are obtained. Then, the dispersion can be filtered to select NPs of the desired size and centrifuged, or collected directly.

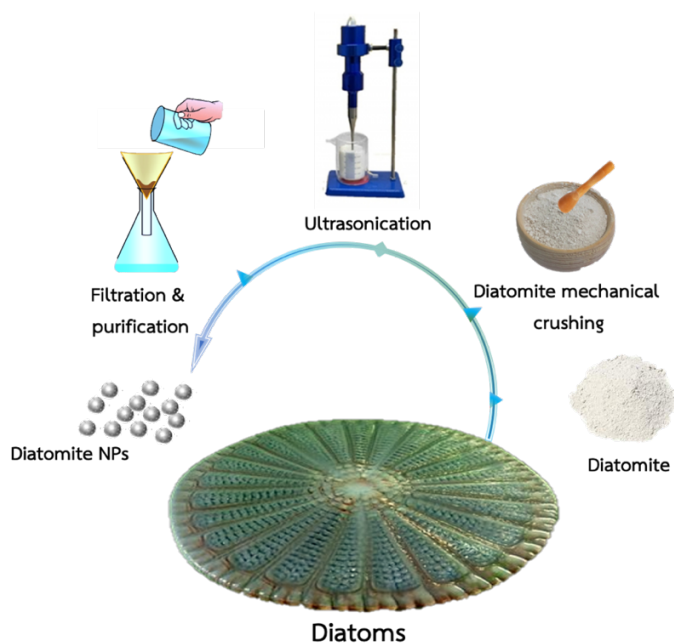


Figure 4. Process of DNPs' production from diatoms. Diatomite powder is nanostructured *via* mechanical crushing and ultrasonication. Then, DNPs having an average size of 200-400 nm are selected through filtration.

Finally, the obtained dispersion is purified to remove organic and inorganic impurities related to the sedimentary nature of diatoms.

The purification of the DNPs is mandatory to providing them with high biocompatibility for medical purposes. The process involves the treatment with a mixture of sulfuric (H_2SO_4) and hydrogen peroxide (H_2O_2), 4:1 respectively, known as Piranha treatment, and a solution of 5M hydrochloric acid (HCl). The former removes the organic matter related to the presence of fossilized frustules; the latter purges metal oxide (Al_2O_3 , Fe_2O_3 , CaO) impurities from DNPs, which arise from the sedimentary bioprocess of diatomite.^[59] The purification process decreases the percentage of metal oxide in DNPs (**Fig. 5**), whereas the silicon and porous ultrastructure of nanostructured frustules forming the DNPs are kept unaltered.

Compounds	Before purification (%)	After purification (%)
SiO ₂	92.1	94.6
Al ₂ O ₃	3.3	2.7
K ₂ O	1.0	0.8
CaO	1.8	0.9
Fe ₂ O ₃	1.8	1.0

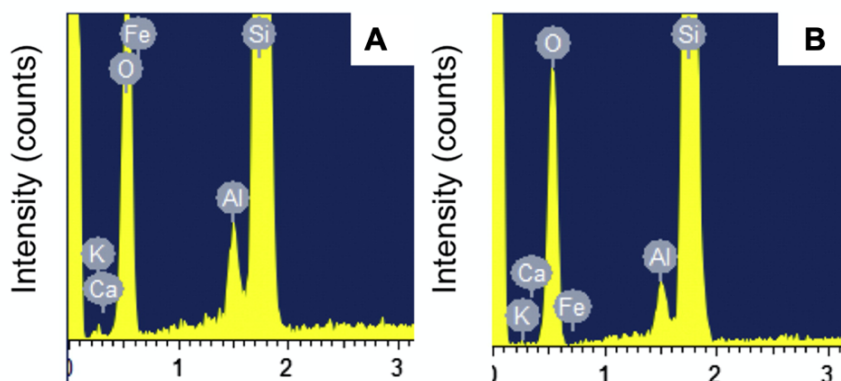


Figure 5. Composition of nanostructured DNPs before (a) and after (b) purification processes. The variation of metal oxide percentage in DNPs is reported in the upper Table.

When DNPs are produced by sonication and purification, they already show a highly reactive surface chemistry, which does not need to be activated for further conjugation steps. The NP surface, indeed, is rich in silanol groups (—Si—OH) that can be used to make siloxane linkages with silane coupling agents stabilizing the DNP dispersion.^[63] The most used organosilane is the (3-aminopropyl) triethoxysilane (APTES), which serves as an intermediate for further modification of DNPs. The silanization process offers two main benefits: it stabilizes DNPs avoiding aggregation in solution, and provides the surface with —NH_2 for further linkages *via* peptide bond formation.^[45] However, free —NH_2 can cause

cell stress and damage, therefore they are frequently masked by a polymer coverage, or involved in peptide bonds.^[64] Our group demonstrated that amino-silanized DNPs further modified with PEG and a cell-penetrating peptide are less toxic than amino-silanized DNPs as drug carriers. ^[64] Similarly, we reported that APTES-modified DNPs can be further functionalized with a cationic poly-D arginine peptide to electrostatically load and release a small interfering ribonucleic acid (siRNA) in H1355 cells.^[59] The advantages of a positively charged surface rich in —NH₂ was also investigated for the *in-situ* synthesis of gold NPs on DNPs' surface for label-free uptake and drug release monitoring in cancer cells.^[29,55,56] The realization of biosensing and monitoring platforms made of gold NPs and DNPs is described in detail in the following paragraphs.

A functionalization approach based on APTES and a thiol (—SH)-PEG-modified surface was also proposed for the development of redox-responsive DNPs carrying a peptide nucleic acid (PNA) capable of targeting malignant cells.^[65] The (—SH)-PEG played a key role in enabling the loading of the PNA sequence in DNPs by disulfide bond (S—S) and subsequent cleavage by glutathione in cancer cells.

Most of the surface modification approaches exploited in the last years were aimed at designing a biocompatible drug delivery system for the treatment of diverse types of cancer. The porous structure of DNPs can host and protect anticancer drugs with a fast metabolization rate, low water solubility, and high enzymatic degradation, thus increasing the active dose of the drug at the target site. These nanocarriers showed the capability of loading and releasing different anticancer agents, including nucleic acids, small molecules, and SiRNA in cancer cells with diverse release

kinetics.^[29,59,61,65] The drug release profile strongly depends on the loading strategy and can be driven by two mechanisms: (i) fast diffusion through the porous matrix (ii) electrostatic attraction between the drug and NPs becoming weak (iii) external *stimuli*, such as molecules, pH, temperature, (iv) diffusion through a polymer matrix covering the DNPs' surface. This last technique has gained particular interest in the last years, as it provides DNPs with higher LC and pH-sensitive release profiles. Our group recently described an overview of drug-loading strategies to achieve the desired release kinetics from DNPs.^[54] The entrapment of drug-loaded DNPs into the polymer matrix is undoubtedly the most effective drug-loading technique as it offers a sustained release for up to 48 h, avoiding burst and off-target delivery of the drug.^[66] Furthermore, the polymeric shell can be modified with a targeting agent to recognize a surface antigen expressed in the tumor, promoting a targeted uptake and drug release.^[67] Finally, the entrapment in *stimuli*-responsive polymer makes the drug release triggerable by external chemical factors that are altered in cancer cells, such as pH, enzyme, excess glutathione, and reactive oxygen species (ROS).

1.5 Metastatic colorectal cancer (CRC): current approaches and limitations

Despite the great advances in primary and adjuvant therapies, colorectal cancer (CRC) still ranks as the second most lethal cancer due to the outbreak of metastases to the liver.^[68] Metastases formation and chemoresistance remain the major clinical challenges in CRC treatments, limiting the prognosis and survival rate of patients diagnosed with CRC.^[69] Various biological pathways are involved in the migration and invasion of CRC to

a secondary tumor site, such as the transforming growth factor (TGF) - β /SMAD. The activation of TGF- β receptor 1 signaling induces the phosphorylation of receptor-regulated SMAD2/3 proteins, which play a critical role in the translocation of pro-metastatic signals to the nucleus.^[70] The phosphorylation of cytoplasmatic SMAD2/3 proteins is often upregulated in CRC and promotes metastases by increasing the transcription of genes involved in cell adhesion, motility, and extracellular matrix (ECM) composition.^[71] The spread of metastases in CRC is driven by a phenotype and functional transformation of the cells, which start overexpressing adhesive molecules to probe their surroundings, adapt their mechanical properties and migrate through a complex three-dimensional (3D) environment (**Fig. 6**).^[72] In this process, called epithelial-to-mesenchymal transition (EMT), the upregulation of TGF- β causes increased levels of pro-metastatic genes (Snail, Twist, Vimentin, and matrix metalloproteinases MMP-2) and mesenchymal markers, such as the L1 cell-adhesion molecule (L1-CAM) (**Fig. 6**). This molecule helps cells adhere and spread on the surface of blood capillaries and initiate the metastatic outgrowth in perivascular sites.^[73] In CRC, L1-CAM⁺ cells have the metastasis-initiating capacity and are responsible for adenoma initiation, carcinoma propagation, and liver metastatic colonization.^[74] Recent findings suggested that the TGF- β 1 promotes L1-CAM overexpression, which, in turn, is responsible for the malignant and migratory phenotype of CRC cells.^[75,76]

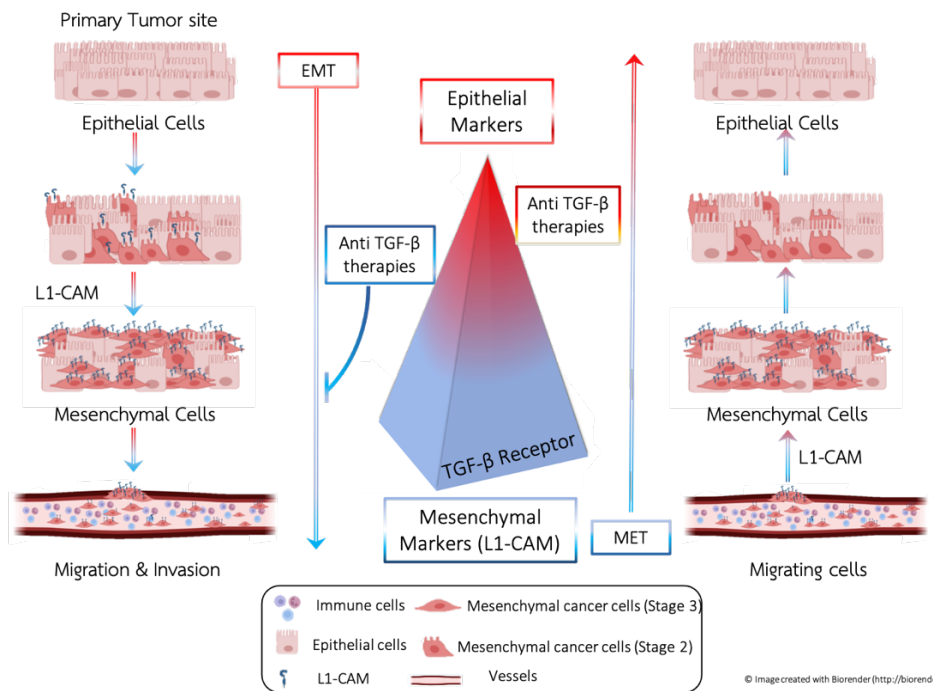


Figure 6. The epithelial to mesenchymal transition (EMT) in CRC is mediated by activation of TGF- β receptor. The spread of metastases is promoted by the overexpression of mesenchymal markers, such as L1-CAM, which promotes a morphological transformation of cells. The blockade of the TGF- β receptor is the most common strategy to revert mesenchymal cells into epithelial (MET). Image realized with Biorender © tools.

The primary treatment for CRC is the surgical resection alongside traditional chemotherapy in case of distant metastases, especially to the liver and lungs.^[77] Surgical resection of the primary tumor site is generally associated with increased survival rates, and, therefore, is considered the first option to treat non-metastatic CRC. However, for late-stage CRC characterized by distant metastases, the benefit of aggressive surgical

resection is still under debate due to limited evidence on whether metastatic sites are resected or not.^[78] In this scenario, emerging FDA-approved drugs inhibiting the TGF- β pathway have been brought into preclinical and clinical trials to halt the spread of metastases through the mesenchymal-to-epithelial (MET) transition.^[79,80] Among them, the small ATP-mimetic TGF- β inhibitor galunisertib (LY 2157299) has been orally administered both in monotherapy and in combination with standard antitumor regimens in Phase 2 clinical trials.^[81] Galunisertib is an oral small molecule that specifically downregulates SMAD2 phosphorylation, abrogating the activation of the TGF- β signaling and nuclear translation (**Fig. 7**). The TGF- β activation controls, in turn, the outburst of signals involved in crucial cell functions, such as proliferation, differentiation, migration, angiogenesis, and escape of immunological checkpoints.^[82] Hence, TGF- β inhibitors may lead to ECM remodeling (**Fig. 7A**), modulation of tumor vascularity and angiogenesis (**Fig. 7 B**), and suppression of metastases by activation of MET genes (E-Cadherin) (**Fig. 7 C**).^[83] Furthermore, the abrogation of SMAD proteins phosphorylation may reduce stemness and decrease cancer stem cells (CSCs), which are the main cause of tumor relapse (**Fig. 7 D**).^[84,85] Exposure-response studies on patients receiving galunisertib revealed that 300 mg day⁻¹ administered for 14 days on/ 14 days off treatment is the appropriate dosing regimen for patients with metastatic CRC.^[86] The pharmacokinetic profile of galunisertib revealed a drug absorption within 2.3 h and an elimination half-life of 8 h upon oral administration both in monotherapy or combined approaches (*e.g.*, coadministration with sorafenib).^[87] Recent studies showed an increment of disease control rates of ~ 20% in patients with low

baseline levels of TGF- β 1 receiving galunisertib in monotherapy.^[82] On the contrary, the oral administration of galunisertib in patients exhibiting high levels of TGF- β 1 did not produce similar outcomes, requiring a combined regimen of galunisertib and other anticancer agents (gentamicin, immune checkpoints inhibitors, sorafenib). Using a combination of drugs may decrease the probability a tumor is resistant to the treatments but it also exposes patients to a higher risk of side effects.^[88] When two drugs are administered simultaneously, indeed, the chance of drug interactions to occur increases, as well as the possibility that the side effects of both drugs get worse. Moreover, like many drugs for oral use, galunisertib is primarily cleared by the cytochrome CYP3A4 in the liver, with 13% of the initial dose excreted in the urine and feces. A secondary oxidative metabolism eliminates 4.6% of the dose of galunisertib from the body.^[87] This intense metabolism has two main drawbacks: it produces oxidative metabolites and glucuronides, which are the main product of galunisertib metabolization, circulating in the plasma; it decreases the bioavailability of galunisertib, making it necessary to administer a higher amount of drug or number of doses to compensate for the drug loss. However, additional drug doses affect liver functions, increase systemic toxicity, and hardly match patients' compliance.^[89] Likewise, when galunisertib is administered orally in combination with other drugs, the effects of drug metabolization and systemic toxicity multiply by two, paving the way for a debated question: how can we protect drugs, reduce liver metabolism, and increase drug availability while targeting cancer cells and decreasing side effects? Nanomedicine is the answer.

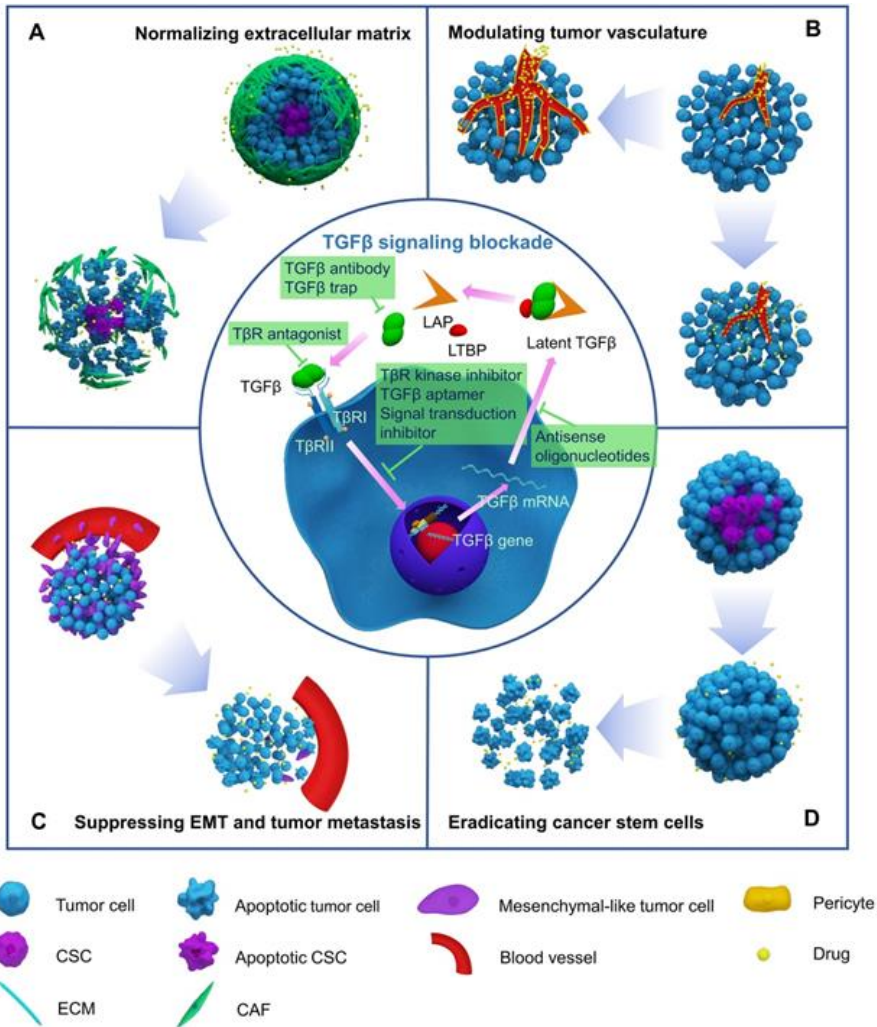


Figure 7. Role of TGF- β signaling and possible effects of its abrogation. Anti TGF- β therapies (small molecules, oligonucleotides, mRNA) can (A) normalize the ECM, (B) modulate tumor vasculature, (C) suppress EMT, and (D) eradicate cancer stem cells. Adapted with permission of Ivyspring International Publisher.^[83]

1.6 Controlled delivery of anti-cancer agents from DNPs

Based on their tremendous potential, DNPs have secured their place in the race for novel strategies for the treatment of metastatic CRC. The advantages offered using DNPs as drug carriers are summarized in **Figure 8**. The loading of anticancer drugs in DNPs can be achieved by immersion, covalent attachment, or non-covalent binding.^[90] Generally, the choice of drug-loading depends on the chemical structure of the drug itself, and the desired release kinetics. Small molecules with a little chemical reactivity, such as galunisertib, are preferentially loaded by immersion in favorable pH environments. The porous ultrastructure of DNPs acts as a sponge, absorbing drug molecules both in the pores and on the surface (**Fig. 8**). The release profile, in this case, is biphasic, with a first burst release from the surface and a slower delivery from the inner matrix.^[52] Oligonucleotide-based agents, such as siRNA, mRNA, DNA, and PNA, instead, can be modified to exhibit a reactive terminal group for covalent and non-covalent attachment strategies. The covalent strategy generally consists of a peptide bond between the drug and a degradable polymer, which triggers the release of the drug in the cell.^[91] The drug release profile, in this case, depends on the polymer degradation kinetics. The non-covalent drug-loading approach, instead, is based on a non-covalent linkage between the drug and DNPs, such as a disulfide bond (S–S) cleavable by reducing agents. With this approach, a burst drug release is observed immediately after bond cleavage.^[92]

The tunable chemistry of biosilica alongside mechanical stability (**Fig. 8**) enables modifying the surface of DNPs with a variety of reactive groups or coating agents. A common way to delay drug release from porous

systems is to entrap NPs in biocompatible polymers with pH-responsive features (*e.g.*, gelatin, cellulose, PEG).^[93] The polymer coverage around DNPs can be achieved by simple bulk mixing or using microfluidics, which offers precise control over the mixing process and higher batch-to-batch reproducibility.^[91,94] Sustained release from polymer-capped DNPs helps maintaining a constant level of drugs within the body, eliminating the likelihood of burst release and consequent drug degradation.^[95] This approach is particularly useful to deliver small molecules with high metabolization rates, such as galunisertib, which, otherwise, would be metabolized upon burst release. Polymers used as coating agents can be roughly classified as either gastro-resistant, such as cellulose, or sensitive to acidic pHs, like gelatin.^[96,97] The choice of the coating agent depends on many factors, including the programmed site of drug release, time of delivery, and desired administration route. Polymer shells can be further modified with probes offering the advantage of targeting metastatic CRC cells overexpressing L1-CAM, thus addressing the release of the drug locally (**Fig. 8**). This approach, known as active targeting, favors the uptake of modified-DNPs in malignant cells and promotes the local release of galunisertib. The attachment of anti-L1-CAM antibodies on galunisertib-loaded DNPs to L1-CAM may reduce the likelihood of untargeted drug release and uptake, which may cause the downregulation of TGF- β signaling in healthy cells.^[83] Altogether, the numerous advantageous properties offered by DNP-based treatments in therapeutic contexts seem to reasonably explain their ongoing exploration and interest. The translation into clinical nanomedicines is, however, still uncertain due

to biodegradability concerns, which motivate researchers to continue investigating the safety of this material.

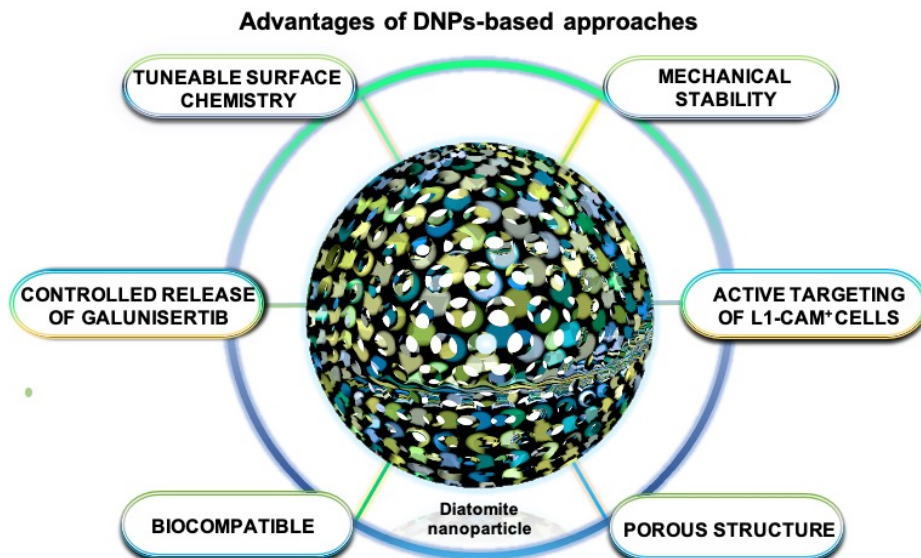


Figure 8. Advantages of DNP-based strategies. DNPs are attractive for the delivery of anticancer agents due to their advantages, such as porous structure, controlled drug release, mechanical stability, specific targeting of malignant cells, biocompatibility, and tunable surface chemistry.

1.6.1 Sustained release of galunisertib from polymer-coated functionalized DNPs

Even though inorganic NPs have been reported for the delivery of different types of anticancer agents, such as small molecules, nucleic acids, and proteins, only a few examples of galunisertib-loaded nanocarriers have been reported in the literature.^[29,92,98] The main reasons are the complicated chemical structure (**Fig. 9**) and the coexistence of several isoforms of the drug, which make the appropriate pH conditions for drug-loading challenging to find out. In a recent galunisertib-delivery system

developed by Wang's Lab, galunisertib was loaded in gold nanocage by immersion for 24 h.^[98] The immersion method is by far the most common and easiest loading approach but, unfortunately, is time-consuming, provides a low loading efficiency, and causes drug burst release. A valid strategy to fasten the loading reaction, increase galunisertib loading efficiency, and provide sustained release is to coat drug-loaded DNPs with a crosslinked polymer. This method has two main advantages: (i) the crosslinked polymer matrix helps DNPs retain the drug molecules inside the porous structure, thus delaying the time of release, (ii) the release of galunisertib is controlled by the polymer degradation, which occurs under internal *stimuli* (pH, enzyme). These *stimuli* represent physiological variations that occur naturally in target cells and tissue, such as altered pH levels or enzyme concentrations. When the polymer-degrading *stimulus* is unique to the metastatic CRC environment (*e.g.*, overexpression of metalloproteinases), the release of galunisertib is controlled only by the pathological trigger.

This thesis will focus on the use of gelatin and hydroxy-propyl-methyl cellulose (HPMC) as pH-sensitive polymers of relevance for the development of a DNP-based galunisertib drug delivery system for metastatic CRC.

1.6.2 Gelatin: a pH-sensitive coating for targeting L1-CAM⁺ metastatic cells

Gelatin is one of the most famous biopolymers used as a stabilizer of pharmaceutical formulations, including vaccines, and is recognized as safe by FDA for food and pharmaceutical purposes.^[99] It is constituted of denatured proteins obtained by partial hydrolysis of animal collagen

sourced from bovine skin or hide, porcine skin and, not infrequently, bone. The functional groups on the polymer backbone can be used for further chemical modifications, which can be especially useful for active targeting purposes.^[100] Having both acid ($-\text{COOH}$) and basic ($-\text{NH}_2$) functional groups, it displays amphoteric characteristics and can be crosslinked *via* the formation of an intramolecular peptide bond.^[101] Polymer crosslinking delays gelatin dissolution in water and improves stability in body fluids. When used as a coating agent of nanocarriers, gelatin lessens the diffusion of the drug out of the porous structure, providing the system with a pH-sensitive and sustained release profile.^[102] The major benefit of using gelatin for the development of CRC-targeted DNPs is related to its unique degradation pathway, which is triggered by two *stimuli* largely found in the metastatic CRC environment: the acidic pH and gelatin-degrading enzymes, such as MMPs.

The interstitial pH of normal tissues is usually 7.3 but it fluctuates substantially in cancer tissues due to deregulated metabolism, uncontrolled proliferation, and altered perfusion.^[103] Specifically, the extracellular cancer microenvironment pH ranges from areas of neutral pH to areas of intense acidification, with values as low as 5.6.^[104] Gelatin strength was reported to decrease at $\text{pH} < 6$, therefore the local change of pH in the tumor microenvironment is the main cause of polymer degradation. Moreover, it is generally reported that areas of H^+ accumulation overlap with increased concentration of MMPs, especially the MMP-9 isoform.^[105] MMP-9, also known as gelatinase-B, is highly expressed in CRC, where it binds and degrades gelatin for ECM remodeling. The overexpression of MMP-9 in CRC has been often associated with a hyper-activation status of TGF- β 1,

forming an interplay loop that promotes CRC proliferation and metastases.^[106] **Figure 9** shows an efficient functionalization approach for developing gelatin-coated galunisertib-loaded DNPs by bulk mixing. DNPs are first mixed with the drug solution for 2 h to favor the entrapment of galunisertib in the system. Then, the drug-loaded DNPs are immersed in a solution of gelatin with crosslinking agents promoting peptide bonds between gelatin chains and creating a polymeric coating.^[29] Considering the unique gelatin sensitivity to the composition of the tumor microenvironment, the polymer coating addresses the release of galunisertib into CRC cells, avoiding the undesired downregulation of the TGF- β signaling in healthy cells.

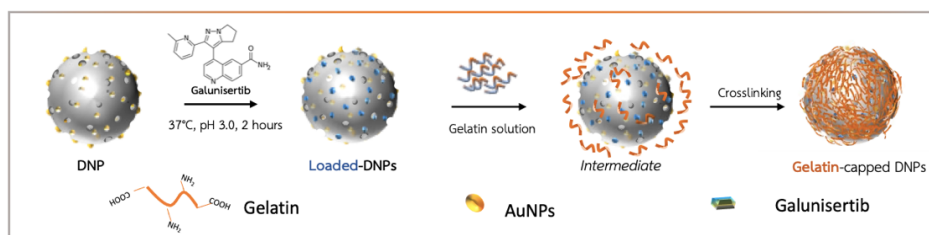


Figure 9. Functionalization of gelatin-coated galunisertib-loaded DNPs. DNPs are first mixed with galunisertib for 2 h to favor its entrapment in the porous structure. Then, the drug-loaded DNPs are immersed in gelatin with crosslinkers, which promote the formation of a polymeric coating. Adapted with permission from John Wiley and Sons, Copyright © 2021.^[29]

Using gelatin as a coating agent of drug-loaded DNPs offers one more incredible advantage for the treatment of metastatic CRC. Due to its high versatility, gelatin coatings can be further modified with biological ligands, such as antibodies, to target malignant cells overexpressing a specific antigen.^[107] The active targeting approach was first introduced in 1980

when monoclonal antibodies were hailed as magic bullets capable of targeting cancer cells.^[108] Since then, targeted therapy approaches have flourished and contributed to controlling and improving the survival rate of cancer patients. In metastatic CRC, the overexpression of the surface antigen L1-CAM opened up the way for active-targeted nanocarriers capable of binding to the adhesion molecule and inducing the release of drugs locally.^[109,110] Active targeting of L1-CAM cells may increase the accumulation of galunisertib in malignant cells due to the specific interaction of the antibody-labeled NPs and antigens on the cell membrane. With this approach, sustained drug release and active targeted go hand in hand. The delayed release profile ensures that galunisertib is not released until the antibody-labeled DNPs are bound to the targeted cells.

Two major functionalization approaches have been exploited for binding antibodies to NPs: covalent and non-covalent mode. The former consists of a peptide bond between the —COOH groups of the antibody and —NH₂ on gelatin, or vice versa; the latter involves modifying the gelatin coverage on DNPs with protein A, which binds to the crystallizable fragment (Fc) of antibodies upon structural rearrangement. Protein A is a bacterial cell wall peptide with a primary binding site for immunoglobulin G (IgG).^[111] Contrary to the covalent method that binds either the Fc or antigen-binding fragments (Fab) casually, protein A anchors the Fc region of the antibody *via* a site-specific binding. Therefore, using protein-A as a bridge between the gelatin-covered DNPs and the anti-L1-CAM antibody ensures that both the Fabs on the gelatin-covered DNPs are available for binding the antigen on metastatic cells. In the following thesis, active-targeted DNPs were developed using the protein-A, which resulted in being the most suitable

method for the attachment of the anti-L1-CAM antibody on the DNPs. Antibody-modified nanocarriers with two available sites for antigen binding display increased targeting efficiency and uptake, which, in turn, increase the drug availability at the desired site of action.^[112]

1.6.3 Hydroxy-propyl-methyl cellulose: an enteric coating for oral administration of DNPs

Hydroxy-propyl-methyl cellulose (HPMC) is an FDA-approved hydrophilic coating material used for the preparation of oral drug delivery systems.^[113] It possesses —COOH groups on the polymer side chains that make it insoluble at stomach pH (1-2) but soluble at neutral or alkaline intestinal pHs (pH > 6.5). For this reason, it is generally used as a coating agent of gastro-resistant capsules with a drug release profile starting at intestinal pH values.^[114] The solubility of HPMC depends on the number of —COOH (or other substituent groups) on the polymer backbone. The acetate succinate HPMC (HPMC-AS) type, for instance, dissolves at pH values between 5.5–6.8 but its degradation rate can be tuned modifying the amounts of methoxy, hydroxypropyl and succinyl groups. As an FDA-approved polymer, HPMC-AS is widely used for pharmaceutical applications, and a growing number of studies report its use for the fabrication of pH-sensitive nanocarriers for oral administration.^[115–117] The gastro-resistant features of HPMC-AS protects the delivered drug from acidic digestion and enzyme degradation in the stomach, delaying the release of the drug at the intestinal pH. There are two main methods to entrap DNPs in such an entering coating, which are the bulk mixing and the microfluidic approach.

Microfluidics is a cutting-edge technology that makes it possible to encapsulate nanocarriers with high batch-to-batch reproducibility, size stability, and using a few volumes of reagents. In the last years, this technique has gained increasing relevance for the production of advanced drug delivery systems with pH-responsive properties, especially for oral nanocarriers.^[94] Compared to bulk mixing processes, which often result in polydisperse NPs, microfluidics enables the precise encapsulation of NPs due to the well-controlled mixing of polymer solution and NPs inside micrometer-sized channels.^[94,118] A cheap way to fabricate a microfluidic platform for the encapsulation of DNPs in enteric coatings is the glass capillary-based technique (**Fig. 10**) consisting of an inner and outer capillary coaxially aligned to create a microfluidic platform.^[115] The entrapment of DNPs in HPMC occurs *via* nanoprecipitation of the polymer around DNPs. The organic phase composed of a dispersion of DNPs and HPMC is pumped in the inner capillary, whereas the nanoprecipitation agent (the water phase) is pumped in the outer capillary. The inner and outer flows are controlled by two pumps forming a 3D coaxial flow (**Fig. 10**). The microfluidic encapsulation of galunisertib-loaded DNPs may represent a turning point in the clinical translation of DNP-based nanocarriers because it offers an alternative administration route for such NPs that are not recommended for intravenous injection (IV). IV is generally the preferred route of NPs due to fast distribution, instantaneous onset of effects, and high drug bioavailability.^[119] IV route, however, is suggested for hydrophilic NPs smaller than 100 nm but not for larger nanocarriers with a size distribution between 200-400 nm, such as the DNPs.^[120] A valid alternative to IV injection is represented by oral

administration, which is the most common way to treat colon diseases and increase the drug bioavailability in the colon achieving a localized effect.^[121] However, gelatin-coated DNPs would not reach the colon upon oral administration due to the extensive gelatin degradation in the stomach by pH and enzymes. The digestion of the polymeric coating would, in turn, cause the untargeted release of galunisertib in the stomach, followed by absorption, liver metabolization, and reduced bioavailability. When DNPs are entrapped in the enteric coating by microfluidics, instead, gelatin is protected from degradation in the stomach by HPMC, which starts dissolving at pH 5.5. The progressive alkalization from the small intestine to the colon causes HPMC dissolution and promotes the pH-responsive release of galunisertib in the lower GI tract.

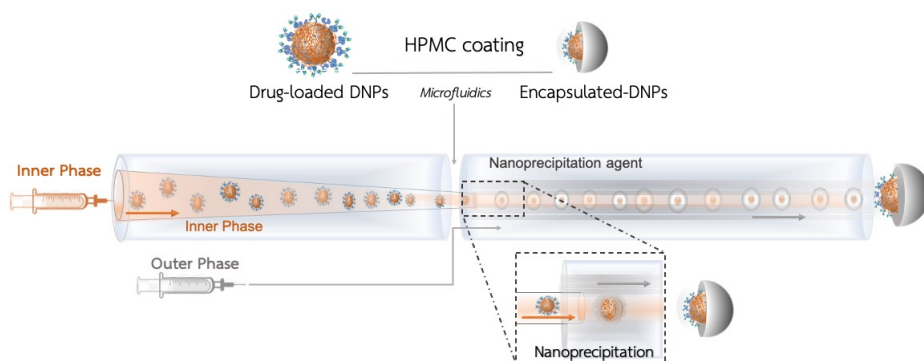


Figure 10. Encapsulation of modified galunisertib-loaded DNPs into HPMC by glass capillary-based microfluidics. The inner phase consisting of a dispersion of DNPs and HPMC is pumped in the inner capillary, whereas the outer phase (nanoprecipitation agent) flows in the outer capillary.^[122]

1.6.4 Redox-controlled release of anticancer peptide nucleic acid by diatomite nanoparticles

The recent advances in the understanding of cancer metabolism have increased the interest of researchers in the role of glutathione (GSH) in cellular redox homeostasis. GSH is a tripeptide largely found in cells where it represents the major antioxidant and scavenger system.^[123] In physiological conditions, reduced GSH is the predominant form and is converted into oxidized GSSG upon reaction with ROS by GSH-dependent peroxidases. This mechanism protects cells against exogenous and endogenous toxins, which may cause oxidative stress and DNA damage.^[124] A four-fold increase in the levels of GSH has been reported in different types of cancer, where it mediates cell proliferation, differentiation, and metastatic activity. The significant difference between the concentration of reducing GSH in cancer and healthy cells has brought attention to this tripeptide as the trigger of drug release from redox-responsive nanocarriers.^[125] To develop a GSH-sensitive nanocarrier, both the surface of NPs and drug chemical structure should be modified with thiol (—SH) groups to form a disulfide linkage S—S . This drug-loading approach displays many advantages over the traditional immersion method, such as increased loading efficiency, reduced burst release, and a drug release profile controlled by internal *stimuli*.^[126] It also displays disadvantages, however, among whom the necessity of introducing —SH groups in the drug chemical structure to form the S—S bond. Drug modifications are generally discouraged because they may affect the interaction of the drug with its target, compromise pharmacodynamics, and reduce therapeutic efficacy.^[127]

By contrast, chemical modification, such as the introduction of —SH groups, can be easily performed in oligonucleotide-based therapeutics, such as the PNA. PNAs are synthetic mimics of DNA in which the deoxyribose phosphate backbone is replaced by a pseudo peptide skeleton to which the nucleobases are linked.^[128] Chemical modifications, such as functional groups, can be easily introduced at either the —C or —N terminus of the sequence without affecting the hybridization efficiency with the target. PNA binds to complementary DNA /RNA with higher efficiency and greater specificity than conventional oligonucleotides, due to its neutrally charged backbone and resistance to nucleases and proteases.^[129] An example of redox-responsive DNPs delivering a PNA targeting an immune checkpoint modulator in cancer cells is reported in **Fig.11**. The nanocarriers were first modified by a —SH terminal PEG, and then the —SH-modified PNA was loaded inside DNPs through the formation of a S—S bond. The increased concentration of GSH inside cancer cells (2-20 mM) triggered the release of PNA upon reduction of the S—S and regeneration of —SH.^[65]

The key point of such a drug-loading approach relies on the significant difference in the concentration of GSH levels between the outer and inner cancer environments. Due to the altered equilibrium between the two sites, the disulfide bond reduction is more likely to happen inside cancer cells, thus improving the concentration of the delivered drug in the tumor environment. Accordingly, this method may reduce the uptake of PNA in healthy cells, where, instead, immune checkpoints are essential for the maintenance of homeostasis and prevention of autoimmunity.^[130]

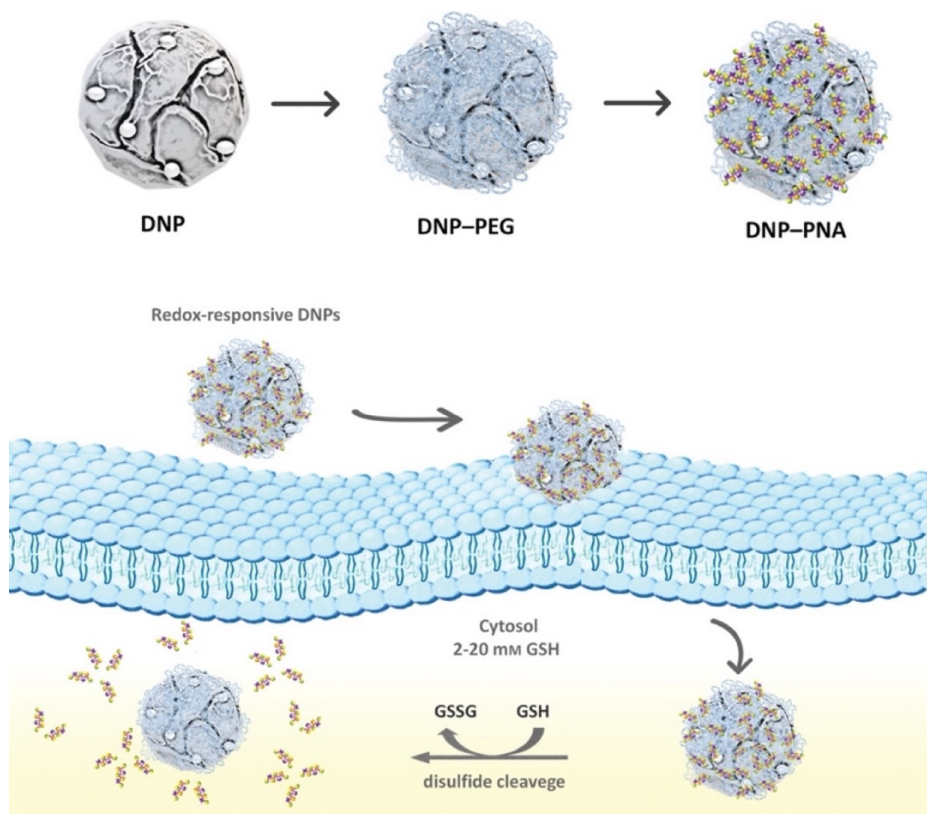


Figure 11. Scheme of redox-responsive DNPs' functionalization and drug release profile. The increased concentration of GSH in cancer cells causes the cleavage of the disulfide bond between the DNPs and PNA and the release of PNAs in cancer cells. Reproduced with permission from John Wiley and Sons, Copyright © 2021.^[65]

1.7 Hybrid multifunctional DNPs as label-free drug monitoring platforms

In paragraph 1.2 the term “hybrid” was used to describe NPs with both organic and inorganic features, such as liposomes containing gold NPs, or polymeric micelles encapsulating metal NPs. However, the word hybrid can also be used in another sense to describe NPs composed of more than

one type of inorganic nanomaterial. Several examples of hybrid inorganic NPs can be found in the literature, including the well-known AuroLase[®] made of silica-gold nanoshells, or silica composites with silver NPs for antibacterial purposes.^[34] Hybrid inorganic NPs display properties related to both the inorganic materials they are made of, being multifunctional and displaying many advantages over non-hybrid inorganic NPs. Silica NPs, to give an example, have incredible properties as nanocarriers, such as the drug-loading efficiency, but they have neither photoluminescent nor optical features. Due to this, they are suitable as nanocarriers but require a labeling approach for imaging purposes. On the contrary, inorganic nanomaterials such as gold, silver, iron, and quantum dots, display optical, magnetic, and photoluminescent properties, which make them ideal candidates for imaging purposes. Gold NPs, in particular, have been widely investigated for photothermal, photoacoustic, and surface-enhanced Raman scattering (SERS) imaging due to their optical properties.^[19,131] Therefore, the advantageous combination of silica and gold NPs allows for the fabrication of a platform with optical features for imaging purposes and drug-loading and release capabilities for therapy. The localized surface plasmon resonance (LSPR) effect and enhanced electromagnetic field (SERS) are worth-noting properties of gold NPs, making them the most exploited material for sensing applications. The LSPR effect is a surface plasmon resonance phenomenon of the noble metal nanomaterials, which is dependent on the composition, shape, size, and micro-environmental medium.^[132] SERS is a powerful vibrational technique arising from the strong amplification of electromagnetic fields generated by LSPR.^[133] The Raman signals of molecules absorbed on gold

NPs are enhanced by several orders of magnitude, allowing for the monitoring and sensing of biomolecules with incredibly low limits of detection. **Figure 9** describes the fabrication of a hybrid inorganic system composed of DNPs and gold NPs acting as both nanocarrier and nanosensor with two functionalities: (i) release of galunisertib in CRC and (ii) label-free monitoring and quantification of drug release *via* SERS.^[29] The gold NPs are in-situ synthesized *via* chemical reduction of gold salts on the surface of DNPs, which are further loaded with galunisertib and covered by a layer of crosslinked gelatin (**Fig. 9**). Gold NPs provide a highly sensitive SERS readout of galunisertib with non-invasive laser illumination exciting their plasmonic resonance, allowing for the monitoring of NPs' internalization and drug release quantification. The fabrication of nanocarriers with optical features for label-free drug monitoring offers a key advantage over the traditional photoluminescence-based approaches. The SERS readout intensity is independent of cell conditions, such as pH and temperature, which, instead, can affect the intensity of fluorescence signals.^[134] As a consequence, the SERS signal is more reliable than fluorescence for real-time analysis in living cells, avoiding under/overestimation of the released drug. Moreover, hybrid silica-gold systems allow for the monitoring of surface modifications by a simple absorption measurement rather than time-consuming and expensive techniques, such as the transmission electron microscopy (TEM). The LSPR of gold NPs is influenced by changes in refractive index in the surrounding medium, which generally happen upon NPs' functionalization. Due to this, in hybrid gold-DNPs systems covered by gelatin (**Fig. 9**), the polymeric shell surrounding gold NPs causes a change

in the local refractive index and a redshift of the LSPR peak, which can be monitored spectroscopically.^[61] The assessment of surface functionalization *via* UV-Visible (UV-Vis) spectroscopy is dramatically faster and cheaper than TEM imaging, and, most importantly, does not require specialized personnel to run the equipment. Furthermore, the LSPR shifts of gold NPs can be correlated to the thickness of the gelatin shell through a theoretical model, providing a correlation between the amount of loaded drug and gelatin, which influences the drug release profile. Likewise, the degradation of gelatin in cancer cells and consequent drug release results in a blue shift of the LSPR peak, which can be monitored as well.^[61]

The increasing interest in the development of label-free platforms with lower limits of detection has brought gold-decorated biosilica to the attention of researchers, as demonstrated by the increasing numbers of papers reporting both the DNPs and frustules as substrates.^[135] Among them, hybrid gold-DNPs were already tested in cancer cells revealing their safety, thus leading the way to their application as both nanosensors and nanocarriers.

CHAPTER II

Aims

2. Aims

Drug delivery is the most exploited area of nanomedicine and holds the promise of improving the quality of life for millions of patients suffering from unspecific, painful, and aggressive cancer treatments. Nanotechnology has opened up new avenues in the management of different diseases and, over the past years, DNPs have contributed to the development of advanced drug delivery systems for cancer treatment. The increasing knowledge of DNPs' surface modification has promoted the design of diverse functionalization approaches for the fabrication of both DNP-based nanocarriers and nanosensors. Moreover, the possibility to encapsulate DNPs in pH-responsive polymers and modify them with targeting agents offers a set of exciting opportunities for site-specific sustained drug delivery.

The following dissertation describes the development of multifunctional DNPs loaded with different anticancer agents, coated with pH-responsive polymers of varying nature, and functionalized with ligands to target cancer cells. Different fabrication methods, characterization techniques, and drug release strategies are described as means to ensure the potentiality of DNPs for the treatment of cancer.

The aims of the following thesis are:

1. To develop hybrid active-targeted nanocarriers with *site-specific* drug delivery and *real-time monitoring* functionalities. The nanocarrier consists of galunisertib-loaded DNPs decorated with gold NPs, covered by pH-responsive gelatin, and modified with antibodies targeting the L1-CAM on CRC cells. Active targeting

approaches increase the uptake of NPs and release of drugs in the targeted cells, reducing undesired effects. The enhancement of galunisertib Raman signal provided by gold NPs allows for the real-time monitoring of drug release in living cells and label-free *in vivo* imaging by SERS.

2. To improve the drug-loading capacity of hybrid DNPs through the formation of gelatin shells, whose thickness can be calculated by reverse engineering analysis of the hybrid nanosystem LSPR. A higher drug-loading efficiency enables lowering the administered concentration of nanocarriers, reducing the risk of systemic toxicity.
3. To exploit a microfluidic approach for the encapsulation of galunisertib-loaded active-targeted DNPs in a gastro-resistant coating for oral administration. The oral route is highly suggested for the treatment of CRC because it allows for the accumulation of the NPs in the lower intestine and localized release of galunisertib. Moreover, the oral route may overcome challenges associated with the intravenous injection of DNPs, such as blood clearance, clogging, systemic distribution and side effects.
4. To develop redox-responsive DNPs for the controlled release of a PNA targeting the programmed cell death 1 receptor/ ligand 1 (PD-1/PD-L1) immune checkpoint in cancer cells. The different concentration of GSH between healthy and tumor cells is here exploited for the development of a *stimuli*-responsive PNA nanocarrier.

Overall, the different functionalization approaches described in the present thesis aimed at a common goal: propose nanomedicine-based strategies to concentrate the release of anticancer agents in targeted malignant cells, thus reducing off-target effects and toxicity.

CHAPTER III

Methods

3. Methods

3.1 Sonication, purification, production, and aminosilanization of diatomite nanoparticles (DNPs)

To produce DNPs, the diatomite powder was dispersed in ethanol and mechanically crushed. The powder was then collected and ultrasonicated with a tip-sonicator (Sonics Materials VC 750) with a 40% amplitude (750 Watt and 20 kHz) for 90 h. The obtained DNPs were collected by centrifugation (15000 rpm) and washed in water. The purification process was performed by dispersing DNPs in a piranha solution made of a 4:1 mixture of concentrated H₂SO₄ and 30%_{w/v} H₂O₂ to remove traces of organic contamination. Then, DNPs were purified with HCl overnight to remove residues of metal oxides. The purified DNPs were extensively washed with H₂O and collected by centrifugation (15000 rpm). Afterwards, the DNPs were suspended in a 10% v/v APTES ethanol solution for 1 h at room temperature under mild stirring (500 rpm) in dark conditions. Finally, they were collected by centrifugation, the supernatant was removed, and DNPs were washed with ethanol. Amino-modified DNPs underwent a curing process for 1h at 50°C and were characterized.

3.2. Preparation of galunisertib-loaded gelatin-covered hybrid DNPs (DNPs-AuNPs-LY@Gel) modified with the anti-L1-CAM antibody

The first step in the preparation of the hybrid nanosystem was the in-situ synthesis of the gold-decorated-DNP complex (DNPs-AuNPs). To this aim, 0.125 mg of amino-modified DNPs were dispersed in 1×10^{-3} M chloroauric acid (HAuCl₄) aqueous solution (2.5 mL) and mixed under mild stirring for 10 min. To this solution, dicarboxylic polyethylene glycol (PEG, 0.2 mL) was added and vigorously stirred for 5 min. Finally, 0.015

mL of 0.1 M sodium borohydride (NaBH_4) aqueous solution was added at once. The color of the dispersion turned from yellow to red when NaBH_4 was added to the solution, confirming the reduction of gold salts and the formation of gold NPs (AuNPs) on the surface of the DNPs. The prepared dispersion of DNPs-AuNPs was centrifuged to remove the excess reagents at 3500 rpm for 10 min, the supernatant was discarded, and the residue was vigorously washed with Milli-Q H_2O . The second step of functionalization consists of galunisertib (herein abbreviated as LY) loading in DNPs-AuNPs and gelatin capping. To this aim, DNPs-AuNPs were soaked in a 10% acetone drug solution 5-fold more concentrated than the carrier and gently mixed at pH 2.5 for 2 h, 37°C . The drug-loading dispersion was centrifuged at 3500 rpm for 10 min and the supernatant with the unloaded drug was discarded. The DNPs-AuNPs-LY were mixed with a gelatin solution (1:2 weight *ratio*, respectively) in 10 mM 2-(N-Morpholino) ethane sulfonic acid hemisodium salt (MES) buffer pH 3.5 for 2 h. For gelatin crosslinking, an aqueous solution of 0.4 μM EDC and 0.1 μM N-hydroxy succinimide (NHS) was added to the NPs dispersion and stirred for 2 h at 37°C . The weight *ratio* between gelatin, EDC, and NHS was 1: 1.4: 0.2, respectively. After cross-linking, the gelatin-covered DNPs-AuNPs-LY system (DNPs-AuNPs-LY@Gel) was washed with Milli-Q H_2O and collected.

For the binding of the anti-L1-CAM antibody, protein A (pr-A) was covalently attached to the gelatin shell of the DNPs-AuNPs-LY@Gel to help the antibody orient the Fc fragment on the DNPs. To this aim, the NPs were suspended in a 0.1 mg mL^{-1} phosphate-buffered saline (PBS) solution of pr-A with 2 μM EDC and 0.8 μM NHS and stirred for 2 h (400 rpm).

Then, the suspension was centrifuged, the supernatant was removed, and the NPs were washed three times with PBS. Pr-A-modified DNPs-AuNPs-LY@Gel were then incubated with a $0.8 \mu\text{g mL}^{-1}$ anti-L1-CAM antibody for 2 h. Finally, the antibody-labeled formulation (DNPs-AuNPs-LY@Gel-Ab) was washed with H_2O , centrifuged, and collected.

3.3 Improvement of the galunisertib loading capacity of plasmonic DNPs via the formation of gelatin shells of varying thicknesses

This section describes an alternative approach to synthesizing a plasmonic nanocarrier made of DNPs and AuNPs and further capped by gelatin shells. In this protocol, the AuNPs on the surface of DNPs are stabilized by gelatin rather than dicarboxylic PEG. To discriminate between the plasmonic substrate described in section 3.2 (DNPs-AuNPs) and the one described herein, the DNPs decorated by gelatin-stabilized AuNPs (gel-AuNPs) are abbreviated as (AuDNPs). The main difference between the protocols described here and in section 3.2 are: (i) the use of gelatin rather than dicarboxylic PEG to stabilize AuNPs, (ii) the use of different concentrations of gelatin to promote the formation of shells of varying thickness on the surface of AuDNPs, (iii) the use of gelatin as both the AuNPs stabilizer and coating material, providing additional features and functionalities to the hybrid nanocarrier.

To produce AuDNPs, a dispersion of amino-modified DNPs was immersed in 10^{-3} M HAuCl_4 solution and stirred for 5 min. A 0.025% gelatin aqueous solution was then added to the dispersion to stabilize AuNPs (weight *ratio* between gold salts and gelatin 10:1). The dispersion was stirred for further 5 min and 100 mM aqueous solution of NaBH_4 was added dropwise until the color of the dispersion turned from yellow to

purple/red. AuDNPs were left to rest for 30 min and purified by centrifugation (4500 rpm, 10 °C, 10 min). Then, the gelatin stabilizing AuNPs was cross-linked using a mixture of EDC and NHS in PBS (weight *ratio* gelatin: EDC: NHS 10:14:7) for 90 min to weld AuNPs to the silica substrate. The loading of galunisertib in the hybrid system (AuDNPs-LY) was performed by dispersing NPs in 1 mg mL⁻¹ galunisertib solution for 2 h at 37 °C. The excess of the unloaded drug was discarded by centrifugation at 4500 rpm, and the dispersion was washed twice. The loaded system was then resuspended in gelatin aqueous solutions pH 4.0 at the concentrations of 0.125%, 0.25%, 0.5%, 0.75% and 1.50% w/v. The mixture was stirred for 30 min and EDC and NHS were added for cross-linking the gelatin matrix for 1 h at room temperature (AuDNPs-LY@Gel_x, where *x* is the concentration of gelatin in the external shell). In this step, gelatin was used as a coating material, and we used an increasing concentration of gelatin to promote the growth of polymeric shells of varying thickness. Finally, the dispersion was centrifuged, and NPs were washed twice in H₂O and collected for analysis.

3.4 Development of redox-responsive DNPs for the GSH-triggered release of PNA in cancer cells

Redox-responsive DNPs were synthesized by dissolving APTES and PEG (1:1 *ratio*, 7.5 μmol of each molecule) in 0.1 mL of N, N-dimethylformamide (DMF) under constant stirring (800 rpm) for 16h at room temperature. When elapsed the time, 1 mg of bare DNPs was dispersed in the APTES–PEG/DMF solution under stirring, overnight at room temperature. The as-obtained pegylated DNPs (DNPs–PEG) were

centrifuged for 30 min at 15000 rpm, the supernatant was discarded, and the NPs were rinsed with DMF and MilliQ-H₂O. Finally, the DNPs-PEG were mixed with 0.1 μmol PNA (molar *ratio* NPs: PNA 5:1) in 0.5 mL of 4×10⁻⁴ M sodium dodecyl sulphate (SDS), 2×10⁻³ M EDTA, pH 7.6 at 30 °C, overnight under stirring. The PNA-conjugated DNPs-PEG (DNPs-PNA) were centrifuged for 30 min at 15000 rpm, the supernatant was removed, and the NPs were washed with MilliQ-H₂O.

3.5 Fabrication of the microfluidic platform for the encapsulation of antibody-modified DNPs (DNPs-Gel-Ab) in enteric coatings

For the encapsulation of the DNPs-Gel-Ab, a borosilicate glass capillary with a diameter of 1.0 mm (World Precision Instruments, Inc., USA) was tapered using a micropipette puller (P-97, Sutter Instrument Co., USA) to a diameter of 20 μm. The inner diameter (d_i) of the capillary was further enlarged to *ca.* 100 μm. The inner capillary was inserted into an outer capillary (d_i = 1.1 mm, Sutter Instrument Co., USA) and coaxially aligned. Two polyethylene tubes were attached to the microfluidic chip to flush the inner and outer phases at constant flow rates separately. A three-dimensional (3D) coaxial flow was achieved by simultaneously pumping the inner and outer solutions in the same direction at flow rates controlled by two pumps (PHD 2000, Harvard Apparatus).

3.6 Production of encapsulated-DNPs *via* glass capillary-based microfluidic technology

Antibody-labeled DNPs-Gel (DNPs-Gel-Ab) were loaded with galunisertib, coated with gelatin, and modified with the anti-L1-CAM antibody following the protocol described in section 3.2 and 3.3. The drug-loaded DNPs-Gel-Ab were encapsulated into hydroxy propyl methyl

cellulose acetate succinate (herein abbreviated as HPMC) using the microfluidics glass capillary technique.^[115,118] HPMC is a polymer commonly used for enteric coatings soluble at alkaline pH with an opening pH range between 5.5 and 6.5.^[96] The inner phase was injected through the inner capillary and consisted of 1 mg mL⁻¹ drug-loaded DNPs-Gel-Ab dispersed in 5 mg mL⁻¹ ethanol: water solution (50:50) of HPMC. The outer solution phase was injected in the outer capillary and consisted of 0.5 % w/v aqueous solution of polyvinyl alcohol (PVA) pH 6.7. The inner solution was injected at 1 mL h⁻¹, while the outer solution was pumped at 30 mL h⁻¹. The encapsulated-DNPs-Gel-Ab (herein abbreviated as encapsulated-DNPs) were collected from the end of the outer capillary under mild stirring (400 rpm), centrifuged (13200 rpm), and washed with H₂O to remove excess reagents.

3.7 Evaluation of the binding efficiency of protein and antibody anti-L1-CAM to the active-targeted DNPs-LY@Gel-Ab

To quantify the amount of pr-A and antibody anti-L1-CAM bound to the surface of DNPs-AuNPs-LY@Gel-Ab, we attached fluorescein isothiocyanate (FITC)-labeled pr-A (pr-A*) on the DNPs-AuNPs-LY@Gel. Then, pr-A*-modified DNPs-AuNPs-Gel were digested in a 70 µg mL⁻¹ trypsin solution for 1h at 37°C to degrade the gelatin shell and detach pr-A* from the NPs. The suspension was centrifuged, and the supernatant containing the degraded gelatin and pr-A* was analyzed by fluorometry using an external calibration method. The fluorescence emission of the detached pr-A* at 516 nm was interpolated in the pr-A* titration curve achieved by exciting the samples at 488 nm, and the number of molecules attached to the surface was calculated. For the quantification

of antibody binding efficiency, Alexa Fluor[®]-488-labeled anti-L1-CAM Ab* was bound to pr-A-modified DNPs-AuNPs-LY@Gel as described in 3.2. Then, the suspension was incubated with 2% SDS at 90°C for 15 min to denature pr-A and release the Ab* in the supernatant. The fluorescence intensity of Ab* at 519 nm was measured by a spectrofluorometer, the concentration was calculated using an external calibration method, and the number of attached antibodies was quantified. The efficiency of surface coverage (S) was calculated as moles (mol) of proteins per mass of DNP using the following equation:

$$S = mol_{Ab}/w_{DNP}$$

where mol is the moles of Ab and w is the weight of a single DNP (mol/g)

3.8 Physicochemical characterization of the developed formulations

Hydrodynamic diameter (ζ -average), polydispersity index (PDI), and ζ -potential of the developed NPs were measured using a Zetasizer ZS Nano instrument (Malvern Instruments Ltd., UK). The functionalization steps (decoration with AuNPs, gelatin coating, protein attachment, antibody labeling, and microfluidic encapsulation) were evaluated using a Bruker VERTEX 70 series Fourier transform infrared (FTIR) spectrometer (Bruker Optics, Germany) with a horizontal attenuated total reflectance (ATR) sampling accessory (MIRacle, Pike Technology, USA) with a resolution of 4 cm^{-1} . The analysis was performed with dried samples (0.5–1 mg) at room temperature. The morphology of bare DNPs, DNPs-AuNPs, DNPs-AuNPs-Gel, DNPs-Gel-Ab, DNPs-PEG, and encapsulated-DNPs was evaluated by transmission electron microscopy (TEM), using a TecnaiTM F12 microscope (FEI Company, USA). For this purpose, NPs

were dispersed in H₂O at the final concentration of 0.1 mg mL⁻¹, pipetted on copper-coated grids, left to dry at room temperature and analyzed. The fluorescence of labeled formulations was assessed by fluorescence microscopy (Leica Microscope) by drying 0.05 mg of NPs suspension on either glass slides or silicon wafers. The images were acquired in fluorescence, dark field (DF) or bright field (BF) conditions, according to the needs.

The encapsulation of the DNPs-Gel-Ab in HPMC was assessed using an Oxford INCA 350 EDX spectrometer connected with a field emission scanning electron microscope (FESEM; Hitachi S-4800, Japan). The measurement points were selected from areas imaged with the bright field TE detector of the FESEM. The UV-Vis spectra of bare DNPs, DNPs-PEG, DNPs-AuNPs, DNPs-AuNPs@Gel, and DNPs-AuNPs@Gel-Ab were recorded on Cary 100 UV-Vis double beam spectrophotometer (Agilent, CA, USA) using quartz cells of 10 mm path at room temperature. Samples were dispersed in deionized H₂O. The peak analysis was performed by OriginPro 2016 (Origin Lab, Northampton, MA, USA).

3.9 NMR Spectroscopy standard ¹H NMR experiments

The solution ¹H proton nuclear magnetic resonance (NMR) data was collected by a Bruker Advance III 700 spectrometer (Bruker BioSpin GmbH, Rheinstetten, Germany), operating at 700 MHz. The samples APTES (0.01–7.5 μmol in 0.6 mL of DMF-d), OPSS-PEG-NHS (0.010–7.5 μmol in 0.6 mL DMF-d), APETS/PEG complex (*ratio* 1:1, 7.5 μmol of each molecule in 0.6 mL DMF-d), and PNA (0.01 μmol in 0.6 mL DMF-d) were analyzed using standard ¹H NMR protocol (128–256 scans, 2 dummy scans, 1 s relaxation delay). For qNMR, dried modified-DNPs

were dispersed in 0.6 mL DMF-d or D₂O, sonicated in an ultrasonic bath for 60 s, transferred to an NMR tube (5 mm), and characterized by NMR (256 scans, 2 dummy scans, 6 s relaxation delay). The fumaric acid (10 mg mL⁻¹ in DMF) with resonance at 6.64 ppm was used as an internal standard and approximately 0.005–0.05 mL of the prepared solution of DNPs sample was used for each analysis.

NMR spectra were processed by MestReNova software (Mestrelab Research, S.L., Spain). After Fourier transformation, the chemical shift was referenced by the residual signal of DMF-d₇ used as a solvent (a broad peak centered at 8.03 ppm). The phase was corrected automatically. The baseline was corrected by a fifth-order polynomial fit with a manually adjusted filter. To calculate the functionalization yield, the signals of the compound of interest were compared with those of the fumaric acid.

3.10 *In vitro* drug-loading capacity and release studies

For the investigation of DNPs' drug-loading capacity (LC) and release profile, different approaches were exploited according to the features of the developed formulation. However, a common quantification method based on reversed-phase high-performance liquid chromatography (RP-HPLC) was used to measure the amount of loaded and released galunisertib.

- The galunisertib LC of DNPs-AuNPs-LY@Gel was determined by immersing the drug-loaded formulations in 1 mL of PBS pH 5.5 for 60 h. The NPs were then centrifuged, and the supernatants were collected and analyzed by RP-HPLC. *In vitro* release tests were performed by shaking DNPs-AuNPs-LY@Gel in PBS pH 5.5 and 7.4 at 37 °C. At predetermined time intervals (0, 5, 16, 24, 48, 60

h) the release solution was centrifuged (3500 rpm) for 5 min, and the supernatant was collected and replaced with fresh PBS until the subsequent sampling time. The collected supernatants were filtered through a syringe-filter 0.22 μm (Millex- GS, Merck, Darmstadt, Germany) and analyzed by RP-HPLC.

- For the determination of the LC of DNPs-AuNPs-LY@Gel_x having shells of different thicknesses, NPs were dispersed in 0.06 mg mL⁻¹ trypsin PBS solution pH 7.4 for 2 h to promote the degradation of the gelatin shell. The NPs were then centrifuged, and supernatants were analyzed. The drug release profile was studied by dispersing NPs in the same media and analyzing the supernatants at different time points (5, 10, 20, 30, 60 min, 16 h) by RP-HPLC.
- The galunisertib LC of encapsulated-DNPs was measured by dispersing the NPs in 70% ethanol solution for 4 h under stirring (400 rpm) to dissolve the HPMC matrix. The dispersion was centrifuged (13200 rpm), the supernatant was collected, and the DNPs-Gel-Ab obtained by the HPMC dissolution were dispersed in 1mL of PBS pH 7.2 for 8 h. Trypsin (0.06 mg) was added to the above solution to degrade the gelatin matrix and favor the release of galunisertib. After 8 h, the DNPs-Gel-Ab were centrifuged, and the released drug was quantified by RP-HPLC. For the *in vitro* drug release studies, the encapsulated-DNPs were dispersed in buffers mimicking the GI tract (stomach, intestine, and colon), such as the simulated gastric fluid (SGF) pH 1.6 and fasted-state simulated intestinal fluid (FaSSIF), pH 5.5 and 8.0. The SGF solution consisted of 0.2% w/v sodium chloride (NaCl) and 0.7% v/v HCl,

to which 1 mg mL⁻¹ pepsin was added to mimic the presence of digestive enzymes. The FaSSIF solutions consisted of 106 mM NaCl, monobasic sodium phosphate, 8.7 mM sodium hydroxide, 3 mM sodium taurocholate, and 0.75 mM lecithin. The pH of FaSSIF solutions was adjusted to 5.5 and 8.0, and trypsin (0.06 mg mL⁻¹) was added to mimic the intestine and colon composition. Encapsulated-DNPs were dispersed in SGF-pepsin⁺ for 2 h at 37°C and under stirring (400 rpm). Then, the dispersion was centrifuged (13200 rpm), the supernatants were collected at different time points (5, 15, 30, 60, and 120 min), and the NPs resuspended in pre-warmed fresh buffer. After 2 h, the NPs were removed from the SGF solution by centrifugation and dispersed in FaSSIF-trypsin⁺ pH 5.5 for 4 h at 400 rpm. The supernatants were collected at different time points (5, 15, 30, 60, 120, 180, and 240 min) by centrifugation and analyzed. Finally, encapsulated-DNPs were dispersed in FaSSIF-trypsin⁺ pH 8.0 for 2 h at 400 rpm. The NPs were centrifuged at different points (5, 15, 30, 60, and 120 min) to collect the supernatant and calculate the released drug by RP-HPLC.

- For the quantification of the efficiency of PNA conjugation to DNPs-PNA, the PNA was labeled with FITC (DNPs-PNA*) and the released drug upon breaking of the disulfide bond was quantified by fluorescence spectroscopy. DNPs-PNA* (0.1 mg) were immersed into 1 mL of PBS pH 7.4 and 5.5 without or with DTT (0.02 and 0.1M) at 37 °C for 48 h under mild stirring. After the release test, an excess of DTT (100 mm) was added to the NP

suspension to promote the complete release of the PNA*. The NPs were removed by centrifugation, and the released PNA* was quantified by a spectrofluorometer (FP-8250, Jasco Europe, Italy). The amount of PNA was quantified comparing the fluorescence intensity of the supernatant at 520 nm with a known concentration of PNA-FITC used as a standard. *In vitro* release tests were performed by shaking the DNPs–PNA* (0.1 mg) into PBS buffer (1 mL, pH 7.4) without or with DTT (0.02 and 0.1 M) at 37 °C for 48 h under mild stirring. At predetermined time intervals, the release solutions were centrifuged at 15000 rpm for 5 min, the supernatants were collected and replaced with fresh buffer until the subsequent sampling time. The collected supernatants were analyzed by spectrofluorometer according to the described method.

For the quantification of the released drug by RP-HPLC, a Discovery® C18 Column (Merck, DE) was used as a stationary phase (5 µm particle size, 150 × 4.6 mm). Mobile phase A comprised TFA 0.02% v/v in H₂O, whereas mobile phase B was TFA 0.02% v/v in acetonitrile (ACN). The flow rate and wavelength were set at 1 mL min⁻¹ and 254 nm, respectively. The amount of loaded/released drug was quantified using an external calibration method and the LC was determined using Equation 1:

$$LC (\%) = \frac{\text{drug released at time } t}{\text{total amount of drug loaded}} \times 100 \quad (1)$$

The cumulative drug release was measured using Equation 2:

$$\text{Cumulative release}(\%) = P(t - 1) + Pt \quad (2)$$

where Pt is the percentage of the released drug at time t and P(t–1) is the percentage of drug quantified at the previous time.

3.11 Stability studies of encapsulated-DNPs

The stability of the formulation in water-based solutions was evaluated by immersing the encapsulated-DNPs 1 mg mL^{-1} in MES buffer 10 mM pH 4.5 for 36 h at room temperature. The HPMC coating on the encapsulated-DNPs starts dissolving at pH between 5.5 and 6.5, therefore MES pH 4.5 was selected as a buffer to avoid HPMC dissolution. For the stability studies, 0.05 mg of encapsulated-DNPs were taken from the dispersion at different times (0, 6, 12, 24, and 36 h) and analyzed by DLS at the final concentration of 0.05 mg mL^{-1} .

3.12 Raman and SERS microscopy: set up experiment and SERS gain measurement

Raman and SERS imaging were obtained from an inverted confocal Raman microscope (Xplora Inv, Horiba – Jobin Yvon, equipped with three laser lines at 532, 638, and 785 nm) using the laser line at 638 nm (50 mW, He-Ne) as the pump wavelength and a $60\times$ water immersion objective lens (Nikon, NA = 1.2, WD = $300 \mu\text{m}$). The slit aperture of the spectrometer and the confocal pinhole were $100 \mu\text{m}$. Rayleigh's backscattered light was filtered out with a notch filter. The beam waist was measured with a knife-edge method detecting the Raman band at 514 cm^{-1} of a Si wafer blade and provided the value of about $0.7 \mu\text{m}$ at 638 nm. To compare the Raman signal of galunisertib with SERS signal enhancement from the DNPs-AuNPs-LY@Gel complex, the SERS gain “G” was calculated as the *ratio* of the SERS signal intensity for the drug band at 1360 cm^{-1} (I_{SERS}) and the Raman intensity of the same band (I_{Raman}), normalized to the different powers (P_{SERS} , P_{Raman}), integration times (t_{SERS} , t_{Raman}) and molecular concentrations (c_{SERS} , c_{Raman}), as shown in equation 3.

$$G = \frac{\frac{I_{SERS}}{t_{SERS} \times C_{SERS} \times P_{SERS}}}{\frac{I_{Raman}}{t_{Raman} \times C_{Raman} \times P_{Raman}}} \quad (3)$$

3.13 Galunisertib release from the DNPs-AuNPs-LY@Gel *in vitro* and living cells by SERS

For drug Raman spectroscopy, a drop (3 μL) of 5 mg mL^{-1} drug acetone solution was deposited on a calcium fluoride (CaF_2) slide and dried. The galunisertib Raman spectrum was acquired by using a laser at 638 nm, with 40 mW power and 1 s of acquisition time. 3 μL of 0.5 mg mL^{-1} suspension of DNPs-AuNPs-LY@Gel was deposited on a CaF_2 coverslip and left to dry. The SERS spectrum of galunisertib was recorded by using a laser power of 1 mW and an acquisition time of 1 s.

For the *in vitro* release tests, 3 μL of 0.5 mg mL^{-1} DNPs-AuNPs-LY@Gel in PBS was deposited on a CaF_2 slide. The DNPs-AuNPs-LY@Gel suspension covered a circular area of 20 mm^2 (radius 2.5 mm), yielding a concentration of 250 ng mm^{-2} . The area occupied by a single cluster of DNPs-AuNPs-LY@Gel was 1 μm^2 , with a total mass of nanocomplex 75.0 fg carrying 1.5 fg of galunisertib. A single DNP-AuNPs-LY@Gel particle had a radius of 225 nm and an area of 0.16 μm^2 . So far, each cluster of 1 μm^2 comprised ~6 DNPs. Each DNP had a mass of about 12 fg, and the loaded drug mass was 0.25 fg. Having the molecular weight of galunisertib known (369.42 g mol^{-1}), we estimated that 106 molecules of the drug were loaded on a single cluster before release started (t_0).

After deposition and drying, the DNPs-AuNPs-LY@Gel were immersed in two different PBS solutions 5.5 and 7.4 pH, respectively. The drug SERS spectra were recorded at different times up to 48 h using a 638 nm

laser. The residual mass of the drug on the single DNP after being dispersed for 24 h in PBS pH 7.4 and 5 was calculated by the drug release curves.

For live-cell SERS experiments, cells were seeded in 35 mm dishes and incubated the day after with a 0.05 mg mL^{-1} dispersion of DNPs-AuNPs-LY@Gel in phenol red-free Dulbecco's Modified Eagle's Medium (DMEM, 0.5 mL) for 0, 2, 18, 24, 42, and 48 h. At each time point, SERS spectra of the released drug in cells were acquired by using a laser power of 1 mW and acquisition time of 1 s. The drug release was monitored by analyzing the intensity of the band at 1380 cm^{-1} . For each time point, SERS spectra were collected from 30 cells and the experiment was repeated 3 times. The total mass of DNPs incubated was 0.075 mg and the total mass of loaded drug was 1.5 μg . The mass of galunisertib for a single DNP was 0.25 fg.

3.14 Cell lines and culture conditions

The human colon adenocarcinoma Caco-2, LS-174T, and SW620, human lung carcinoma A549, breast cancer MCF-7 and MDA-MB-231, and glioblastoma U87MG cells were obtained from the American Type Culture Collection (ATCC, USA). The human goblet-like HT29-MTX was kindly provided by Dr T. Lesuffleur (INSERM U178, Villejuif, France). Caco-2, HT29-MTX, A549, MCF-7, and U87MG cells were grown separately in tissue culture flasks (Corning Inc., USA) with high-glucose DMEM supplemented with 10% *v/v* heat-inactivated fetal bovine serum (FBS), 1% *v/v* L-glutamine, 1% *v/v* non-essential amino acids (NEEA), 1% *v/v* and antibiotic-antimitotic mixture (final concentration of Penicillin and Streptomycin PEST 100 IU mL^{-1}). The SW620 and LS-174T cells were

cultured in tissue flasks with high glucose DMEM supplemented with 10% v/v FBS, 1% v/v L-glutamine, and 1% v/v PEST. Cells were kept in the incubator (16 BB gas, Heraeus Instruments GmbH, Germany) at 37 °C and 5% CO₂ in a water-saturated atmosphere. The MDA-MB-231 cells were cultured in 10% FBS Roswell Park Memorial Institute 1640 medium (RPMI), supplemented with 1% PEST, 1% L-glutamine, and 1% NEEA. For each cell line, the culture medium was replaced every other day and sub-culturing was performed at 80% confluency for all the cell lines using trypsin-PBS-EDTA.

3.15 Cell viability assays

- **Viability of LS-174T, SW620, and CRL-1790 cells with the DNPs-AuNPs-LY@Gel system**

Cells at the density of 3×10^4 cells/well were seeded separately into 96-well plates and allowed to attach for 24 h. Then, the cells were treated with DNPs-AuNPs-LY@Gel dispersions (12.5, 25, 50, and 100 $\mu\text{g mL}^{-1}$), DNP-AuNPs-LY (50 $\mu\text{g mL}^{-1}$), DNPs-AuNPs (50 $\mu\text{g mL}^{-1}$), DNPs-AuNPs@Gel (50 $\mu\text{g mL}^{-1}$), DNPs-AuNPs-LY@Gel-Ab (20 $\mu\text{g mL}^{-1}$), and galunisertib (2.5×10^{-6} M), for 24 and 48 h. Cell viability was determined using the CCK-8 assay kit according to the manufacturer's instructions (Dojindo). Positive and negative controls were obtained by incubating the cells with 1% Triton X-100 and HBSS-HEPES buffer, respectively. The plates were shaken for 5 min, and the luminescence was measured using a Varioskan Microplate Reader (ThermoFisher Scientific, USA).

- **Viability of Caco-2, HT29-MTX, and SW620 cells with the encapsulated DNPs**

The cell viability of Caco-2, HT29-MTX, and SW620 was evaluated with the CellTiter-Glo[®] luminescent cell viability assay, measuring the amount of ATP produced by living cells. Cells (5×10^5 cells mL⁻¹) were seeded separately into 96-well plates and allowed to attach for 24 h. Then, the cell culture medium was removed, and DNPs, DNPs-Gel, DNPs-Gel-Ab, and encapsulated-DNPs were incubated with Caco-2, HT29-MTX, and SW620 cells at different concentrations (12 - 100 $\mu\text{g mL}^{-1}$) for 6 and 24 h at 37 °C, 5% CO₂. After incubation, cells were washed twice with HBSS and HEPES, and then incubated with 0.1 mL of CellTiter-Glo[®] (prepared in HBSS–HEPES buffer *ratio* 1:1). Positive and negative controls were obtained by incubating cells with 1% Triton X-100 and HBSS–HEPES, respectively. The plates were shaken for 5 min, and the luminescence was measured using a Varioskan Microplate Reader.

- **Viability of A549, and MDA-MB-231 cells with the DNPs-PEG formulations**

The A549 and MDA-MB-231 cells were seeded in 96-well plates at the density of 1×10^4 cells/well in 10% FBS DMEM (for A549 cells) or 10% FBS RPMI (for MDA-MB-231 cells). The plates were then placed back in the incubator for 24 h to allow the complete attachment of the cells. We then removed the medium and replaced it with 0.1 mL of modified DNPs-PNA at the concentrations of 25, 50, 100, and 200 $\mu\text{g mL}^{-1}$ for 24, 48, or 72 h.

The PNA was incubated with cells at concentrations of 0.00125, 0.0025, 0.005, and 0.01 μmol in a complete medium for 24, 48, or 72 h. Then, we removed the samples from the wells and washed the cells with HBSS-HEPES pH 7.4. The intracellular ATP concentration was measured by CellTiter-Glo[®] assay and correlated to cell viability. The luminescence was read in a Varioskan Lux plate reader. The cells incubated with complete medium (10% of FBS DMEM or 10% of FBS RPMI) represented the negative control, while the cells incubated with 1% Triton-X 100 were used as the positive control.

3.16 RNA preparation and real-time PCR

Total RNAs from human colon cancer cells were extracted with the Eurogold TRIFAST kit (Euroclone) according to the manufacturer's instructions. One microgram of total RNA was used for cDNA synthesis with high-capacity reverse transcriptase (ThermoFisher). Quantitative real-time PCR (qPCR) was performed using the SYBR Green PCR master mix (ThermoFisher), according to the manufacturer's instructions. The list of utilized primers is reported in the Supporting Information of the manuscript.^[29]

3.17 Confocal fluorescence imaging

- **Internalization studies of DNPs-AuNPs-LY@Gel in LS17-4T cells**

The DNPs-AuNPs (0.1 mg) were dispersed in a 20 $\mu\text{g mL}^{-1}$ Alexa Fluor[®]-488 PBS solution and gently mixed with EDC (3.5×10^{-6} M) and NHS (0.3×10^{-6} M) for 90 min at room temperature. Then, the DNPs-AuNPs* were loaded with galunisertib and capped by

crosslinked gelatin according to the aforementioned procedure. For microscopy imaging, 12-mm glass coverslips were incubated with poly-L-Lys (0.01% v/v) for 10 min at room temperature to promote cell adhesion. LS-174T cells (5×10^4) were plated on the top of the coverslips and left to adhere for 24 h. Then, the DNP-AuNPs*-LY ($50 \mu\text{g mL}^{-1}$) and DNP-AuNPs*-LY@Gel ($50 \mu\text{g mL}^{-1}$) were added to the wells with serum-free DMEM and incubated for 24 h at 37 °C. As a control, the cells were incubated with PBS 1×. The fluorophore concentration for labeling was chosen considering a functionalization efficiency of 10% (data not shown here). The cells were washed with PBS buffer and fixed by 4% v/v paraformaldehyde (PFA) for 10 min in the dark. Cells were washed with PBS and the cell membrane was stained by $2 \mu\text{g mL}^{-1}$ wheat germ agglutinin (WGA) Alexa Fluor[®]-555 conjugate for 10 min at 37 °C and washed again. Finally, the cell nuclei were stained with $1 \mu\text{g mL}^{-1}$ 4',6-diamidino-2-phenylindole (DAPI) in PBS solution for 10 min and washed. An inverted confocal fluorescence microscope (ZEISS LSM-700) with appropriate filters was used to evaluate the cell uptake of the DNPs.

- **Internalization studies of active-targeted encapsulated in Caco-2, HT29-MTX, and SW620 cells**

Caco-2, HT29-MTX and SW620 cells were seeded at the density of 2×10^5 cells mL^{-1} in Lab-Tek[™] 8-chamber slides (Ibidi) separately and allowed to attach for 24 h in a humidified atmosphere. Then, the medium was discarded, and cells were incubated with 0.05 mg of Alexa Fluor[®] 488-labeled DNPs-Gel,

DNPs-Gel-Ab, and encapsulated-DNPs in DMEM for 24 h. The fluorophore labeling was performed according to the protocol described previously. After reaching confluency, the cells were washed twice with HBSS-HEPES, fixed by 1% v/v PFA, and nuclei and membrane were stained with DAPI and CellMask™ Deep Red, respectively. Finally, the cells were washed and suspended in fresh PBS and analyzed by Leica SP5 II HCS-A confocal microscope (Leica Microsystems, Wetzlar, Germany).

- **Internalization studies of DNPs-PEG in MDA-MB-231 and A549 cells**

We seeded 1×10^5 cells in 12-well plates and placed them back in the incubator for 24 h to allow for a complete attachment. Then, we removed the medium and added the DNPs*-PEG and PNAs at the concentration of $50 \mu\text{g mL}^{-1}$ and incubated them for 12 or 24 h. Upon each time-point, the samples were removed from the wells and the cells were washed twice with PBS. Then, we stained the cells with Cell Mask deep red, followed by fixation by 4% PFA. The nuclei were stained with DAPI. Finally, we washed the wells 4 times with PBS. The images were processed with Leica LASX Software.

3.18 Internalization of DNPs-AuNPs-LY@Gel in CRC cells by Raman spectroscopy

For Raman imaging, 12-mm-diameter CaF_2 coverslips were incubated with poly-L-Lys (0.01% v/v) for 10 min at room temperature to promote cell adhesion. Then, LS-174T cells were plated on the top of the coverslips and after 24 h a dispersion of 0.05 mg mL^{-1} DNPs-AuNPs-LY@Gel was

added into wells in duplicate and incubated for 12 and 24 h at 37 °C. Before acquiring a Raman image of the sample, LS-174T cells were washed with PBS 3 times, fixed with 2% v/v PFA for 10 min at room temperature and washed with PBS 3 times. The Raman image was recorded by raster scanning the fixed cell through the laser focus (638 nm, laser power 20 mW), with a step size of 0.5 μm, and acquiring a 2D array of Raman spectra on a selected area (exposure time 0.5 s/spectrum). A total of 1500/2000 spectra for each cell were collected. The chemical maps (false color Raman images) were generated using the multivariate curve resolution-alternative least square (MCR-ALS) method (HORIBA Scientific Lab Spec 6 software, Horiba Jobin Yvon, Villeneuve d'Ascq, France).

3.19 Cell uptake studies by fluorescence-assisted cell sorting (FACS)

- **Uptake of DNPs-PNA in MDA-MB-231 and A549 cells**

We assessed the quantitative cell uptake by flow cytometry (FCM) on a BD Accuri cytometer equipped with a C6 autosampler (BD Biosciences, USA). The samples were labeled introducing a FITC moiety on the PNA structure. We seeded 1×10^5 cells in 12-well plates and incubated them for 24 h to allow for a complete attachment. Then, the medium was removed, and cells were incubated with the samples at the concentration of $50 \mu\text{g mL}^{-1}$ for 6 or 12 h. Upon each time point, the medium was removed, and the cells were washed twice with PBS pH 7.4. The cells were then detached from the plate with a scraper, resuspended in cold PBS and transferred to a 96-well V-bottom plate. We centrifuged the cells at 300g for 5 min in an Eppendorf R5100 centrifuge tube

(Eppendorf, USA). The samples were washed twice with cold PBS, then the cells were resuspended in 0.2 mL of cold PBS. The samples were analyzed by Accuri™ C6. To distinguish between the fraction of samples associated with or taken up by the cells, we incubated the cells with 0.1 mL of 0.005% trypan blue for 5 min. Then, we washed the cells twice with cold PBS, before the samples.

- **Uptake of active-targeted encapsulated-DNPs in Caco-2, HT29-MTX, and SW620 cells**

Caco-2, HT29-MTX, and SW620 cells were seeded separately in a 24-well plate at a density of 1×10^5 cells/well and incubated for 24 h at 37°C. The cells were washed once with PBS pH 7.2 and incubated with 0.05 mg mL^{-1} Alexa Fluor® 488-labeled DNPs-Gel, DNPs-Gel-Ab, and encapsulated-DNPs in DMEM for 24 h. Cells were washed twice with PBS to remove the non-internalized NPs before detachment and centrifuged at 13200 rpm for 4 min. Then, cells were suspended in PBS in a 96-well V-Bottom plate separately and analyzed by FACS. For each condition, 2×10^5 cell events were measured and sorted by fluorescence in the FITC channel.

3.20 Quantification of the expression levels of the cell surface antigen L1-CAM

For this study, 3×10^5 Caco-2, HT29- MTX, and SW620 cells were detached with trypsin from the flasks, washed in PBS, and seeded separately in 96-well V-Bottom plates for FACS analysis. This technique can be used to complement the NP-cell interaction studies obtained by confocal microscopy.^[136] The cells were incubated with the anti-L1-CAM

primary antibody solution $6 \mu\text{g mL}^{-1}$ for 30 min at 4°C (0.1 mL 50:50 cells: antibody). Then, the cells were centrifuged, washed twice with PBS, and incubated with the secondary antibody m-IgGK BP-CFL-647 $2 \mu\text{g mL}^{-1}$ for 30 min at room temperature and under dark conditions. Control cells were incubated only with the secondary antibody to measure the binding unspecificity. Cells were sorted by fluorescence in the allophycocyanin (APC) channel with the AccuriTM C6 Plus Flow Cytometer. For each condition, a minimum of 2×10^4 events were measured. Flow cytometry data were analyzed using FlowJo.

3.21 Migration assay

For the investigation of Caco-2, HT29-MTX and SW620 migration, the cells were seeded separately into culture-inserts 2 well in μ -dishes 35 mm (Ibidi, IT) at a density of 8×10^4 cells/well in 10% FBS DMEM. The cells were left to adhere for 48 h and reach 95% confluency at 37°C and humidified atmosphere. After 48 h, the insert was removed, and the cells were washed and allowed to migrate in 0.5% FBS DMEM (control) under starvation. The efficacy of both the free and delivered galunisertib was investigated by adding either free galunisertib (LY) $2.5 \mu\text{M}$ or encapsulated drug-loaded DNPs (encapsulated DNPs-LY, $26 \mu\text{g mL}^{-1}$) in the medium for 24 h and quantifying the cell migration over time. The concentration of the encapsulated-DNPs-LY releasing an amount of drug equivalent to the control ($2.5 \mu\text{M}$) was calculated by drug release studies. We also investigated the effect of the empty encapsulated-DNPs ($26 \mu\text{g mL}^{-1}$) to assess if any of the components of the formulation affected cell migration. After 24 h, the cells were washed twice with DMEM to remove the drug and NPs dispersed in the media, and fresh 0.5% FBS DMEM was

added to the plate to keep the cells under starvation. The culture medium was replaced every day. The pictures were acquired with an inverted microscope and analysis was performed using Fiji software.

3.22 Hemotoxicity study

The blood compatibility of the modified DNPs-PNA and PNAs was evaluated with a hemolysis assay based on the quantification of released hemoglobin by spectroscopy. Heparin-stabilized fresh human blood was obtained from anonymous donors from the Department of Molecular Medicine and Medical Biotechnology of the University of Naples Federico II and used within 2 h. We added 6 mL of whole blood sample stabilized with EDTA to 10 mL Dulbecco's phosphate-buffered saline (D-PBS) and then centrifuged for 5 min to isolate red blood cells (RBCs). We washed the RBCs with 10 mL of D-PBS and diluted 2 mL of washed RBCs to 40 ml with D-PBS (5% cells). 0.1 mL of diluted RBC suspension was incubated with NPs (25, 50, 100, and 200 $\mu\text{g mL}^{-1}$), PNAs (0.00125, 0.0025, 0.005, 0.01 μmol) or Cys (0.00125, 0.0025, 0.005, 0.01 μmol) D-PBS suspensions, Milli-Q H₂O (positive control), and D-PBS (negative control) for 1, 4, 24, 48 h at room temperature. The samples were centrifuged for 5 min at 13000 rpm and supernatant absorbance was measured at 577 nm by UV-Vis. The hemolytic activity expressed as hemolysis percentage was calculated by the following using equation:

$$\text{Hemolysis}(\%) = \frac{Abs_{\text{sample}} - Abs_{\text{negative control}}}{Abs_{\text{positive control}} - Abs_{\text{negative control}}} \quad (4)$$

3.23 Suspension cultures assay

Spheres were generated and expanded in CSCs media composed of advanced DMEM:F12 (GIBCO) supplemented with 1 \times glutaMAX

(GIBCO), $1 \times$ B-27 (GIBCO), $1 \times$ N2 (GIBCO), 20 ng mL^{-1} bFGF (basic fibroblast growth factor) (Invitrogen) and 50 ng mL^{-1} EGF (epidermal growth factor) (Peprotech). 5×10^2 cells were suspended in 0.5 mL of sphere medium in 24-well ultra-low attachment plates. After 7 days of incubation, the spheres were typically $>75 \mu\text{m}$ large. Cultures were kept no longer than 4 weeks after recovery from frozen stocks (passage 3–4).

CHAPTER IV

Results and discussion

4. Results and discussion

4.1 Delivery and real-time monitoring of galunisertib in colorectal cancer cells by plasmonic-assisted DNPs

This section describes the results reported in the following publication and includes results that have not been published yet. The supporting information (SI) of published data can be accessed here: <https://doi.org/10.1002/sml.202101711>

C. Tramontano[§], S. Managò[§], D. Delle Cave, G. Chianese, G. Zito, L. De Stefano, M. Terracciano, E. Lonardo, A.C. De Luca, I. Rea; SERS quantification of Galunisertib Delivery in Colorectal Cancer Cells by Plasmonic-Assisted Diatomite Nanoparticles, *Small*, 2021, 2101711

4.1.1 DNPs-AuNPs-LY@Gel nanosystem preparation and characterization

The epithelial-to-mesenchymal transition (EMT) is a dynamic multistep process involved in several physiological and pathological conditions, including cancer. In CRC, the EMT is associated with overexpression of metastatic features, alongside invasive and chemo resistant cell phenotype. In contrast, the mesenchymal-to-epithelial transition (MET), which is the reverse program of EMT, is characterized by the upregulation of epithelial adhesive proteins such as E-Cadherin, and downregulation of mesenchymal proteins, such as Snail and Twist. Blocking the EMT or promoting MET are considered powerful therapeutic approaches to treating metastatic CRC cancer. Among the chemotherapeutic drugs used in CRC, galunisertib has been proposed as a powerful small molecule able

to reduce tumor growth and the risk of relapse. However, upon oral administration, galunisertib is predominantly cleared by cytochrome P450 (CYP3A4) in the liver, leading to the formation of various toxic metabolites circulating in the plasma. The major challenge in the treatment of metastatic CRC is to increase the accumulation of the drug in malignant cells and reduce drug dosing regimens. To this aim, here we propose a hybrid nanosystem constituted by DNPs decorated with AuNPs and capped with gelatin (DNPs-AuNPs-LY@Gel) for the sustained delivery of galunisertib in CRC cells and concurrent quantification of drug release at the single-cell level *via* SERS imaging. The real-time quantification of drug in single cells allows for the precise dose response analysis, suggesting the required amount of drug for achieving a significant therapeutic effect.

The DNPs-AuNPs-LY@Gel were prepared following the fabrication procedure reported in Figure 9. Amino-silanized DNPs (reported as “DNPs”) resulted in a mean size of 400 ± 50 nm and a surface ζ -potential of 20 ± 5 mV, due to the positive surface charge of $-\text{NH}_2$ groups on the DNPs’ surface. At this stage, the colloidal suspension of DNPs in deionized H_2O appeared colorless (**Fig. 11**). To decorate silica with AuNPs, the DNPs were dispersed in the HAuCl_4 solution and the AuNPs were synthesized *in-situ*. The $-\text{NH}_2$ groups on the surface of the DNPs allowed for the electrostatic interaction with AuCl_4^- gold precursor ions. The resulting hybrid DNPs-AuNPs had a mean size comparable to that of the bare DNPs within the error (400 ± 50 nm). The ζ -potential decreased to -15 ± 10 mV due to the presence of the $-\text{COOH}$ groups of the dicarboxylic PEG used as a stabilizing agent of the AuNPs. The *in-situ*

synthesis was confirmed by the color change of the DNPs-AuNPs, which turned from transparent to light purple. The porosity structure of DNPs-AuNPs and their surface area of $23.6 \pm 0.1 \text{ m}^2 \text{ g}^{-1}$ allowed for the development of a drug delivery system with efficient galunisertib (LY) loading and release capacity. The small molecule galunisertib was loaded in the DNPs-AuNPs by immersion method in an acidic solution to promote the electrostatic interactions between the protonated isoform of the drug and PEG surrounding the DNPs-AuNPs. The elaborate chemical structure of LY can be protonated on various functional groups according to the multiple isoforms generated under different pH conditions. In this study, the acidic pH of the loading solution promoted the protonation of the quinoline-carboxamide group of the LY, which, in turn, favored the interactions with the negatively charged AuNPs. The interactions between the drug and AuNPs (N –Au type chemisorption) further supported the loading of LY in the DNPs-AuNPs. The nanosystem loaded with LY (DNPs-AuNPs-LY) was finally capped with a layer of crosslinked gelatin to prevent the burst release of the drug in an aqueous solution. The DNPs-AuNPs-LY system was dispersed in a gelatin solution pH 3.5 to preserve the electrostatic interactions between the LY and nanosystem. Then, the gelatin absorbed on the surface of the DNP-AuNPs-LY was crosslinked and the DNPs-AuNPs-LY@Gel still purple in color were characterized. The characterizations of the DNPs-AuNPs-LY@Gel revealed an increment of the mean size to $450 \pm 50 \text{ nm}$ and a surface ζ -potential of $-7 \pm 8 \text{ mV}$, due to the crosslinking of the gelatin layer involving both –COOH and –NH₂ groups and providing the NPs with a neutral surface charge (**Fig. 11 a-b**).

The morphological analysis by TEM (**Fig. 11c**) revealed an irregular shape and a porous morphology of the nanocomplex with a pore size ranging between 15 and 35 nm (Image J). Previous studies demonstrated that the irregular shape of the DNPs did not induce cell toxicity.^[64] The in-situ synthesis promoted the growth of a dense coverage of AuNPs on the surface of the DNPs having a mean size of 25 nm. The DNPs-AuNPs-LY@Gel showed a morphology similar to the DNP before the drug-loading and gelatin capping, revealing that the exposure to the chemical reagents used in the functionalization procedure (*i.e.*, acetone, acidic solutions) did not alter their morphology. The presence of the gelatin layer, visible as a thin and clear ring around the DNPs-AuNPs-LY@Gel in TEM investigations, was further confirmed by UV-Vis analysis. **Figure 11 d** reports the absorbance spectra of bare DNPs, DNPs-AuNPs, and DNPs-AuNPs-LY@Gel suspended in H₂O. The suspension of DNPs did not show absorption peaks in the visible range under investigation (**Fig. 11 d**), whereas the DNPs-AuNPs had an LSPR peak at 576 nm. The presence of LY loaded in the nanocomplex could not be detected through changes in the LSPR of the DNPs-AuNPs-LY suspension, due to the small size of LY (data not shown here). Conversely, the gelatin capping in the DNPs-AuNPs-LY@Gel caused the LSPR to shift by 10 nm due to the increase of the effective refractive index in the NP surroundings. The FTIR analysis (**Fig. 11 e**) showed that DNPs were characterized by two bands at 1100 cm⁻¹ and 800 cm⁻¹ related to the asymmetric and symmetric stretching modes of siloxane (Si–O–Si). The features at 3400 cm⁻¹ and 1640 cm⁻¹ were due to the O–H stretching and O–H bending of H₂O physically absorbed on the silica. The presence of the gelatin in DNPs-AuNPs-

LY@Gel was confirmed by the bands at 1530 cm^{-1} and 1450 cm^{-1} related to N–H bending (amine II), and the features at 2910 cm^{-1} and 2840 cm^{-1} were due to the C–H stretching vibrations.

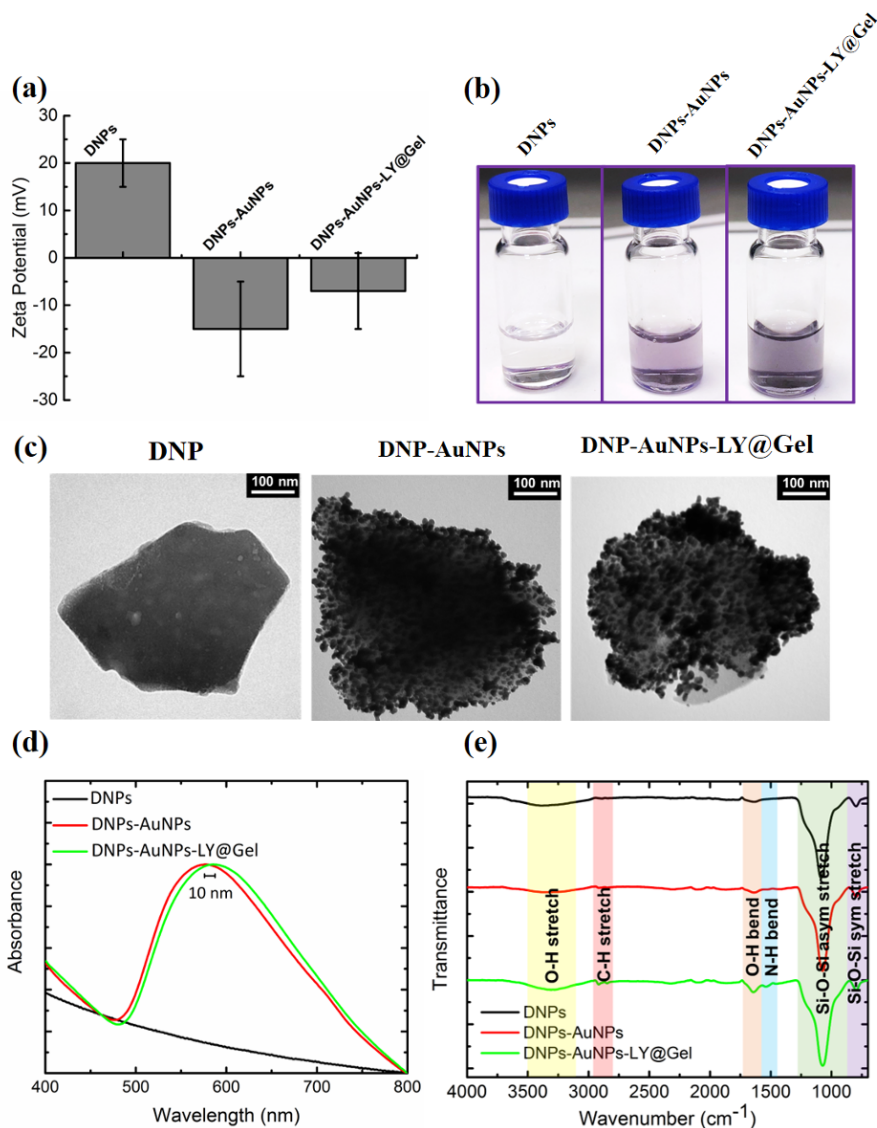


Figure 11. a) ζ -potential of bare DNPs, DNPs-AuNPs, and DNPs-AuNPs-LY@Gel reported as mean ($n=5$) \pm SD. b) Images of vials containing a

suspension of bare DNPs, DNPs-AuNPs, and DNPs-AuNPs-LY@Gel in de-ionized H₂O. c) TEM images of the bare DNP, DNP-AuNPs, and DNP-AuNPs-LY@Gel complex. d) UV-Vis spectra of a suspension of bare DNPs, DNPs-AuNPs, and DNPs-AuNPs-LY@Gel in de-ionized H₂O. e) FTIR spectra of DNPs, DNPs-AuNPs, and DNPs-AuNPs-LY@Gel.

4.1.2 Evaluation of the loading and release capacity of the DNPs-AuNPs-LY@Gel

For the design of a sustained drug release system, gelatin was selected as a capping element due to its advantageous features, including biodegradability, biocompatibility, and pH-responsive behavior. After galunisertib loading and gelatin capping, the DNP-AuNPs-LY@Gel nanosystem was immersed in an acidic solution of PBS and shaken for 48 h. The amount of drug loaded in the nanocomplex (LC) was determined by analyzing the release solution after 48 h by RP-HPLC. The LC of galunisertib in the nanosystem resulted to be $20 \pm 4 \mu\text{g mg}^{-1}$ of the DNPs-AuNPs-LY@Gel. To investigate the release behavior of the nanosystem, we performed *in vitro* release tests under physiological (7.4) and acidic (5.5) pH conditions mimicking the tumor microenvironment. The “Warburg effect” is a well-accepted theory according to which cancer cells produce energy from glucose essentially through the glycolytic pathway. This effect leads to the production of a huge amount of lactate that decreases the tumor microenvironment pH.^[103] The DNPs-AuNPs-LY@Gel exhibited a pH and time-dependent release behavior of galunisertib in the tested conditions. As shown in **Figure 12 a**, the cumulative release of galunisertib increased significantly with decreasing pH values due to the sensitivity of gelatin to the acidic pH. When the

DNPs-AuNPs-LY@Gel was dispersed in PBS solution pH 7.4, the amount of the drug released to the medium was less than 10% of the total LY loaded in the nanocomplex. In the PBS solution 7.4, instead, the gelatin matrix was folded tightly, and the drug was retained in the nanosystem up to 48 h. Since the electrostatic attraction between the gelatin molecules decreases in acidic solutions, when the DNPs-AuNPs-LY@Gel were dispersed in PBS pH 5.5 the relaxation of the gelatin chains promoted the release of galunisertib to the medium in a time-dependent manner (sigmoidal release profile). The drug release from DNPs-AuNPs-LY@Gel started after 10 h and gradually increased due to the extension of the gelatin chains that were disrupted after 48 h of incubation in PBS pH 5.5. When the gelatin matrix was completely dissolved, 100% of the drug was released into the medium. To highlight the advantages of our system, we also carried out *in vitro* release tests of the DNP-AuNPs-LY complex in both acidic and physiological environments (**Fig. 12 b**). The uncapped nanosystem exhibited a typical burst release profile, releasing 100% of the drug within 5 min without any sensitivity to the pH of the release solution. Indeed, the release profiles of the DNP-AuNPs-LY complex in PBS solutions 5.5 and 7.4 were comparable within the errors. Therefore, the gelatin coating in the DNP-AuNPs-LY@Gel delayed the release of galunisertib up to 48 h preventing the uncontrolled burst release typically attributed to porous NP-based systems. Moreover, the choice of gelatin for the surface coating was based on the pathophysiological properties of cancer and offered the opportunity of achieving *stimuli*-responsive drug release at tumor sites.

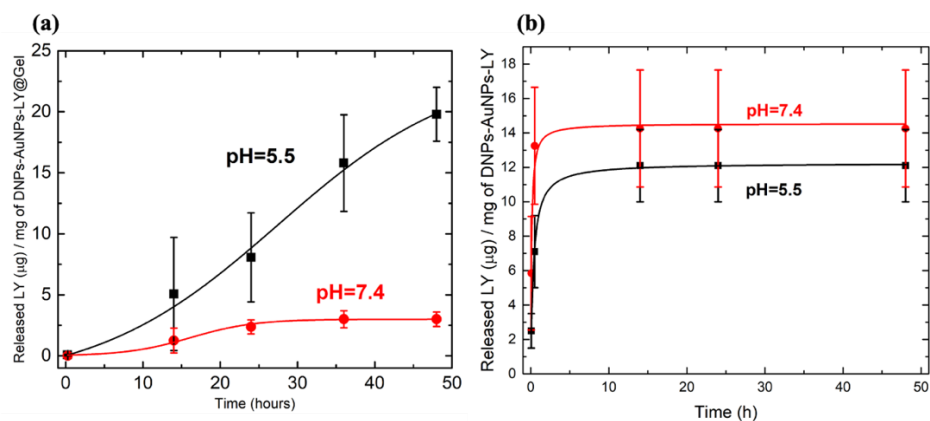


Figure 12. (a) Drug release behavior of the DNP-AuNP-LY@Gel complex in PBS solution at different pH. (b) Drug release behavior of the DNP-AuNP-LY in PBS pH 5.5 and 7.4. The release was expressed as the mass of galunisertib (LY, μg) released from 1 mg of NPs.

4.1.3 SERS monitoring and real-time quantification of the delivered galunisertib in living CRC cells

The major shortcoming of existing nanocarriers is their limited detection sensitivity, which hinders the label-free monitoring and quantification of intracellular drug release. To overcome this limitation, we developed the hybrid system DNP-AuNPs acting as a SERS substrate and nanosensor. The near-field optical amplification of metal nanostructures on the DNP-AuNPs increases their detection performance, allowing for a label-free sensing of biomolecules with excellent specificity and sensitivity. The combination of the drug-loading capacity of DNPs with the strong Raman enhancement of molecules close to AuNPs is an ideal strategy to combine therapeutic purposes with label-free intracellular drug monitoring. Indeed, the hybrid nanosystem can integrate multiple functionalities allowing for bio-imaging and drug delivery simultaneously without using fluorophore

or external markers, thus avoiding fluorescence quenching issues. The incorporation of galunisertib (LY) into the DNPs-AuNPs and enhancement of the LY signal were preliminarily evaluated by studying the Raman and SERS spectra. **Figure 13 a** compares the SERS signals of the complex DNPs-AuNPs-LY@Gel, DNPs-AuNPs@Gel, the substrate DNP-AuNPs alone, and the Raman spectrum of the LY. The drug Raman spectrum exhibited strong bands between 1300–1600 cm^{-1} due to the main molecular vibrational bonds of the pyridine (basically C–H, C–N, C–C stretching and bending modes). The SERS fingerprint of the LY in the DNPs-AuNPs-LY@Gel was markedly similar to its Raman counterpart, whereas the DNPs-AuNPs@Gel and DNP-AuNPs SERS signal did not show any significant spectral feature in the regions between 1300–1650 cm^{-1} . This result confirmed that any of the components of the developed NPs interfered with the SERS signal of the drug itself. The most intense SERS vibration, ascribed to a combined action of ring C–N stretching and bending, was found at 1360 cm^{-1} . The intensity of this band was monitored to quantifying the LY intracellular release from the developed platform. For the SERS experiment, a drop (3 μL) of the DNPs-AuNPs-LY@Gel (500 $\mu\text{g mL}^{-1}$) was deposited on a CaF_2 slide. The LY loaded was $20 \pm 4 \mu\text{g mg}^{-1}$ of DNPs-AuNPs-LY@Gel, which corresponded to $\sim 25 \mu\text{M}$. The SERS spectrum of the complex DNP-AuNPs-LY@Gel revealed an enhancement (SERS Gain, G) of the LY signal of about 4.5×10^5 compared to the Raman signal. G was calculated as the *ratio* between the SERS and Raman signal of the LY bands at 1360 cm^{-1} , normalized to the power (1 mW vs 20 mW), integration time (1 s), and concentration of the drug. G provided quantitative information on the signal gain provided by the

DNPs-AuNPs-LY@Gel compared to pure LY Raman fingerprint at the same experimental parameters. The SERS spectra of LY loaded in the DNP-AuNPs-LY@Gel complex were reproducible and the intensities on a selected nanocomplex could vary up to 18% (the standard deviations for the band at 1360 cm^{-1} , 1500 cm^{-1} , 1545 cm^{-1} , and 1580 cm^{-1} were respectively 4%, 11%, 18% and 8%). The SERS intensity for the band at 1360 cm^{-1} was about $1400\text{ counts s}^{-1}$ at the considered experimental parameters. A standard deviation of about 10% was registered for signals acquired on different clusters of the DNPs-AuNPs-LY@Gel, showing a good inter-sample reproducibility (see SI of the publication).^[29]

Before investigating the release properties of the DNPs-AuNPs-LY@Gel, we evaluated its internalization in the human CRC cell line LS-174T by Raman imaging (**Fig. 13 b**). To this aim, LS-174T cells were incubated with a dispersion of $50\text{ }\mu\text{g mL}^{-1}$ of DNPs-AuNPs-LY@Gel for 18 h and 24 h. Different colors are associated with the loadings/spectra (see SI of the publication) used to reconstruct the Raman map and are linked with a specific cell location (*i.e.*, nucleus, cytoplasm) or nanocomplex. By using the MCR approach, it was possible to reconstruct a false color Raman map of the cell showing that the NPs were internalized and localized in a few clusters distributed throughout the cell cytoplasm within 18 h of incubation.^[60] Then, we investigated the LY release from the DNPs-AuNPs-LY@Gel in PBS pH 5.5 and 7.4 by SERS analysis (**Fig. 13 c**). The DNPs-AuNPs-LY@Gel were deposited on a CaF_2 slide with a distribution of 250 ng mm^{-2} . The total mass of DNPs-AuNPs-LY@Gel was $1.5\text{ }\mu\text{g}$ carrying 30 ng of LY; the amount of LY loaded in a single DNP-AuNPs-LY@Gel was 0.25 fg (section 3.13). In PBS pH 7.4, a very small amount

of LY (~4%) was released by the DNPs-AuNPs-LY@Gel within 24 h. A slow release was observed after 30 h and about 60% of LY was delivered from DNPs-AuNPs-LY@Gel after 48h. At pH 5.5, mimicking the cancer cell microenvironment, the release of LY from the NPs became faster and a great amount of LY (~50 %) was released after 24 h, reaching 90% of the released drug after 48h. These results confirmed that the gelatin coating provided the nanoplatform with a pH-responsive behavior and triggered the drug release in acidic conditions, as observed also by HPLC analysis. The amount of LY released from the nanoplatform was quantified by SERS according to the LC calculated by HPLC (section 4.1.2). According to **Figure 13 c**, 50% of LY was released from 1.5 μg of DNPs-AuNPs-LY@Gel after 24 h in the acidic microenvironment, corresponding to 0.125 fg per nanocomplex unit (15 ng of LY). These observations confirmed that the loaded anticancer drug was efficiently released in acidic conditions and that the release could be quantified per single nanocomplex unit due to the high sensitivity provided by the SERS technique.

The time-dependent release of LY was further studied in living LS-174T cells to monitor the release behavior of the developed NPs in a cancer microenvironment at various incubation times (0, 2, 18, 24, 42 and 48 h). A dispersion of DNPs-AuNPs-LY@Gel was incubated in 1.5 mL of cell medium at a final concentration of 50 $\mu\text{g mL}^{-1}$, corresponding to a total mass of DNPs-AuNPs-LY@Gel of 75 μg and a total mass of LY loaded of 1.5 μg . The mass of LY for single DNPs-AuNPs-LY@Gel was 0.25 fg. After 2h, the SERS signal was collected only from the non-internalized DNPs-AuNPs-LY@Gel, and, therefore, the LY signal intensity in the cells was comparable to the control experiments (without cells). At this point,

the nanoplatform was not internalized and it was not possible to trace the SERS signal of LY in cells. Conversely, after 18 h, the nanoplatform penetrated cancer cells and the LY SERS signal was detected inside cells, indicating a successful internalization. After 18 h the amount of LY released in LS-174T cells was ~30% of the total encapsulated drug, corresponding to 450 ng of LY (0.075 fg for the DNP unit). The released LY was ~50% of the total encapsulated drug (750 ng overall, 0.125 fg for DNP unit) after 24 h. A smooth LY release was observed after 30 h and 65% of LY was released (975 ng overall, 0.16 fg for DNP unit) after 48h. Interestingly, an efficient SERS intracellular tracing and imaging of LY in living CRC was demonstrated up to 48 h and quantified to provide an LY sensing resolution down to 7.5×10^{-18} g. For comparison, the LY release from the DNP-AuNPs-LY complex (without the gelatin coating) was investigated in PBS pH 7.4 and pH 5.5 and in living CRC within 48 h by SERS analysis. A burst LY release was observed after 60 seconds regardless of the pH (see **SI of the publication**).^[29] The LY SERS signal completely disappeared after 10 min, as observed *in vitro* release by HPLC (section 4.1.2). These results further demonstrated that the nanosystem designed without the gelatin coating was not suitable for sustained drug delivery inside cancer cells.

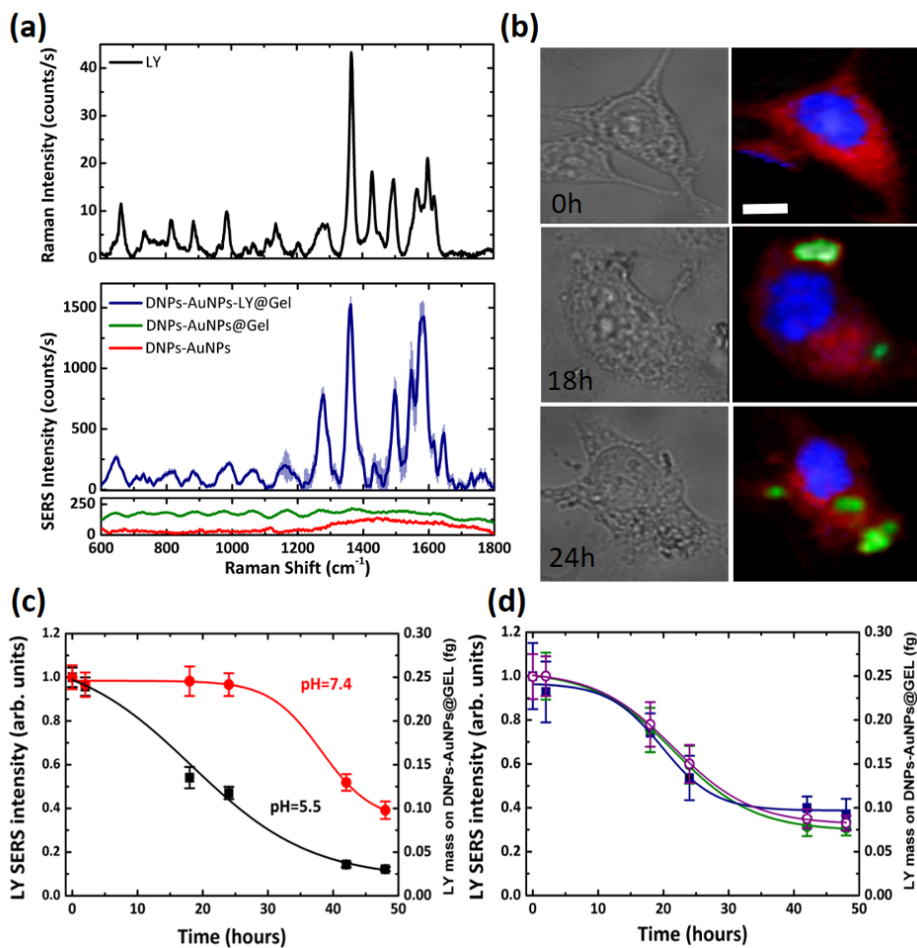


Figure 13. (a) Raman spectrum of galunisertib (LY, black line) and SERS spectrum of LY in the complex DNP-AuNPs-LY@Gel (blue line), background signals from the DNP-AuNPs@Gel (red line), and the DNP-AuNPs alone (green line). All the SERS and Raman spectra were rescaled to a common laser power of 1 mW so that the intensities could be directly compared. Spectra are offset for clarity. (b) Optical image and Raman mapping images showing the internalization of DNP-AuNPs-LY@Gel into CRC cells after 0, 18, and 24 h of incubation. The scale bar is 10 μm

(c) Time-dependent LY SERS intensity from the DNPs-AuNPs-LY@Gel in PBS pH 7.4 and pH 5.5. (d) Time-dependent LY SERS signal from the DNP-AuNPs-LY@Gel complex in living CRC cells.

4.1.4 Evaluation of MET induced by DNPs-AuNPs-LY@Gel in CRC cells

After assessing the drug release properties of the developed nanoplatform, we evaluated whether the controlled delivery of LY from the DNPs-AuNPs-LY@Gel could increase the therapeutic efficacy of the drug, reducing tumor cell invasiveness and metastases. For these studies, the LS-174T cell line was chosen due to its metastatic potential and mesenchymal phenotype. The LS-174T cells were also selected because they trigger an intact TGF- β signaling useful to test the inhibitory potential of LY delivered by our complex.^[77]

The cellular uptake of DNPs-AuNPs-LY@Gel labeled with Alexa Fluor[®]-488 (DNPs-AuNPs*-LY@Gel) was investigated by confocal microscopy (**Fig. 14**). To evaluate whether the gelatin layer affected the cellular uptake of the DNPs, the internalization of the labeled DNPs-AuNPs-LY (DNPs-AuNPs*-LY) was also investigated. To this aim, 50 $\mu\text{g mL}^{-1}$ of the DNPs-AuNPs*-LY@Gel or DNPs-AuNPs*-LY were incubated with the LS-174T cell line for 24 h. Then, the cells were washed, and cell nuclei and membranes were stained with DAPI and WGA-Alexa Fluor[™] 555, respectively. Untreated cells (**Fig. 14**) and cells treated with free dye are also shown as controls. The images revealed that the presence of the gelatin layer did not alter the cellular uptake of the DNPs since the DNPs-AuNPs*-LY@Gel and DNPs-AuNPs*-LY exhibited a comparable internalization. The morphological analysis performed on the cells

reported in **Figure 14** allowed us for the evaluation of the MET process. The results, expressed in terms of elongated (mesenchymal) and rounded (epithelial) cells showed that only the DNP-AuNP*-LY@Gel were able to promote the reversion of the cell phenotype (**Fig. 16 e-f**). Moreover, since the internalization of DNP-AuNP-LY and DNP-AuNP-LY@Gel was comparable, we hypothesized that DNP-AuNP*-LY had a negligible effect on the cell phenotype due to the complete loss of the drug, as shown by SERS and HPLC investigations.

The biocompatibility of the DNP-AuNP-LY@Gel suspension was investigated by exposing the LS-174T cell line to the nanosystem at different concentrations ($12.5100 \mu\text{g mL}^{-1}$) for 24 and 48 h and monitoring the cell growth. The results reported in **Fig. 15 a** demonstrated that the multifunctional platform did not induce cell toxicity up to 48 h of incubation. A concentration of DNP-AuNP-LY@Gel $50 \mu\text{g mL}^{-1}$ carrying $2.5 \mu\text{M}$ of the drug was selected for cell treatments.

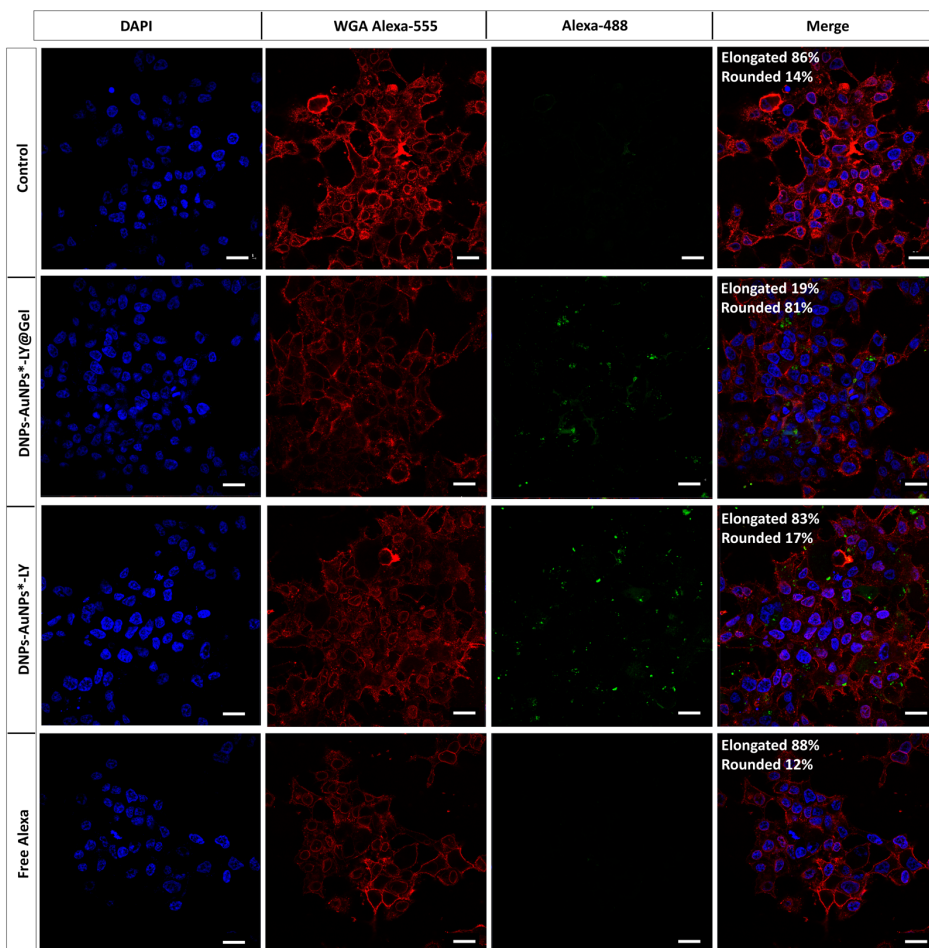


Figure 14. Confocal fluorescence images of LS-174T cells incubated with labeled DNPs-AuNPs*-LY@Gel or DNPs-AuNPs*-LY for 24 h. As a control, untreated cells (first line) and cells treated with the free dye Alexa Fluor[®]-488 20 $\mu\text{g mL}^{-1}$ (last line) were also reported. Cell nuclei and membranes were stained with DAPI and WGA-Alexa Fluor[®]-555, respectively; the DNPs were labeled with Alexa Fluor[®]-488 *via* carbodiimide chemistry. The scale bar is 20 μm .

The cell growth of LS-174T was also investigated in presence of 2.5 μM of LY, 50 $\mu\text{g mL}^{-1}$ of DNPs-AuNPs@Gel or DNPs-AuNPs, and 50 $\mu\text{g mL}^{-1}$ of DNPs-AuNPs-LY@Gel or DNPs-AuNPs-LY (both containing 2.5 μM of LY, according to the HPLC quantitative analysis) (**Fig. 15 b**; **Fig. 16 a**). We did not observe significant changes in the LS-174T cell growth after 48 h of treatment with all the developed NPs. Analogue studies were performed using the highly invasive CRC SW620 cells, which display a phenotype and genetic background similar to LS-174T cells. In this case, we observed a slight increase in cell growth in the presence of DNPs-AuNPs@Gel, DNPs-AuNPs and DNPs-AuNPs-LY suspensions (**Fig. 15 c**; **Fig. 16 b**). Overall, we observed that none of the components of the developed nanoplatform was toxic to the cells.

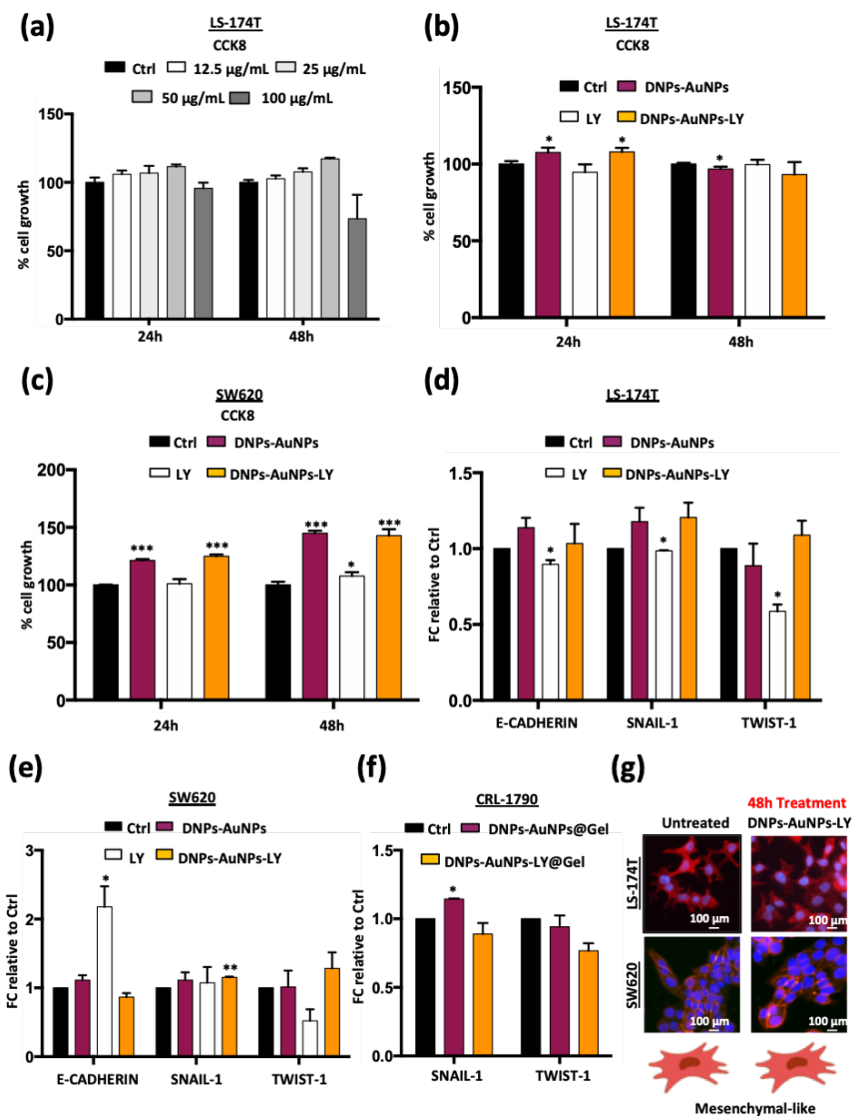


Figure 15. (a) Cell viability of LS-174T cells grew for 24 and 48 h with DNP-AuNPs-LY@Gel at different concentrations. Cell viability was evaluated using CCK8, and absorbance was measured at 450 nm. $n \geq 6$. (b) Cell viability of LS-174T cells grew for 24 and 48 h with 2.5 μM LY, 50 $\mu\text{g mL}^{-1}$ of DNP-AuNPs and 50 $\mu\text{g mL}^{-1}$ of DNP-AuNPs-LY. Cell

viability was evaluated using CCK8, and absorbance was measured at 450 nm. * $p \leq 0.05$, $n \geq 6$. **(c)** Cell viability of SW620 cells grew for 24 and 48 h with 2.5 μM LY, 50 $\mu\text{g mL}^{-1}$ of DNPs-AuNPs and DNPs-AuNPs-LY. **(d)** qPCR analysis of EMT genes in LS-174T cells grew for 24 h in presence of 2.5 μM LY, 50 $\mu\text{g mL}^{-1}$ of DNPs-AuNPs and DNPs-AuNPs-LY. Data were normalized to *GAPDH* expression and presented as Fold Change (FC) in gene expression relative to Ctrl. * $p \leq 0.05$. $n \leq 6$. **(e)** qPCR analysis of EMT genes in SW620 cells grew for 24 h with the indicated treatments. **(f)** qPCR analysis of EMT genes in human normal colonic cells (CRL-1790) grew for 24 h with 2.5 μM LY, 50 $\mu\text{g mL}^{-1}$ of DNPs-AuNPs and DNPs-AuNPs-LY. **(g)** Representative images of LS-174T and SW620 cells untreated or treated with DNPs-AuNPs-LY for 48 h.

It has been shown that MET may be induced by blocking the activity of specific factors and signaling pathways that trigger EMT, including the TGF- β -mediated phosphorylation of Smad proteins. Therefore, we investigated whether the DNPs-AuNPs-LY@Gel could reverse the EMT by blocking the TGF- β 1 receptor. The anti-metastatic effect of the developed hybrid multifunctional complex was assessed by investigating E-Cadherin, Snail-1, and Twist-1 expression levels in LS-174T and SW620 cells using qPCR analysis. MET is characterized by loss of mesenchymal markers (*i.e.*, Snail-1 and Twist-1) and enhancement of epithelial markers (*i.e.*, E-Cadherin). During the EMT, the cells lose their epithelial characteristics, like cell polarity and cell-cell contacts, and gain mesenchymal traits such as increased motility. The transient nature of the EMT events allows mesenchymal cells for reverting to an epithelial shape when signals driving the EMT decrease. In both cell lines, the DNP-

AuNPs-LY@Gel complex significantly increased the expression of E-Cadherin and suppressed the expression of Snail-1 and Twist-1 genes (**Fig. 16 c-d**). Of note, the modulation of the expression levels of E-Cadherin, Snail-1, and Twist-1 genes was much stronger upon treatment with DNPs-AuNPs-LY@Gel than free LY at equal concentrations. The encapsulation of LY in the hybrid nanoplatform enhanced the drug effect, thus requiring a lower dose to induce MET in metastatic cells. Reduced doses can lower the likelihood of adverse side effects and the risks of toxic metabolites circulating in the plasma. Any gene modulation was not observed after treatment with DNPs-AuNPs@Gel, DNPs-AuNPs, and DNPs-AuNPs-LY suspensions (**Fig. 15 d-e; Fig 16 c-d**), confirming that the DNPs-AuNPs-LY had no therapeutic effect due to the loss of drug. These results confirmed that the modulation of metastatic genes was consistent only upon cell exposure to the DNPs-AuNPs-LY@Gel.

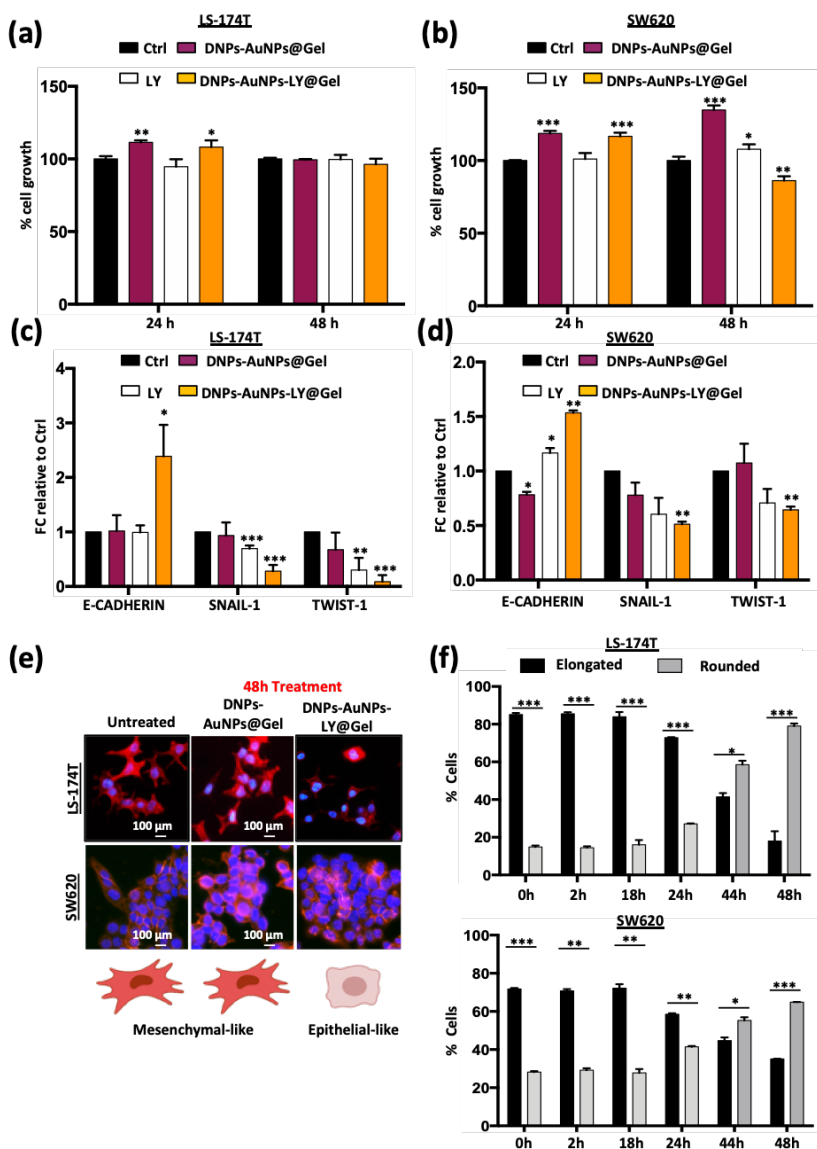


Figure 16. (a) Cell viability of LS-174T cells grew for 24 and 48 h with 2.5 μM LY, 50 μg mL⁻¹ DNPs-AuNPs@Gel and DNPs-AuNPs-LY@Gel (containing 2.5 μM of LY). Cell viability was evaluated using CCK8, and absorbance was measured at 450 nm. *p<0.05, **p<0.005, n≥6. (b) Cell viability of SW620 cells grew for 24 and 48 h in the presence or absence

of 2.5 μM LY, 50 $\mu\text{g mL}^{-1}$ of DNPs-AuNPs@Gel, and DNPs-AuNPs-LY@Gel. (c) qPCR analysis of EMT genes in LS-174T cells grew for 24 h in presence of 2.5 μM LY, 50 $\mu\text{g mL}^{-1}$ of DNPs-AuNPs@Gel and DNPs-AuNPs-LY@Gel (containing 2.5 μM of LY). * $p < 0.05$, ** $p < 0.005$, *** $p < 0.0005$, $n \geq 6$. (d) qPCR analysis of EMT genes in SW620 cells incubated for 24 h with 2.5 μM LY, 50 $\mu\text{g mL}^{-1}$ of DNPs-AuNPs@Gel and DNPs-AuNPs-LY@Gel (containing 2.5 μM of LY). Data were normalized to GAPDH expression and presented as Fold Change (FC) in gene expression relative to control (Ctrl). * $p < 0.05$, ** $p < 0.005$. $n \geq 6$. (e) Representative images of DNPs-AuNPs-LY@Gel-mediated MET in LS-174T and SW620 cells. (f) Percentage of cells with elongated (mesenchymal) or rounded (epithelial) shape treated with DNPs-AuNPs-LY@Gel (50 $\mu\text{g mL}^{-1}$) at the indicated times. The number of counted cells n is ≥ 500 . * $p \leq 0.05$, *** $p \leq 0.0005$. $n \leq 5$.

The DNPs-AuNPs-LY complex realized without the gelatin layer did not induce any variation because it was not able to retain LY as demonstrated by the HLPC and SERS analysis. We also studied the effects of the LY delivery on normal human colon epithelial cells (CRL-1790) upon exposure to 50 $\mu\text{g mL}^{-1}$ of the DNPs-AuNPs-LY@Gel or DNP-AuNPs@Gel (**Fig. 15 f**). The treatment with DNP-AuNPs-LY@Gel did not induce effects on the normal cell line since the expression levels of SNAIL-1 and TWIST-1 genes were unvaried (**Fig. 15 f**). However, since the healthy cells are generally responsive to TGF- β signaling, we cannot exclude that some other genes could be affected by the treatment with the DNP-AuNPs-LY@Gel complex.

The E-CADHERIN plays an essential role in maintaining epithelial integrity and the upregulation induced by the developed NPs was also accompanied by morphological changes in LS-174T and SW620 cells (**Fig. 16 e**). Specifically, cells treated with a suspension of $50 \mu\text{g mL}^{-1}$ of DNPs-AuNPs-LY@Gel showed an evident morphological shift from elongated and spindle-shape (mesenchymal) to rounded (epithelial) phenotype compared to untreated cells or treated with DNPs-AuNPs@Gel or DNPs-AuNPs@Gel (**Fig. 15 g**). The morphological changes were quantified by recording the phenotype shapes over time (**Fig. 16 f**). The transition from elongated to rounded phenotype was already appreciable after 24 h of treatment with the DNPs-AuNPs-LY@Gel and became stronger after 44 h, as shown by the 60% of the cells losing the mesenchymal phenotype. The complete phenotype reversion occurred after 48 h of incubation in both cell lines, where 80% of cells acquired epithelial morphology (**Fig. 16 f**). The cell evolution to a rounded phenotype followed the same profile as the intracellular drug release evaluated by SERS analysis (section 4.1.3). The observed morphological changes confirmed that the metastatic process could be slackened by treating the CRC cells with the developed nanoplatform, which turned out to be more efficient than the free drug.

...

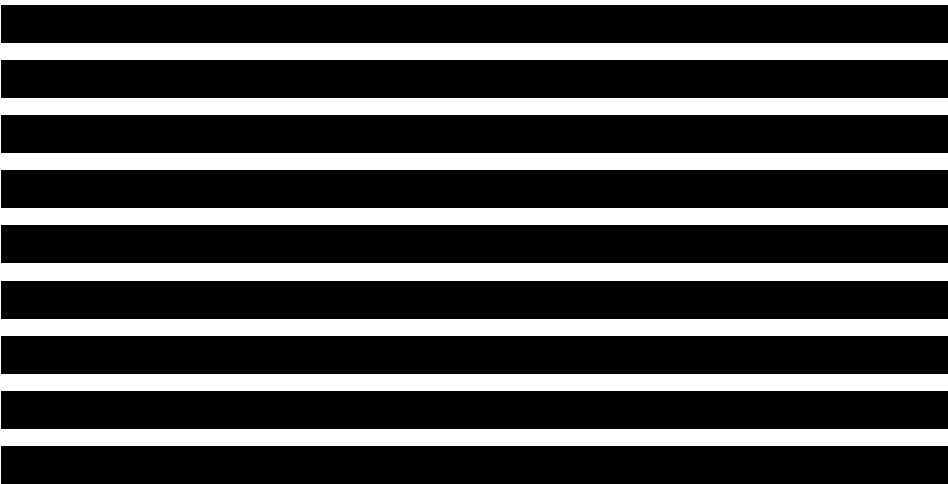
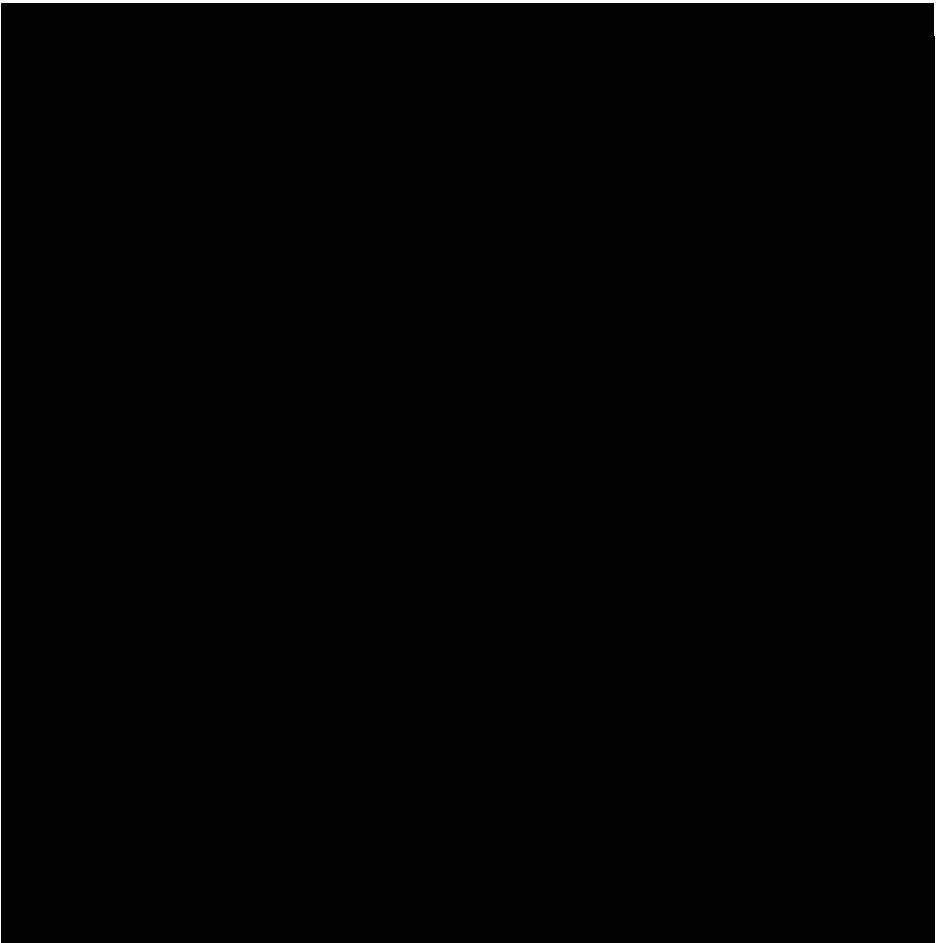
The following paragraphs report the development of DNPs-AuNPs-LY@Gel modified with the anti-L1-CAM antibody and targeting metastatic CRC cells overexpressing the L1-CAM. To assess the efficacy of the developed active-targeted nanoformulation, additional *in vitro* tests on monolayer and 3D cells were performed and reported herein. The

efficacy of the developed nanosystem is under investigation *in vivo* (data not shown here). The results reported in sections 4.1.5 and 4.1.6 are unpublished.

[REDACTED]

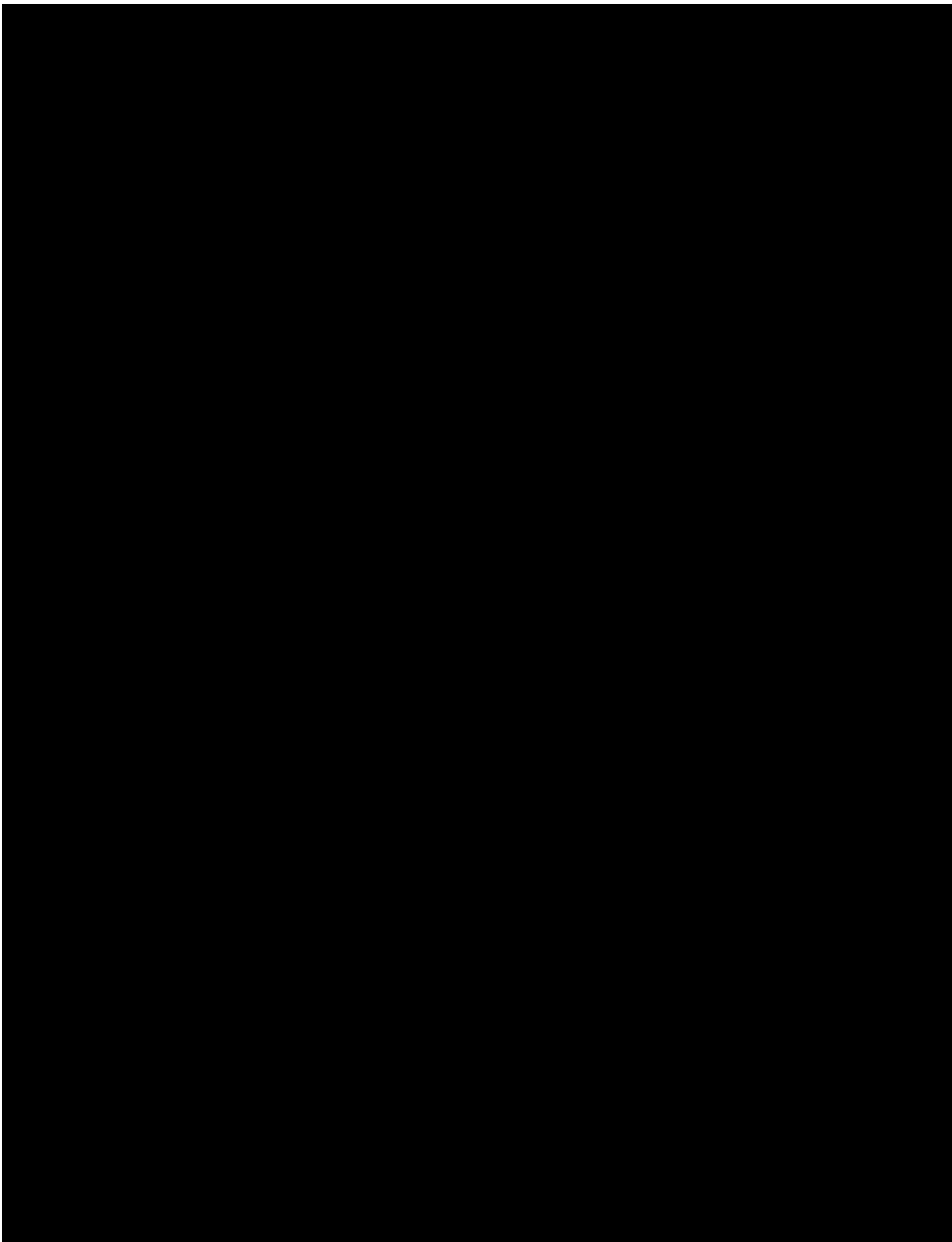
[REDACTED]

[REDACTED]



[REDACTED]

[REDACTED]



[Redacted line of text]

[REDACTED]

[REDACTED]

[REDACTED]

4.2 Enhancement of the galunisertib loading capacity of gelatin-capped plasmonic DNPs for drug delivery applications

This section describes the results reported in the following publication. The supporting information (SI) can be accessed here: <https://doi.org/10.1002/sml.202101711>

C. Tramontano, B. Miranda, G. Chianese, L. De Stefano, C. Forestiere, M. Pirozzi, I. Rea; Design of Gelatin-Capped Plasmonic Diatomite Nanoparticles with Enhanced Galunisertib Loading Capacity for Drug Delivery Applications, *Int. J. Mol. Sci.*, 2021, 22, 10755.

4.2.1 Fabrication and characterization of plasmonic DNPs with gelatin shells of varying thickness

The loading capacity (LC) is a crucial feature of nanocarriers determining the number of NPs that are required to releasing a clinically relevant dose of the drug and achieving the desired therapeutic outcome. The most common way to improve the LC of nanocarriers is to increase the porosity or pore size of the NPs. However, porosity is an intrinsic feature that cannot be tuned in bioderived porous materials, such as the DNPs. Alternatively, the drug LC can be increased by encapsulating the drug-loaded DNPs in gelatin shells, whose thickness can be tuned according to the polymer concentration and desired amount of encapsulated drug.

The development of a hybrid nanosystem with gelatin shells of increasing thicknesses was performed according to the functionalization scheme reported in **Figure 19 a**. The growth of AuNPs on the surface of DNPs

(AuDNPs) was performed through a liquid phase approach in which the DNPs were dispersed in HAuCl_4 solution and the reduction of gold salts in AuNPs was performed *in-situ*. As previously described, DNPs were modified with 10% v/v APTES to provide the surface with positive groups $-\text{NH}_3^+$ (DNPs-APT) and promote the electrostatic interactions with the gold ions. The electrostatic attraction between the negative gold precursors and positive charged DNPs (DNP-APT) granted the in-situ accumulation of AuNPs on the DNPs-APT. The DNPs-APT were dispersed in 0.1 M HAuCl_4 solution and stirred for 10 min with 0.025% aqueous gelatin as a stabilizer. In this protocol, we stabilized the AuNPs with gelatin (gel-AuNPs) rather than diacid PEG used in section 4.1. Gelatin is a natural biocompatible material that provided AuNPs with long-term stability and prevented AuNPs aggregation on the biosilica surface. Generally, gel-AuNPs are obtained by reduction gold salts by thermal heating.^[139] Here, for the first time, the reduction of gelatin-stabilized gold ions was performed using NaBH_4 , which allowed for a better control of NPs' size due to the dropwise addition of the reducing agent. The formation of the AuDNPs was immediately appreciated by a colorimetric change of the dispersion, which turned from light yellow to deep red. The AuDNPs were washed to remove excess reagents, resuspended in PBS solution and then dispersed in EDC/NHS mixture to crosslink gelatin by a peptide bond between the $-\text{NH}_2$ and $-\text{COOH}$. Since the electrostatic interactions between gel-AuNPs and DNPs-APT were not stable under harsh stirring and pH conditions, we crosslinked the gelatin stabilizing the AuNPs to anchor them to the surface of DNPs-APT. This process allowed for further functionalization of the complex and prevented the loss of AuNPs from the

DNPs-APT. The major difference in the preparation of the AuDNPs described herein and in section 4.1 is the use of gelatin as a stabilizer, which provided the plasmonic AuDNPs with drug release monitoring functionalities. To stress the difference between the DNPs-AuNPs in section 4.1 and the formulation described here, the hybrid complex composed of DNPs and gel-AuNPs is referred to as “AuDNPs”. Then, galunisertib (LY) was loaded in the AuDNPs and the complex (AuDNPs-LY) was mixed with concentrated gelatin solutions to create a shell. Gelatin was both the stabilizing agent of AuNPs and polymer coating material. The AuDNPs-LY were dispersed in gelatin solutions of increasing concentration (0.125 %, 0.25%, 0.50%, 0.75%, 1.5% w/v) and crosslinked *via* EDC/NHS that favored the formation of shells of different thickness. The final plasmonic system consisted of DNPs covered by gel-AuNPs, loaded with LY, and further capped by gelatin to prevent burst release (**Fig. 19 a**). To assess the presence of the outer gelatin shell in the AuDNPs-LY@Gel, TEM, DLS, and ζ -Potential studies were performed (**Fig. 19 b-d**). The irregular surface of DNPs was decorated by a carpet of AuNPs with a mean radius r of ~ 3 nm (**Fig. 19 b I- c**). The presence of the gelatin shell covering the final AuDNPs-LY@Gel _{x} (where x is the concentration of gelatin) was confirmed by the surface becoming darker and smoother upon an increment of the gelatin concentration.^[140] Moreover, as evident from Figure 19 b II-III, the gelatin shells obscured the AuNPs, which were no longer visible on the nanosystem after gelatin shell formation. On the contrary, gelatin used as stabilizer in the AuNPs synthesis did not cover the surface of AuDNPs (**Fig. 19 b I**). According to DLS and ζ - potential investigations (**Fig. 19 d**), the DNPs-APT had a mean

diameter of 290 ± 30 nm and a surface charge of 28 ± 6 mV due to the presence of protonated $-\text{NH}_3^+$. Increasing concentrations in the gelatin shell caused an increment in the particle size mainly ascribed to NPs' aggregation due to the sticky nature of gelatin. For the sample AuDNPs-LY@Gel_{0.125%} and AuDNPs-LY@Gel_{0.25%}, we observed a size increment of about 30 nm. For the AuDNPs-LY@Gel_{0.5%}, instead, the size increased from 290 ± 30 to 420 ± 60 nm.

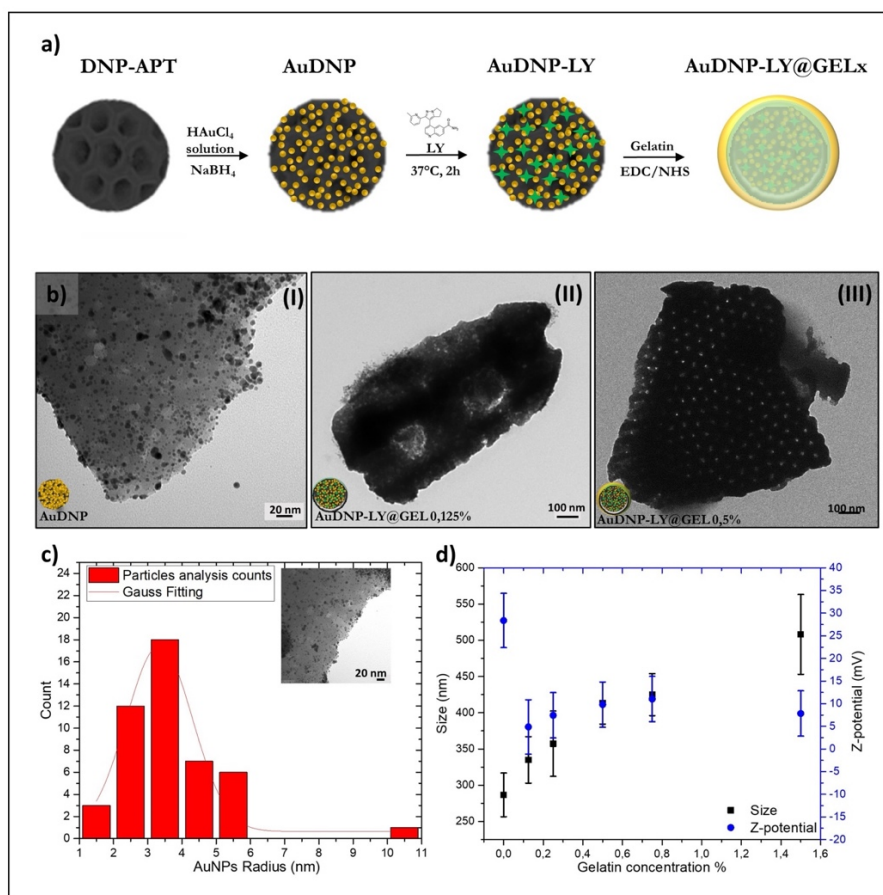


Figure 19. (a) Schematic representation of the functionalization procedure. The growth of AuNPs on the surface of the DNPs was achieved by dispersing amino-modified DNPs in the HAuCl_4 solution, adding gelatin as the stabilizer and NaBH_4 as reducing agent. Then, galunisertib (LY) was loaded into the NPs (AuDNPs-LY) and gelatin shells of varying concentrations and thicknesses (x) were performed by polymer crosslinking (AuDNPs-LY@Gel $_x$). (b) TEM investigations of the AuDNP (I), AuDNP-LY@Gel $_{0,125\%}$ (II) and AuDNP-LY@Gel $_{0,5\%}$. (c). Particle size analysis of the gel-AuNPs decorating the surface of the DNP fitted by a Gauss curve. (d) Changes in the size (black) and surface charge (blue) of the samples AuDNPs-LY@Gel $_x$ varying the gelatin concentration in the outer shell.

We observed that the size of the AuDNPs-LY@Gel $_x$ changed proportionally to the amount of gelatin in the external shells, with a larger size detected in the sample with the highest concentration of gelatin (AuDNPs-LY@Gel $_{1,5\%}$). The increment of the size observed after the formation of the gelatin shell was also influenced by the neutral surface charge exhibited by the AuDNPs-LY@Gel $_x$. Type B gelatin has an isoelectric point (IEP) between 4.8-5.4, therefore it was expected for AuDNPs-LY@Gel $_x$ samples to have a negative surface charge in an aqueous solution pH 6.5 - 7.0 ($\text{pH} > \text{IEP}$). However, a shift of the IEP of the gelatin toward 6-7 can be observed as a consequence of the crosslinking between $-\text{COOH}$ and $-\text{NH}_2$ in the polymer backbone.^[141] Due to this shift, the surface charge of gelatin should be neutral at the IEP or slightly positive. As expected, the ζ -potential of the AuDNPs-LY@Gel $_x$ (0.125 %, 0.25%, 0.5%, 1% and 1.5%) decreased from 28 ± 6 mV (DNPs-APT) to 7

± 5 mV in H₂O, confirming the successful cross-linking of the gelatin shell. Since the gel-AuNPs composing the system were firmly stabilized on the DNPs' surface, the particle aggregation arising from a neutral surface charge did not affect the stability and plasmonic response of the gel-AuNPs.

4.2.2 Correlation of gelatin concentration and shell thickness of the AuDNPs-LY@Gel_x based on a validated optical model

To correlate the concentration of gelatin in the shell to the mean polymer thickness, we studied and optimized a theoretical model based on the optical response (λ_{\max} and λ_2) of gel-AuNPs on the DNPs, which was described in detail in the published paper.^[61] The correlation between gelatin concentrations used for the shell formation and effective shell thicknesses (t) can be a crucial parameter for the design of a nanocarrier. By decorating the DNPs with gel-AuNPs, our system allowed for the monitoring of the shell formation, degradation, and consequent drug release through changes in the LSPR peak of the developed hybrid NPs. First, we simulated the LSPR response of the AuDNPs-LY@Gel_x having shells of increasing thicknesses (t), which modified the effective refractive index of the medium and caused a plasmonic redshift of AuDNPs-LY@Gel_x compared to AuDNPs-LY. Crosslinked gelatin possesses a refractive index higher than H₂O and silica, thus causing a redshift of the plasmon resonance λ_{\max} of the AuDNPs-LY@Gel_x. We performed the simulation for average thicknesses of gelatin shells between 0 – 20 nm and the results are reported in **Figure 20 a**. The experimental LSPR shifts of the AuDNPs-LY@Gel_x systems developed using different concentrations of gelatin in the outer shell are reported in **Figure 20 b**. Since the gel-

AuNPs had a mean size of 3 nm, both the inflection points λ_2 and λ_{\max} were studied for theoretical and experimental absorption spectra, thus enhancing the plasmonic response sensitivity. To do this, we calculated the first derivatives of the spectra and considered the minima of these curves as λ_2 (**Figure 20 c-d**). Although there was another inflection point (λ_1) corresponding to the maxima of the first derivatives, it has been already demonstrated that the highest sensitivity for refractive index sensing can be obtained by considering the λ_2 values.^[142] Moreover, the first inflection points laid near the regions in which the theoretical prediction was not as accurate as in the other regions, due to the absorptions of galunisertib and gelatin in those regions (see SI of the paper).^[61]

From the theoretical analysis, λ_2 underwent a redshift as a function of the gelatin thickness. The λ_2 exhibited a red shift from 600 to 616 nm following a saturation curve with a linear range from 0 to ~11 nm of gelatin thickness and achieving saturation at ~18 nm (**Fig. 20 e**, white squares). This saturation behavior can be explained by the rapidly decaying field enhancement of gel-AuNPs, whose plasmonic effect was localized to the NP's surroundings. This means that the inflection points of the absorption spectra of the AuDNPs-LY@Gel_x were not affected by gelatin having a thickness > 20 nm. The experimental evaluation of λ_2 was performed by measuring the absorption spectra of the AuDNPs-LY@Gel_x obtained using different gelatin concentrations for the formation of the outer shell: 0%, 0.125%, 0.25%, 0.5%, 0.75% and 1.50%. A redshift of the inflection points was observed for the different gelatin concentrations (**Fig. 20 c-d**), in agreement with the theoretical model (**Fig. 20 a**). The theoretical and experimental results reported in **Figure 20 c, e** enabled drawing a

correlation between gelatin concentrations and thicknesses on the hybrid AuDNPs-LY@Gel_x nanocarrier. The relationship between gelatin concentration (c_{gel}) and thickness (t) exhibited a saturation behavior due to the electromagnetic field decay in the surroundings of gel-AuNPs, which could be described by the following Michaelis-Menten equation in the investigated thickness range (**Fig. 20 f**):

$$t = t_{max} \frac{[c_{gel}]}{k_t + [c_{gel}]} \quad (5)$$

where t_{max} was the maximum gelatin thickness (18 nm) at which a redshift of the inflection point λ_2 was appreciated. $K_t = 0.63$ % was the gelatin concentration at which the shell thickness on the AuDNPs-LY@Gel corresponded to half of the t_{max} (9 nm).

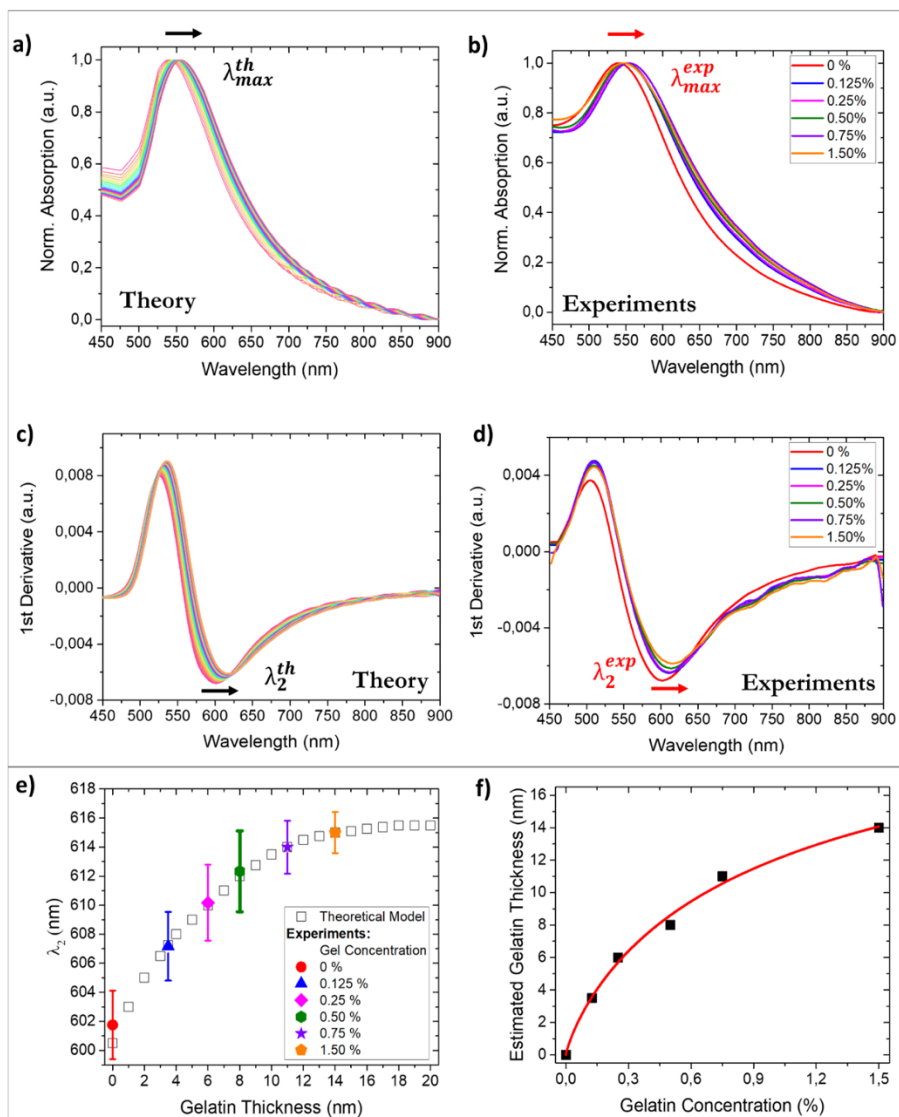


Figure 20. Correlation between gelatin concentration and gelatin thickness: (a, c) Theoretical absorption spectra and first derivatives of AuDNPs-LY@Gel with increasing thicknesses of the gelatin shells. The black arrows indicate the redshifts of λ_{max}^{th} (a) and λ_2^{th} (c) associated with the increase in the gelatin coating thickness, respectively. (B, d)

Experimental absorption spectra and first derivatives of AuDNPs-LY@Gel with increasing gelatin concentrations. The red arrows indicate the redshifts of experimental (exp) λ_{\max} and (b) λ_2 associated with the increasing gelatin concentrations used to make the shell. (e) Comparison between theoretical (th) λ_2 (theoretical model) as a function of the gelatin coating thickness and experimental λ_2 (experimental data). (g) Correlation between the gelatin concentration and the estimated thickness of the gelatin coating. The red line is a fitting of the scatter plot.

The formation of gelatin shells on the AuDNPs-LY@Gel_x followed the typical a substrate-enzyme kinetic, in which the gelatin concentration was the substrate, while the electromagnetic field decay of gel-AuNPs was the limiting reagent (enzyme). While saturation in a typical enzyme-substrate reaction is achieved when the enzyme is exhausted, in our case saturation was achieved when the electromagnetic field enhancement of gel-AuNPs decayed. In the linear region (**Fig. 20 e-f**), the shell thickness was correlated to the gelatin concentrations linearly. After a linear increase of the estimated thickness as a function of the gelatin concentration, the plasmonic response of the gel-AuNPs was no longer affected by changes in the concentration of gelatin (**Fig. 20 e-f**). The modeling of the plasmonic response of gel-AuNPs and estimation of the average gelatin thickness of the AuDNPs-LY@Gel_x allowed for the reverse design of a system in which the desired coating thickness was achieved by tuning the concentration of gelatin used to create the outer shell. Conversely, it was possible to tune the amount of galunisertib loaded in the DNPs by varying the concentration/thickness of gelatin capping the plasmonic nanosystem.

4.2.3 Evaluation of the galunisertib loading capacity of the AuDNPs-LY@Gel_x with different gelatin thicknesses

It has been shown that gelatin is preferentially degraded by trypsin rather than lipase and amylase, and that trypsin overexpression is often associated with tumor progression and metastases.^[143] To mimic the tumor microenvironment, *in vitro* release tests were carried out in PBS pH 7.4 with a large excess of trypsin. The LC and encapsulation efficiency (EE) of AuDNPs-LY@Gel_x were quantified by RP-HPLC and compared to the control sample AuDNPs (in which gelatin was used only as the AuNPs stabilizer). The influence of the gelatin concentration and thickness on the AuDNPs-LY@Gel_x was measured to investigate the ability of gelatin to improve the LC of AuDNPs. The LC and EE of the AuDNPs-LY (without the gelatin shell) quantified as a control was 2.4 ± 0.2 and 0.48%, respectively. The loading efficiency of DNPs-AuNPs (decorated with gel-AuNPs) was higher than the one of DNPs-AuNPs-LY@Gel (**Fig. 12**), which, instead, were coated by gelatin. This is due to the ability of the gelatin stabilizing AuNPs to interact with galunisertib by Au-N chemisorption and favor its entrapment in the AuDNPs-LY. Therefore, the replacement of PEG (used in the DNPs-AuNPs synthesis) with gelatin (used in the synthesis of AuDNPs) improved the galunisertib LC and EE of the AuDNPs-LY. Later, we investigated the variation of the LC and EE by increasing the concentration of gelatin, figuring out a way to modulate the desired LC to the shell on the DNPs (**Fig. 21 a**). The increase of gelatin concentration/thickness in the shell resulted in a higher amount of drug entrapped in the system and available for delivery to the desired site of action. The AuDNPs-LY@Gel_{0.125%} exhibited a LC of 2.5 ± 0.3 similar to

the control AuDNPs-LY, indicating that such a concentration of gelatin could not improve the LC of the NPs. Conversely, when the gelatin concentration increased from 0.125 to 0.25 %, the ability to retain galunisertib increased and the LC of the sample improved up to 2.8 ± 0.3 , with an EE of 0.6%. The samples AuDNP-LY@Gel_{0.5%} and AuDNP-LY@Gel_{0.75%} exhibited a higher LC and EE of 3.5 ± 0.4 (EE=0.7 %) and 5.23 ± 0.5 (EE=1.04 %), respectively, confirming that the higher the concentration of gelatin in the shell, the higher the amount of entrapped drug. The LC swiftly approached the saturation point in the sample AuDNP-LY@Gel_{1.5%}, which showed the highest LC (LC_{max}) of 5.6 ± 0.6 and an EE of 1.12% (**Fig. 21 a**). The samples displayed a similar release profile with 50% of galunisertib released within 20 minutes due to the degradation of the gelatin shell by trypsin. The quick degradation did not allow us to appreciate any kinetics of the drug release from the samples. However, the drug release profile of gelatin-capped nanocarriers was already investigated in section 4.1.

The LC of nanocarriers is generally a non-modifiable parameter, and it is not obvious that NPs have the adequate LC for the encapsulation of the desired therapeutic dose. In this scenario, to reach the desired amount of released drug in the cells, the quantity of administered NPs must be increased, thus increasing the likelihood of cell toxicity. The proposed approach of polymer coating, instead, allowed for increasing the amount of drug released to the site of action without arising the administered dose of NPs but improving their LC. The variation of the LC in response to the increasing concentration of gelatin in the outer shell followed a typical sigmoidal behavior (**Fig. 21 b**). The amount of galunisertib retained in the

AuDNP-LY@Gel_x did not show significant variation for gelatin concentrations $\leq 0.125\%$ (toe region). The drug LC of AuDNP-LY@Gel_x followed a similar sigmoidal curve as a function of the gelatin estimated average thickness (**Fig. 21 c**) and any enhancement of loading efficiency was observed for gelatin average thicknesses below ≤ 6 nm. At higher gelatin concentrations, the nanosystem LC changed proportionality reaching a plateau region in the sample with the highest concentration and thickness of gelatin (AuDNP-LY@Gel_{1.5%}). The improved drug retention can be explained by considering the non-covalent interactions between gelatin and galunisertib. Type-B gelatin showed an IEP value between 4.7-5.2 and an almost neutral charge at a pH 4.5. When the system was dispersed in the gelatin solution pH 4.0, the physisorbed galunisertib exhibited a negligible positive surface charge on the quinoline-carboxamide group. The strength of the Van der Waals interactions occurring between the drug and gelatin increased linearly with the gelatin concentration, allowing for a better retention of galunisertib. Moreover, by raising the gelatin concentration, a larger polymer matrix was crosslinked as well, thus inhibiting the diffusion of the drug molecules out of the system.

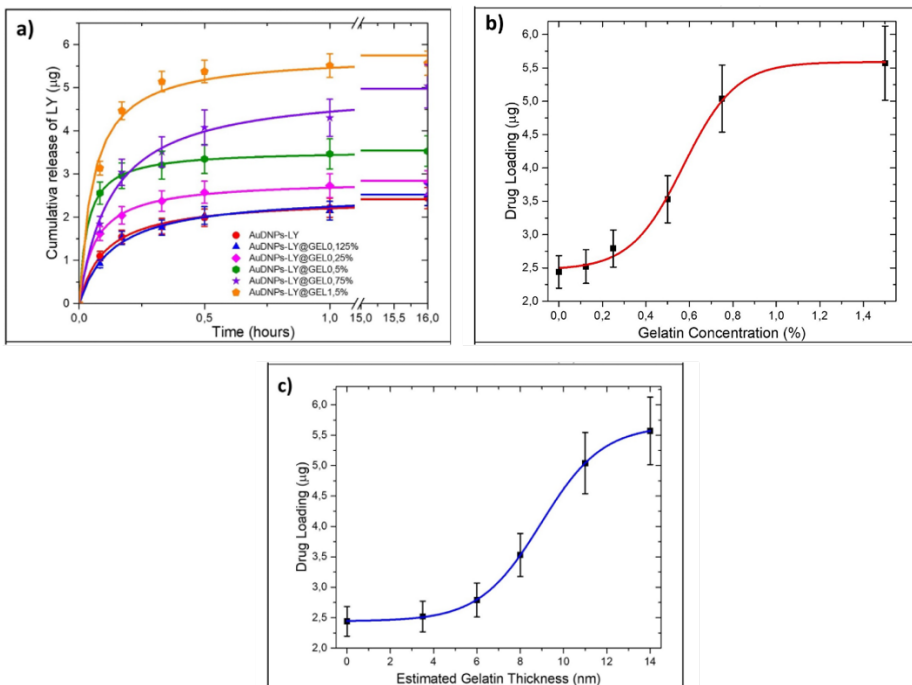


Figure 21. Correlation of the drug-loading capacity of AuDNPs-LY@Gel_x with the gelatin shell. (a) Cumulative release of galunisertib from AuDNPs-LY@Gel_x in PBS containing trypsin (60 µg/mL). (b) Experimental estimation of the drug-loading capacity varying the concentration of the gelatin shell. (c) Theoretical estimation of the drug-loading capacity according to the increasing thickness of the gelatin shell. The vertical bars are representative of the SD on a minimum of n>3 measurements.

The sigmoidal relationship between the drug LC (µg) of AuDNPs-LY@Gel_x and estimated gelatin shell thickness (t) can be explained by the following Boltzmann equation:

$$LC = LC_{max} + \frac{(LC_{min} - LC_{max})}{1 + e^{\frac{t - (\frac{t_{max}}{2})}{\Delta t}}} \quad (6)$$

Where LC_{max} and LC_{min} are the maximum and minimum amounts of galunisertib loaded in the AuDNPs-LY@Gel_x, t is the estimated gelatin thickness, t_{max} is ~ 18 nm, and Δt is:

$$\Delta t = \frac{LC_{max} - LC_{min}}{4 \left. \frac{d(LC)}{dt} \right|_{t = \frac{t_{max}}{2}}} \quad (7)$$

The LC trend of the AuDNPs-LY@Gel_x as a function of the estimated gelatin thickness reported in **Figure 21 c** exhibited three different regimes, described by the Boltzmann type equation (Eq. 6): a toe region in which the gelatin thickness did not affect the LC capacity of the NPs (0-5 nm); a linear region in which the LC varied proportionally to the estimated gelatin thickness (511 nm) due to the increase of the interactions between galunisertib and gelatin; and a saturation region (1114 nm) in which the drug, whose experimental concentration was constant (1 mg mL⁻¹), represented the limiting factor of the loading efficiency.

4.2.4 Application of the developed optical nanosystem for the monitoring of galunisertib release by absorption studies

The complete optical modeling of the AuDNPs-LY@Gel_x can be used to monitor the gelatin shell formation and degradation by UV-Vis, due to the LSPR response of gel-AuNPs to the changes of the local refractive index. The presence of gel-AuNPs on the DNPs enabled monitoring the degradation of the outer gelatin shell and consequent drug release with a fast and cost-effective absorption analysis (**Fig. 22 a**). Through the proposed nanosystem and optical modeling, the characterization of the

NPs (*i.e.*, decoration with AuNPs, drug-loading, and gelatin formation shell) could be assessed by measuring the LSPR peak by UV-Vis rather than using costly equipment, such as the TEM.

According to the theoretical model, the degradation of half of the gelatin shell causes the release of half of the loaded drug from the nanocarrier and a blue shift of the LSPR. As a proof of concept, the blue shift associated with the degradation of the outer shell of the AuDNPs-LY@Gel_{0.125%} was reported in **Figure 22 b**. Trypsin-mediated degradation of gelatin reduced the medium effective refractive index from 1.54 (with gelatin) to 1.33 (without gelatin and corresponding to the refractive index of H₂O) in the surroundings of gel-AuNPs. Due to this remarkable change, the degradation of 100 % of gelatin resulted in a blue shift of both λ_{\max} and λ_2 of LSPR of the AuDNPs-LY. The blue shift due to the gelatin degradation should be equal and opposite to the redshift caused by the formation of the gelatin shell on the AuDNPs. Figure 22 b reports the theoretical shifts of the absorption spectra of the AuDNPs-LY and AuDNPs-LY@Gel_{0.125%}, highlighting a perfect overlapping of the spectra before the gelatin shell formation and after degradation, respectively. To further validate our modeling for gelatin degradation, the LSPR peak of the AuDNP-LY@Gel_{0.125%} system was measured after *in vitro* release test with trypsin. As predicted by the experimental first derivatives of the absorption spectra of our model (**Fig. 22 b**), the inflection wavelength of the AuDNPs-LY@Gel_{0.125%} after gelatin degradation exhibited a blue shift compared to its initial position. However, the LSPR of the AuDNP-LY before gelatin formation (blue) did not overlap with the AuDNPs after gelatin degradation and drug release (purple). We attributed the non-overlapping

resonances to the hybrid nature of the gel-AuNPs, whose relative dielectric constant was measured considering gelatin inclusions in the AuNPs. Gelatin stabilizing AuNPs could be degraded by trypsin as well as gelatin in the shell, affecting the optical properties of AuDNPs-LY after polymer degradation. However, due to the very slight variation in root mean square between theoretical and experimental results, this unexpected effect was considered negligible.

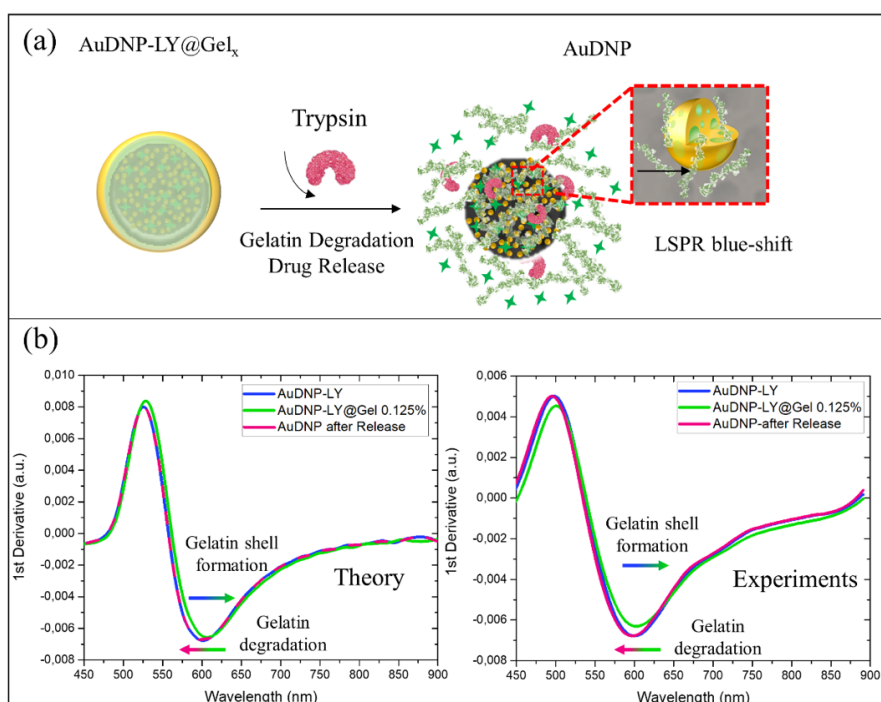


Figure 22: (a) Schematization of the *in vitro* gelatin degradation and drug release. (b) Theoretical and experimental first derivatives of the absorption spectra of the AuDNPs-LY (blue line), AuDNP-LY@Gel_{0.125%} (green line), and after drug release and gelatin degradation (purple).

4.3 Microfluidic-assisted production of gastro-resistant active-targeted diatomite nanoparticles for the local release of galunisertib in metastatic CRC cells

This section describes the results reported in the following publication. The SI of the manuscript can be accessed here: <https://doi.org/10.1002/adhm.202202672M>.

C. Tramontano, J. P. Martins, L. De Stefano, M. Kemell, A. Correia, M. Terracciano, N. Borbone, I. Rea, H. A. Santos, Microfluidic-Assisted Production of Gastro-Resistant Active-Targeted Diatomite Nanoparticles for the Local Release of Galunisertib in Metastatic Colorectal Cancer Cells, *Adv. Healthcare Mater*, 2022, 2202672.

4.3.1 Production, physicochemical characterization, and microfluidic encapsulation of L1-CAM-targeting DNPs-Gel for oral administration.

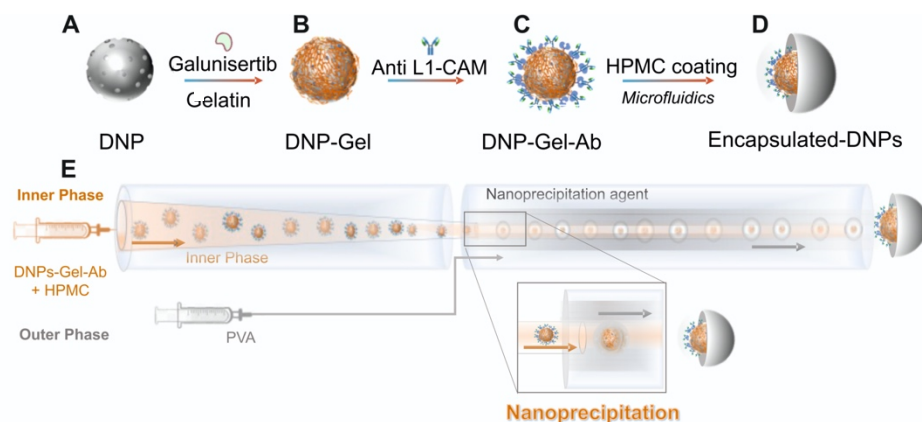
Oral administration is not only the easiest and most tolerated drug delivery route but also the most common way to treat colon diseases locally, and thus represents an attractive approach for the treatment of CRC. Despite the encouraging preclinical results, the clinical translation of galunisertib calls for multiple dosing strategies due to first-pass effects and drug metabolization after oral administration. Particle size is an important parameter in the choice of the appropriate administration route. The intravenous injection is generally suggested for NPs smaller than 150 nm but it is not suitable for DNPs with an average size of 350 nm.^[144] The most suitable administration for this system, instead, is represented by the

oral route. It has been demonstrated that the small intestine epithelium can easily uptake particles 1 μm in size, offering the highest level of tissue uptake for NPs with an average size of 200-500 nm.^[145] Particles with smaller sizes are easier to be metabolized outside the body, reducing the retention time of the delivered drug in the tumor site.^[146,147] Bigger NPs, instead, are more likely to be retained in the tissues upon oral administration, thus increasing the drug availability at the target site.

The results described in previous sections showed that gelatin-capped DNPs (DNPs-Gel) actively targeting L1-CAM provided new tools for protecting and delivering galunisertib, improving drug efficacy and enabling its accumulation in the target site. The oral administration of active targeted DNPs-Gel is, however, a hard task due to the degradation of gelatin by digestive enzymes in the GI tract, which would cause the undesired release of galunisertib. The development of a gastro-resistant coating on the DNPs-Gel by microfluidics could overcome gelatin degradation in the stomach and help address the drug release in the colon. The major advantage of using microfluidics for the encapsulation of DNPs in enteric coatings is the high batch-to-batch reproducibility of the formulations provided by the well-controlled flow rates of polymer solutions and NPs inside micrometer-sized channels.

The DNPs serving as oral drug nanocarriers were functionalized and encapsulated as sketched in **Scheme 1** to fabricate a gastro-resistant oral formulation capable of delivering galunisertib specifically to CRC cells. First, the diatomite earth powder was dispersed in ethanol and ultrasonicated for 160 h to reduce the size of the frustules at the nanoscale level. DNPs were centrifuged, collected, and purified with a mixture of

H₂SO₄ and H₂O₂ to purge the organic contamination, and with HCl to remove metal residues. Then, they were washed with Milli-Q H₂O to remove traces of the acid treatments, and aminosilanized with 10% v/v APTES solution (referred to as “DNPs”) as previously described.^[29,61] The produced DNPs were loaded with galunisertib and further covered by a layer of crosslinked gelatin (0.5% w/v) (**Scheme 1A-B**). Then, the anti-L1-CAM antibody was bound to the gelatin layer via pr-A, and the DNPs-Gel-Ab were encapsulated in HPMC by microfluidics for oral administration (**Scheme 1C-D**).



Scheme 1. Schematic representation of the developed DNPs and their encapsulation *via* microfluidics. (A-B) Galunisertib loading and coverage of DNPs with gelatin. (C) Modification of the DNP-Gel with the anti-L1-CAM antibody. (D) Encapsulation into the enteric polymer. (E) Design of the microfluidic channel, which is composed of an outer capillary, in which the nanoprecipitation agent polyvinyl alcohol (PVA) is pumped, and an inner capillary through which the dispersion of DNPs -Gel-Ab and HPMC is injected.

The DNPs produced by ultrasonication and purification approaches had an average size of 360 ± 50 nm and a surface charge of -10 ± 3 mV due to the negatively charged hydroxyl groups ($-\text{OH}$) (**Figure 23 A**). The gelatin layer induced a slight increase in the DNPs' size (about 40 nm) and provided the surface with positive $-\text{NH}_2$ useful for further functionalization steps. Gelatin was crosslinked by EDC/NHS as intensively described throughout this work. The coating with crosslinked gelatin increased the PDI of the DNPs from 0.30 ± 0.04 to 0.40 ± 0.05 as expected due to the low degree of control over the bulk mixing process of gelatin with the DNPs. The encapsulation of DNPs in gelatin and further crosslinking could also be carried out in a microfluidic platform with 3 inlets, in which the dispersion of DNPs and gelatin, antisolvent solution, and crosslinking agents are pumped separately.^[148] The chemical crosslinking by EDC/NHS is generally a time-consuming step taking 1 h in controlled pH conditions. Unfortunately, long-term reactions may increase the likelihood of particle deposition on the bottom of the channel and contribute to complete or partial clogging. Alternative crosslinking techniques, such as cooling or irradiation, would be more adequate for this technology.^[149] Due to this limiting aspect, herein, the gelatin coating on the DNPs was performed by bulk mixing.

For binding the anti-L1-CAM antibody to the NPs, we attached pr-A to the $-\text{NH}_2$ groups of the gelatin by EDC/NHS and then incubated pr-A-modified DNPs-Gel with the antibody. The DNPs-Gel-Ab showed an average size of 410 ± 20 nm and a surface charge of 16 ± 4 mV (**Fig. 23 B**), which later on favored the interaction with the negatively charged functional groups of the HPMC. This enteric polymer is a regular excipient

of solid dosage forms, widely used as a coating material for orally-administered formulations to protect the drug from the harsh acidic conditions of the stomach.^[113] For the encapsulation of DNPs-Gel-Ab in HPMC, we used a microfluidic platform consisting of inner and outer capillaries aligned in a co-flow geometry (**Scheme 1E**). The inner phase composed of a dispersion of DNPs-Gel-Ab and HPMC in 50:50 ethanol:water was pumped into the inner capillary, whereas the nanoprecipitation agent polyvinyl alcohol (PVA) was injected from the outer to the inner capillary.^[115] The inner and outer phases flowed in the same direction to create a 3D coaxial flow, in which the aqueous PVA solution helped the precipitation of HPMC and the entrapment of DNPs-Gel-Ab in the polymer matrix. Compared to the conventional bulk mixing methods, this technology allowed for a precise encapsulation of DNPs-Gel-Ab due to the possibility of controlling volumes and flow rates of the two phases. The encapsulation was confirmed by a decrease in the size and PDI of the formulation, which turned from 410 ± 20 to 320 ± 10 nm and from 0.40 ± 0.05 to 0.25 ± 0.01 , respectively, due to the improved morphology and stability provided by the homogeneous polymeric coating. The controlled encapsulation provided the system with a less irregular shape (**Fig. 23-C III**), which, in turn, improved the PDI. The nanoprecipitation of HPMC was also confirmed by the negatively charged surface of encapsulated-DNPs, which turned from 14 ± 4 to -20 ± 1 mV due to the $-\text{COOH}$ of the polymer matrix. The consistent negative surface charge of the encapsulated DNPs increased the repulsion forces between encapsulated-DNPs and avoided their aggregation. The HPMC was first absorbed on the DNPs-Gel-Ab flowing through the inner capillary, and, later on, the

antisolvent PVA solution caused the nanoprecipitation of HPMC and the formation of a controlled coating around encapsulated-DNPs. The likelihood of NPs' aggregation with this technique is lower than with the bulk mixing method, due to the continuous adjustment of the reaction conditions over the mixing rates of reagents.^[150]

TEM imaging showed that the ultrasonication approach produced DNPs with irregular size and shape (**Fig. 23 C-I**), which are the expected features of this type of NPs. However, the uneven surface of DNPs is not likely to affect their interactions with the cells, as previously reported.^[64] The gelatin was absorbed into DNPs creating a thin layer that made the surface of DNPs smoother (**Fig. 23 C-II**). Since the bulk mixing of gelatin and DNPs offered a low control over the process, free gelatin not embedding the DNPs-Gel-Ab was detected on the TEM grid. However, after encapsulation in HPMC, the formulation showed a higher homogeneity in morphology, because of the well-controlled microfluidic process (**Fig. 23 C-III**). The improved morphology provided by microfluidics was in line with the decreased PDI value obtained with the DLS. The DNPs were further characterized by attenuated total reflectance (ATR)-FTIR and energy dispersive X-ray (EDX) spectroscopy at different steps of functionalization (**Fig. 23 D-E**). The FTIR spectrum of DNPs showed two characteristic absorption bands at 1075 and 800 cm^{-1} related to the Si-O-Si, and the band at 1600 cm^{-1} ascribed to the aminosilanization (**Fig. 23 D**).^[29] This band increased in the DNPs-Gel-Ab and can be related to both the crosslinked gelatin (C-N) and antibody (N-H) labeling, which resulted in a positive surface charge of DNPs-Gel-Ab (**Fig. 23 D**).^[151] The C-O stretch at 1740 and 1230 cm^{-1} , and the C-H band at 2927 cm^{-1} in the

spectrum of encapsulated-DNPs confirmed the presence in the sample of an organic matrix of HPMC in the sample.^[152] The proof that DNPs-Gel-Ab were encapsulated in HPMC was obtained by EDX elemental analysis (**Fig. 23 E**). We analyzed both the inner DNPs-Gel-Ab and the polymer matrix surrounding them. The silicon (Si) peak appeared in the spectrum when we analyzed the content of encapsulated-DNPs, that is the DNP-Gel-Ab, whereas only the carbon (C) peak was detected when we investigated the polymer matrix of HPMC. Overall, the EDX analysis confirmed that the DNPs-Gel-Ab were efficiently entrapped in the HPMC by creating an in-out structure, in which the inner part was composed of the DNPs-Gel-Ab and the outer of the HPMC polymer.

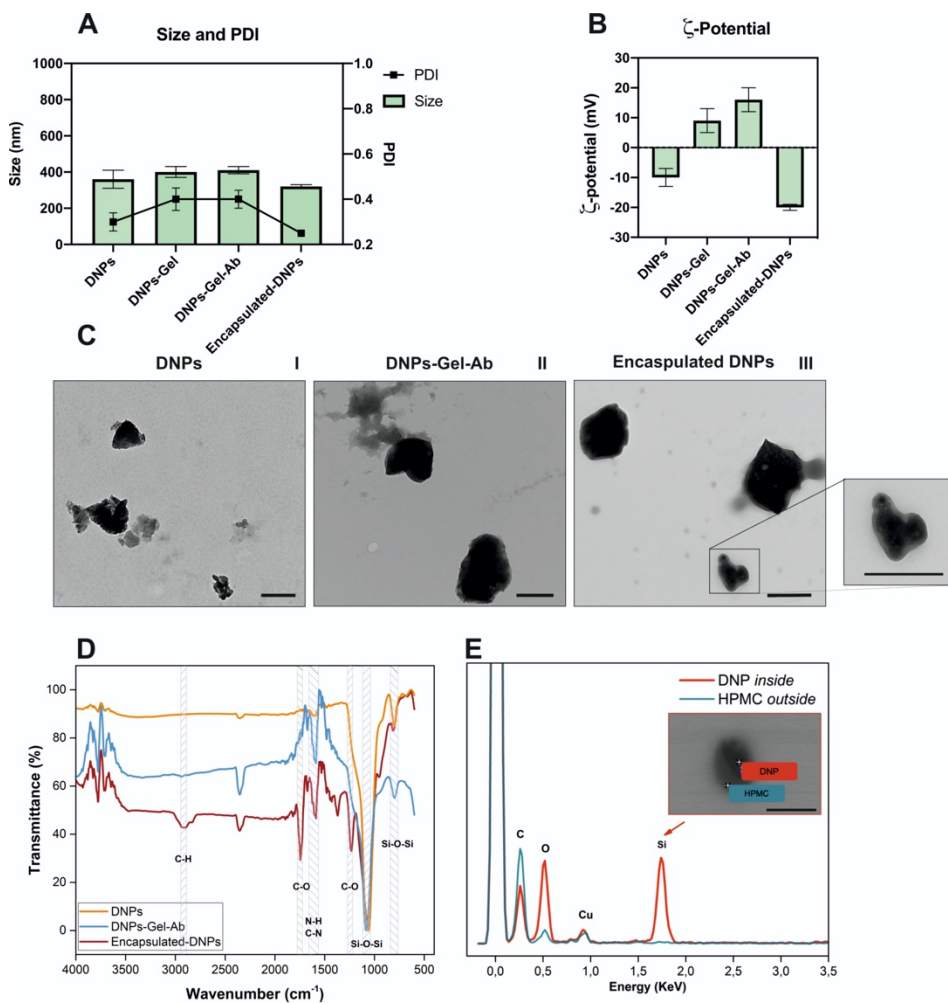


Figure 23. Characterization of the physicochemical properties of the developed DNPs. (A) Size and PDI, and (B) ζ -potential. Results are expressed as mean \pm s.d. ($n \geq 3$). (C) TEM images of DNPs (I), DNPs-Gel-Ab (II), and encapsulated-DNPs (III). The scale bars are 500 nm. (D) ATR-FTIR spectra of the DNPs, DNPs-Gel-Ab, and encapsulated-DNPs. (E) Elemental composition of encapsulated-DNPs by EDX analysis.

4.3.2 Drug-loading, release, and dissolution studies of the encapsulated-DNPs

The transit through the GI tract is influenced by different parameters, including the residence time, pH, and presence of digestive enzymes.^[153] The gastric time can vary from patient to patient and ranges from 0–2 h, whereas the transit in the small intestine is considered relatively constant (4 h). The colonic transit time can be, instead, highly variable and affected by the local disease, with ranges from 1 to 50 h.^[154] Therefore, to study the behavior of the encapsulated-DNPs in the GI tract, we dispersed encapsulated-DNPs in SGF pH 1.6 with pepsin (1 mg mL^{-1}) for 2 h. Then, the encapsulated-DNPs were dispersed in FaSSIF pH 5.5 enriched with trypsin (0.06 mg mL^{-1}). The concentration of trypsin along the small and large intestine can vary significantly from 0.03 mg mL^{-1} to 0.13 mg mL^{-1} from the upper part of the bowel to the lower duodenum.^[143] Due to these fluctuations, we used a mean value of trypsin concentration (0.06 mg mL^{-1}) for mimicking the passage of the encapsulated-DNPs through the intestine, as also reported elsewhere.^[61] To simulate the transit through the colon, the encapsulated-DNPs were then dispersed in FaSSIF pH 8.0 supplemented with trypsin for 2 h.^[155] Before the galunisertib release studies, we investigated the drug LC of the DNPs-Gel-Ab and encapsulated-DNPs. To this aim, the DNPs-Gel-Ab were dispersed in 1 mL of PBS solution supplemented with trypsin to degrade the gelatin matrix, then they were centrifuged, and supernatants were analyzed by RP-HPLC. The encapsulated-DNPs, instead, were first dispersed in 70% ethanol to dissolve the polymer matrix, and then suspended in a PBS solution enriched with trypsin to favor the enzymatic degradation of gelatin.

The DNPs-Gel-Ab and encapsulated-DNPs showed a very similar galunisertib LC of 4.5 ± 0.3 and 4.0 ± 0.2 %, respectively. The decreased LC after encapsulation can be explained by the loss of the drug that was loosely absorbed on the surface of DNPs-Gel-Ab and, thus, released during the encapsulation process. The loading capacity of encapsulated-DNPs is consistent with the loading efficiencies reported by immersion methods for most existing nanocarriers with a similar porosity.^[90] Higher loading efficiencies were achieved by increasing the surface area of NPs, which is a non-tunable parameter for naturally porous NPs, such as DNPs.^[156,157] We reported in section 4.1 that DNPs-Gel having a lower galunisertib loading capacity of 2 (0.4) % inhibited the metastatic signaling in CRC efficiently.^[29] Here, a higher LC of 4 (0.2) % was achieved by increasing the concentration of gelatin in the outer shell, as suggested by previous results.^[61] Due to the improved LC of encapsulated-DNPs, a non-toxic concentration of NPs can be administered to inhibit migration with greater efficiency than the free galunisertib.

Due to the diverse external shells, the drug release profiles of the DNPs-Gel-Ab and encapsulated-DNPs were very different and followed distinct release kinetics (**Fig. 24 A**). For the DNPs-Gel-Ab, we observed a burst release of galunisertib at pH 1.6 within 30 min, due to both the acidic microenvironment and the presence of pepsin. Gelatin is a pH-responsive polymer unfolding at pH <5 and can be degraded by pepsin on the N-terminal residues. Therefore, the gelatin matrix in the DNPs-Gel-Ab got unfolded in the SGF buffer, and, as a consequence, the chains got accessible to the pepsin, which degraded the polymer and favored the release of 100% of galunisertib in less than 30 min.^[97] For the

encapsulated-DNPs, instead, only 20% of galunisertib was released after 2 h in the medium pH 1.6, whereas a consistent amount of the drug (about 80%) was released in FaSSIF pH 5.5. The gastro-resistant HPMC matrix protected the gelatin layer covering the surface of DNPs from the acidic pH, making the N-terminal residues of gelatin inaccessible to pepsin degradation. As soon as the polymer started degrading in FaSSIF pH 5.5, the gelatin on the DNPs-Gel-Ab was degraded by trypsin and galunisertib was gradually released within 4 h. When the encapsulated-DNPs were dispersed in FaSSIF pH 8.0 supplemented with trypsin, the HPMC was completely dissolved, gelatin was digested by trypsin, and 100% of the drug was released at the colon pH. The developed oral formulation was designed to release galunisertib upon dissolution of the enteric coating at the intestinal pH. During the passage between the intestine and colon, however, the HPMC dissolution exposes the inner DNPs-Gel-Ab to the environment and the drug is released upon gelatin digestion. Without the gelatin shell, galunisertib would be released in the intestine quickly. Therefore, the gelatin layer played a crucial role in the developed formulation as it controlled the release of galunisertib in the bowel and ensured its accumulation in the colon. The drug release studies herewith suggest that the critical factors controlling the release of galunisertib from encapsulated-DNPs were the dissolution of both the enteric polymer and gelatin.

To investigate the polymer dissolution, the morphology of the encapsulated-DNPs was analyzed after dispersing the encapsulated-DNPs in SGF at pH 1.6 and FaSSIF at pH 5.5 and 8.0 by TEM (**Fig. 24 B**). The TEM images confirmed that the enteric polymer remained intact when

encapsulated-DNPs were dispersed at pH 1.6 for 2 h. As a result of the gastro-resistant features of the HPMC in these pH conditions, only 20% of the encapsulated drug was released within 2 h (Fig. 24 A).

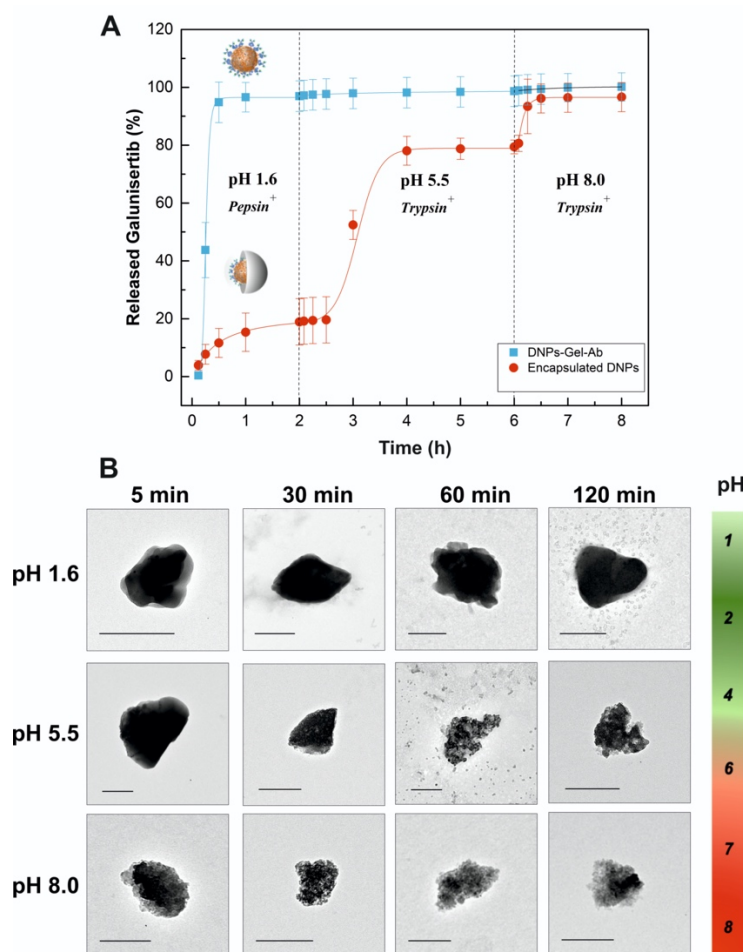


Figure 24. Drug release and dissolution profile studies. (A) The drug release studies of the DNPs-Gel-Ab (blue line) and encapsulated-DNPs (red line) in SGF at pH 1.6 and FaSSIF at pH 5.5 and 8.0 were investigated by RP-HPLC. Results are expressed as mean \pm s.d. ($n \geq 3$). (B) TEM images of the encapsulated-DNPs after incubation in different pH environments. Scale bars are 300 nm.

The dissolution of HPMC occurred rapidly at pH 5.5 since the polymer was completely dissolved after 10 min in the tested pH conditions, exposing the inner DNPs. However, even if the dissolution of the enteric polymer was very fast at pH 5.5, galunisertib was gradually released within 4 h due to the crosslinked gelatin matrix. The TEM images suggested that the HPMC matrix dissolved immediately at pH 8.0 since the enteric matrix was no longer detectable after 5 min and only DNPs could be seen on the TEM grid. Overall, the microfluidic encapsulation in HPMC made the DNPs-Gel-Ab resistant to the harsh conditions of the stomach after oral administration, allowing for the release of galunisertib in the small intestine and colon.

4.3.3 Quantification of L1-CAM expression on Caco-2, HT29-MTX, and SW620 cells and cell viability studies

The L1-CAM is a glycoprotein involved in cancer development and associated with metastases and poor prognosis. The expression of L1-CAM is frequently increased in metastases-initiating CRC cells and promotes their migration and invasion of the liver.^[158] Considering that the developed formulation was envisaged for the treatment of colon cancer, we selected three CRC cell lines expressing different levels of the L1-CAM (SW620, Caco-2 and HT29-MTX) for the *in vitro* studies. The SW620 cell line constitutes a unique model for studying the later stages of CRC since it was derived from a patient affected by Duke's stage B colon carcinoma with liver and lymph node metastases.^[159] The Caco-2 and HT29-MTX cells were isolated from the colon tissue of a patient with colorectal adenocarcinoma, and they both have an epithelial morphology.^[160,161] Moreover, Caco-2 cells represent *ca.* 90% of the

intestinal epithelium, and the goblet-like and mucus-producing HT29-MTX cells represent *ca.* 10% of the intestinal cells.^[162] Therefore, both Caco-2 and HT29-MTX represent the most used *in vitro* gastrointestinal models for investigating the efficacy of oral dosage forms. Since the overexpression of L1-CAM promotes the ETM process by which cells acquire metastatic capacities, we expected that the L1-CAM was overexpressed in the metastatic SW620 cells, whereas Caco-2 and HT29-MTX exhibited basal levels of the antigen. To confirm this, we investigated the expression of the antigen in the Caco-2, HT29-MTX, and SW620 and by FACS (**Fig. 25 A-D**). The SW620, Caco-2, and HT29-MTX cells were incubated with the anti-L1-CAM primary antibody. Then, they were washed to remove the unbound molecules, and incubated with the secondary antibody labeled with a fluorophore. Finally, the cells were washed and sorted by FACS in the APC channel. The expression of the L1-CAM was observed in $20 \pm 4\%$ of Caco-2 cells and $9 \pm 2\%$ of HT29-MTX, suggesting that the epithelial cells express a basal level of the endogenous antigen (**Fig. 25 A-B**). By contrast, as expected based on the metastatic phenotype, $86 \pm 3\%$ of L1-CAM cells expressed the antigen. (**Fig. 25-C**). Hence, the SW620 cell line represented the ideal metastatic target to investigate the potential of our formulation, whereas Caco-2 and HT29-MTX cells served as the epithelial model of CRC cells.

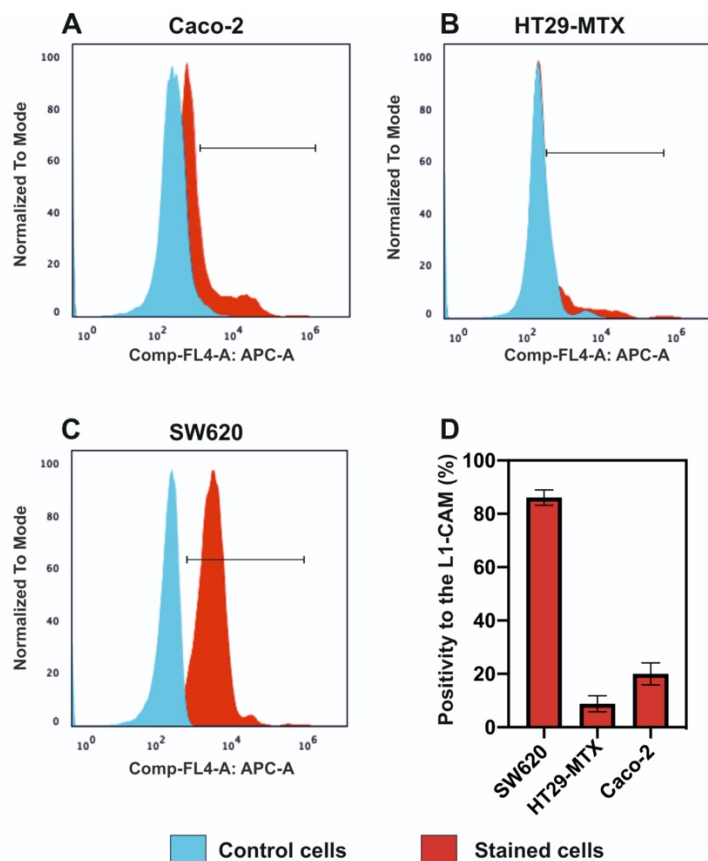


Figure 25. Quantification of L1-CAM expression in (A) Caco-2, (B) HT29-MTX, and (C) SW620 cells by FACS. Cells were incubated with the primary and secondary antibodies and sorted by fluorescence in the APC channel. (D) The statistical analysis is reported as mean \pm s.d. ($n \geq 3$).

After quantifying the expression of the antigen in the selected cell lines, we investigated if any of the components used in the formulation could be toxic to cells for up to 24 h. For this purpose, the SW620, Caco-2, and HT29-MTX cells were incubated with the DNPs at different steps of preparation (DNPs, DNPs-Gel, DNPs-Gel-Ab, and encapsulated-DNPs) at

different concentrations (12, 25, 50, and 100 $\mu\text{g mL}^{-1}$) and time points. The cell viability was measured by using the adenosine triphosphate (ATP)-based luminescence assay after 6 and 24 h of incubation, corresponding to the minimum (6 h) and maximum (24 h) residence time in the GI tract, respectively, when NPs are taken up in the mucosa.^[163] Results showed that all the tested formulations were biocompatible at different concentrations and did not induce toxicity in the SW620, Caco-2, and HT29-MTX cells after 24 h of incubation (**Fig. 26**).

The cell viability of Caco-2 and SW620 cells incubated with each formulation was over 85% after 6 and 24 h of incubation, regardless of the concentration. For HT29-MTX, instead, fluctuations of the cell viability values were observed when the cells were incubated with the DNPs for 6 h. However, even if NPs conditioned the viability of HT29-MTX cells within this time interval, no cytotoxicity was observed. The incubation of the goblet-like cells with the developed DNPs at every step of preparation for a longer time (24 h) did not alter cell viability, which was higher than 80% in each tested condition. Overall, the viability of SW620, HT29-MTX, and Caco-2 cells was higher than 85% after 24 h, demonstrating that none of the developed formulations inhibited cell proliferation. The encapsulated-DNPs, corresponding to the final system, reported high cytocompatibility with both the metastatic and epithelial cell lines up to 100 $\mu\text{g mL}^{-1}$ and 24 h of incubation. The transit of the developed formulation through the colon, however, may be longer than 24 h and take up to 50 h, according to the weight, sex, and health conditions of patients.^[163] A remarkable advantage of using DNPs over organic NPs for oral administration is their thermal and chemical stability, which enables

DNPs to be retained in the colon for up to 50 h without being degraded or affecting cell viability. Our group showed that DNPs can be administered up to a concentration of 2.5 mg mL^{-1} for 72 hours without causing toxicity in vivo, supporting their potential as oral drug delivery systems.^[164]

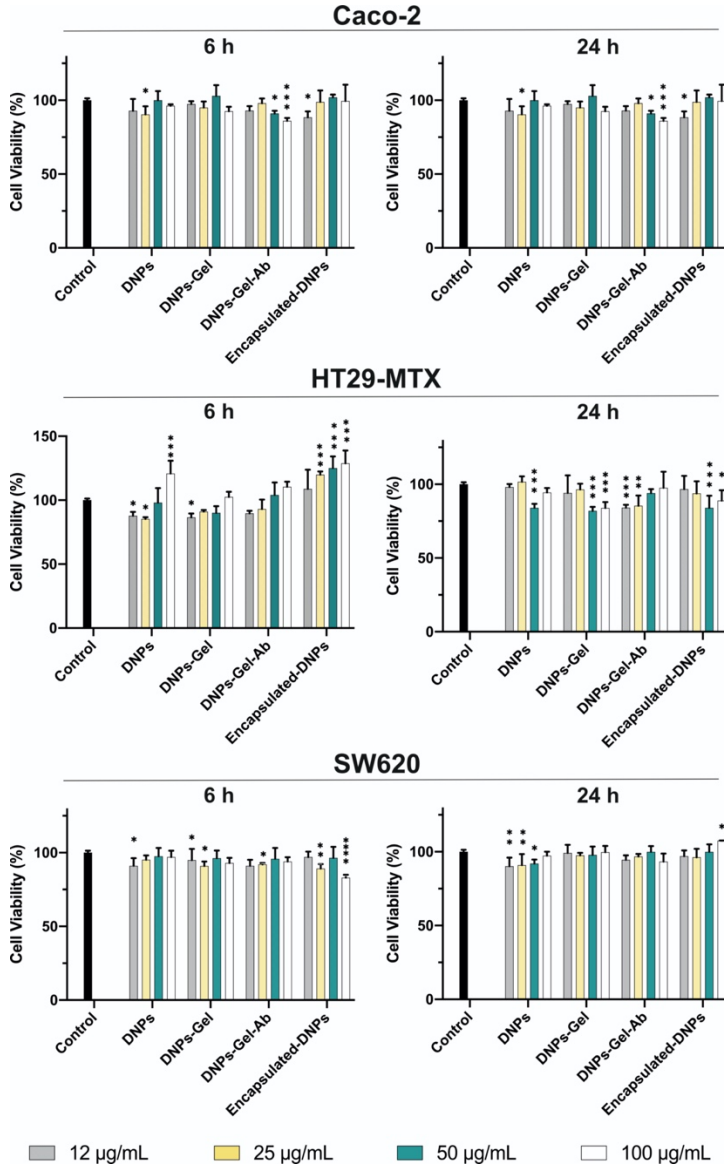


Figure 26. Cell viability (%) of Caco-2, HT29-MTX, and SW620 incubated different concentrations ($25-100 \mu\text{g mL}^{-1}$) of the DNP, DNP-Gel, DNP-Gel-Ab, and encapsulated-DNP. Cells were incubated with HBSS-HEPES buffer (pH 7.2) as the negative control. Each data set was compared to the negative control. The level of significance was set at

probabilities of * $p < 0.05$, ** $p < 0.01$ and *** $p < 0.001$. Results are expressed as mean \pm s.d. ($n \geq 3$).

4.3.4 Cell-DNP interaction studies by confocal microscopy

The chemical composition of the NPs and their surface modifications play a crucial role in the cell-NP interactions and internalization process. For this reason, the surface of NPs can be tailored to promote specific interactions or mediate the internalization by selected pathways. In choosing the appropriate surface functionalization, the cell membrane composition (*i.e.*, antigen, peptides, and protein expression) must be taken into consideration carefully. Here, to promote the interactions of our formulation with the SW620 cell line, the encapsulated-DNPs were modified with the anti-L1-CAM antibody. We hypothesized that the presence of the antibody on the surface of the DNPs could increase the specificity of the interactions with this cell line, rather than with Caco-2 and HT29-MTX expressing basal levels of L1-CAM. To evaluate the efficacy of our targeting approach, we studied the interactions of NPs with the three different cell lines by confocal microscopy (**Fig. 27**). The SW620, HT29-MTX, and Caco-2 cells were incubated with 50 μg of Alexa Fluor[®] 488-labeled DNPs-Gel, DNPs-Gel-Ab, and encapsulated-DNPs in PBS (pH 7.2). At this pH, the HPMC matrix in the encapsulated-DNPs dissolved, exposing the inner DNPs-Gel-Ab. After 24 h, the cells were washed to remove unspecific interactions, and cell membranes and nuclei were stained.

Like many cell lines making epithelial barriers, the Caco-2 monolayer was characterized by the formation of vacuoles, which make these cells function as gut epithelial cells (**Fig. 27**).^[161] The DNPs-Gel were randomly

internalized in this cell line, as shown by the heterogeneous distribution of the NPs on the cell monolayer. The cell-adhesion properties of gelatin covering the DNPs promoted the unspecific interactions of the DNPs with the Caco-2 cells. The DNPs-Gel and DNPs-Gel-Ab showed very similar interactions with these cells, and in both cases, we did not observe any pattern in the cell-DNP interaction. The random DNP distribution on the cell monolayer suggests that the binding of the DNPs-Gel and DNPs-Gel-Ab was driven by unspecific adsorption on the cell surface. Differently from the epithelial cells HT29-MTX and Caco-2, the binding of the encapsulated-DNPs to the targeted cell line overexpressing the antigen was strongly promoted by the presence of the antibody on the surface of NPs. We observed that the antibody-labeled formulation interacted better than DNPs-Gel with the SW620 cells and that the DNPs-Gel-Ab were preferentially concentrated at the cell membrane, where the L1-CAM was expressed.

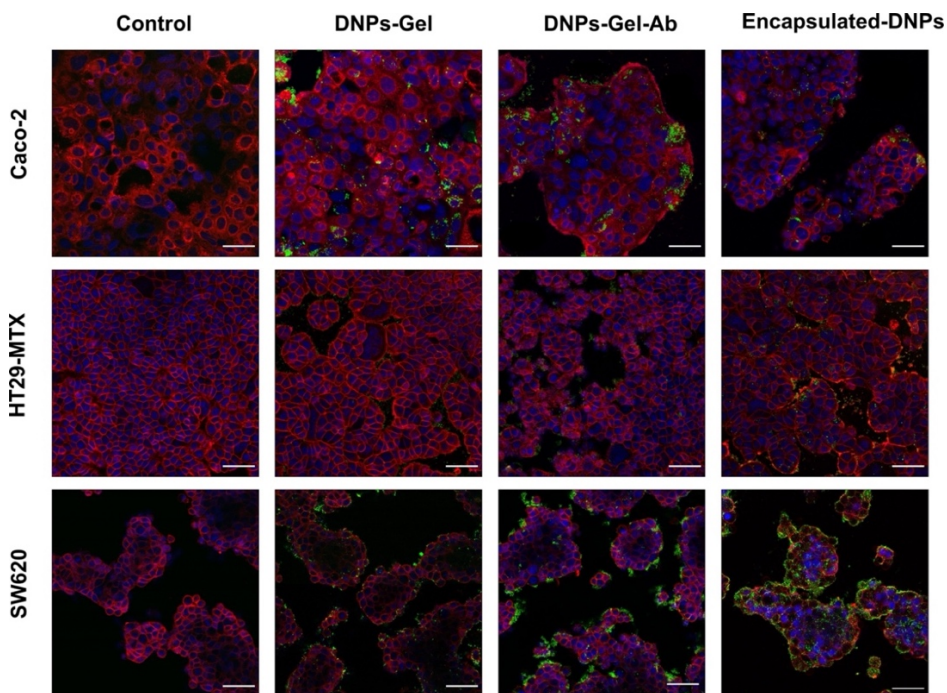


Figure 27. Confocal microscopy of Caco-2, HT29-MTX, and SW620 cells after incubation with 50 μg of DNPs-Gel, DNPs-Gel-Ab, and encapsulated-DNPs for 24 h at 37 $^{\circ}\text{C}$ in PBS. CellMask™ Deep Red was used to stain the cell membranes; DNPs were labeled with Alexa Fluor®-488 and nuclei were stained with DAPI. The scale bars are 50 μm . The images were acquired with a Leica SP8 microscope, using a 63 \times objective.

The internalization of the encapsulated-DNPs in the Caco-2 cell line was reduced compared to the DNPs-Gel and DNPs-Gel-Ab uptake, confirming that the antibody did not drive the cell-DNP interaction, even though *ca.* 20% of the Caco-2 cells expressed the L1-CAM (**Fig. 27**). Similar results were observed with the goblet-like cells HT29-MTX, which exhibited *ca.* 10% positivity to the antigen L1-CAM. Both the DNPs-Gel and DNPs-Gel-Ab showed a few interactions with the HT29-MTX population. The

encapsulated-DNPs seemed to have been internalized in HT29-MTX cells better than the DNPs-Gel and DNPs-Gel-Ab, but the result was not comparable to the SW620 cell line overall. The improved internalization of the encapsulated-DNPs in the epithelial cells can be associated with the reduced size and PDI. The interactions of the final formulation with the targeted cells appeared highly uniform, as demonstrated by the homogeneous distribution of the encapsulated-DNPs on the cell monolayer. Therefore, both the good size distribution provided by the microfluidic process and the active targeting approach enhanced the uptake of the encapsulated-DNPs in the metastatic cell line. The amount of the encapsulated-DNPs detected in the green channel (**Fig. 27**) was more consistent when NPs were incubated with the metastatic cell line rather than with Caco-2 or HT29-MTX cells. The antigen-antibody binding efficiently enhanced the interactions of the NPs with the cell line expressing high levels of the antigen, as seen for the SW620 cells. On the contrary, its effect was negligible for cells expressing basal levels of L1-CAM, such as the Caco-2 and HT29-MTX cell lines. The obtained results provided qualitative information on the interaction of the encapsulated-DNPs with the three selected cell lines. However, the detection of cell-DNPs interactions may be negatively impacted by particular features of the cell monolayer, such as the cytoplasmic vacuolization observed only in Caco-2 cells. To further support the findings obtained by confocal microscopy, we measured the uptake of the developed formulation in the cells and quantified the efficacy of the active targeted approach by FACS.

4.3.5 Specificity of the antibody-labeled DNP uptake in cells by FACS

The number of DNPs internalized or firmly bound to the cell membrane was investigated by flow cytometry to quantify the uptake of the encapsulated-DNPs in the three selected cell lines. According to the quantification of L1-CAM in the CRC cell lines (**Fig. 25**) and the interaction studies (**Fig. 27**), the uptake of the encapsulated-DNPs was expected to be higher in the SW620 than Caco-2 and HT29-MTX cells. To investigate the NP uptake, the metastatic and epithelial cells were incubated with the Alexa Fluor[®]488-labeled DNPs-Gel, DNPs-Gel-Ab, and encapsulated-DNPs for 24 h, and then the unbound NPs were removed with washings. The cells were detached by trypsin, washed again, and analyzed (**Fig. 28**). Since the fluorophore on the DNPs was attached to the gelatin shell, which is degradable by trypsin, the fluorescence signal of DNPs absorbed on the cell membrane was quenched by the detachment step. Consequently, we measured the fluorescence of internalized DNPs by FACS.

We found that the uptake of both the DNPs-Gel-Ab (25.0 ± 0.5 %) and encapsulated-DNPs (26 ± 1 %) in Caco-2 cells was close to the DNPs-Gel (25 ± 1 %) (**Fig. 28 A**) and mainly unspecific, as also shown by the confocal microscopy analysis (**Fig. 27**). Similarly, the internalization of both the antibody-labeled and unlabeled DNPs in the HT29-MTX was comparable to each other, ruling out any specific pattern in the internalization (**Fig. 28 B**).

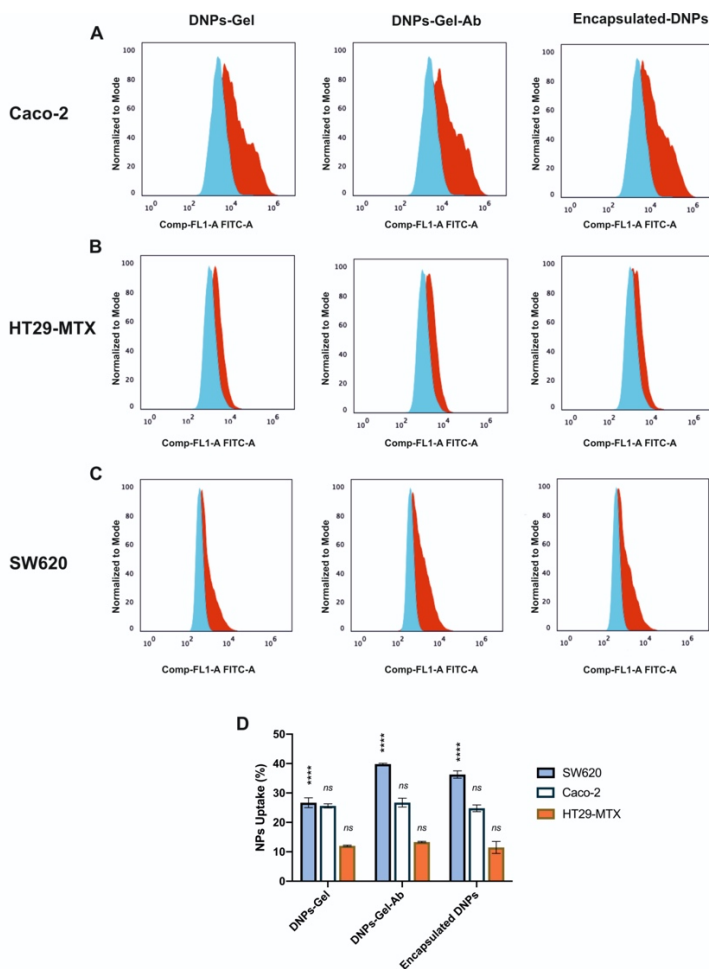


Figure 28. Cell uptake studies. Normalized fluorescence intensity after incubation of (A) Caco-2, (B) HT29-MTX, and (C) SW620 cells with the labeled DNPs-Gel, DNPs-Gel-Ab, and encapsulated DNPs for 24 h. Control cells (blue histogram) were incubated with PBS and analyzed to measure cell autofluorescence. After incubation with DNPs, cells (red histogram) were sorted by fluorescence in the FITC channel. (D) Statistical analysis of DNPs' uptake. The level of significance was set at probabilities of * $p < 0.05$, ** $p < 0.01$ and *** $p < 0.001$. Not statistically significant values are reported as “ns”.

The average uptake of the DNPs-Gel, DNPs-Gel-Ab and encapsulated-DNPs in the HT29-MTX cells was 11 ± 2 % of the total amount of NPs incubated with the cells (**Fig. 28 B-D**). Therefore, the uptake of the antibody-labeled DNPs (DNPs-Gel-Ab and encapsulated-DNPs) in the cells with basal expression of the antigen was mainly unspecific compared to the SW620 cell line. In the cells expressing abnormal levels of the, the functionalization of DNPs-Gel-Ab and encapsulated-DNPs with the antibody anti-L1-CAM improved the cell internalization by 13% compared to the untargeted DNPs-Gel (**Fig. 28 C-D**). The uptake of the DNPs-Gel in the metastatic cells was reported to be 27 ± 2 %, which was comparable to the uptake of the same formulation in the Caco-2 cells. However, the internalization of the DNPs-Gel-Ab with the SW620 cells was measured to be 40.0 ± 0.2 %, corresponding to an internalization about 15 higher than in Caco-2 and 30 % greater than in HT29-MTX. (**Fig. 28 D**). Overall, the DNPs-Gel showed a good cell uptake in both Caco-2 and SW620, confirming the ability of DNPs to penetrate cancer cells and serve as nanocarriers. Additionally, here, the antibody-labeled formulations showed an improved cell uptake in the targeted SW620 cells overexpressing the antigen, due to the antibody-antigen affinity. Moreover, even though the DNPs are generally taken up in the CRC cell lines passively, the actively targeted functionalization moved towards the specific uptake of NPs in the CRC cell line overexpressing the L1-CAM.

4.3.6 Encapsulated-DNPs inhibit the migration of the metastatic cell line SW620

The ability of metastatic cells to migrate and colonize a secondary tumor site is promoted by the upregulation of both the TGF- β pathway and

overexpression of the L1-CAM. The TGF- β pathway promotes the nuclear transcription of pro-metastatic genes (e.g., Twist, SNAIL, and Vimentin), whereas the L1-CAM mediates the adaption to the stroma and adhesion to blood capillaries. Hence, the blocking of both the targets (TGF- β and L1-CAM) can slow down the metastatic cells' ability of invading and colonizing a perivascular site. We investigated whether the release of galunisertib from the encapsulated-DNPs in the SW620 cells could block the TGF- β pathway, thus reducing the cell migratory capacity. For this purpose, the SW620 cells were seeded in a wound-healing assay chamber and allowed to reach 90% confluency for 48 h. After that, we studied the migration of the control cells incubated with DMEM supplemented with 0.5% FBS to slow down cell proliferation. To compare the effect of free galunisertib to that of the drug delivered by our NPs, we dispersed either galunisertib (LY) 2.5 μM or drug-loaded encapsulated DNPs 26 $\mu\text{g mL}^{-1}$ (reported as encapsulated-DNPs-LY in **Fig. 29**) in the culture media and studied the cell migration under starvation. The mass of drug-loaded encapsulated-DNPs that released an amount of galunisertib equivalent to the free drug was calculated by the drug release studies (section 4.3.2). Then, to evaluate any contribution of the developed NPs on the cell migration, we also investigated the effect of the empty encapsulated-DNPs (26 $\mu\text{g mL}^{-1}$) on the cells (reported as encapsulated-DNPs). The cell migration was measured as the percentage of wound closure (**Fig. 29**). The migration of the untreated cells started only after 48 h and reached $30 \pm 3\%$ of wound closure after 120 h in starvation (**Fig. 29 A-B**). The cells were kept under starvation in 0.5% FBS DMEM to slow down cell proliferation, which could contribute to wound closure and affect the result

of the experiment. Therefore, the migration observed in the control cells (30%) was only due to the capacity of cells to migrate towards the wound area and was not affected by their proliferation. The effect of galunisertib on the cell line was negligible within 48 h and started to be consistent at 96 h when cells began to invade the wound area (**Fig. 29 B**). The treatment of the SW620 cells with 2.5 μ M of the free drug decreased the wound closure from $30 \pm 3\%$ of the control cells to $20 \pm 2\%$, confirming the capacity of galunisertib to downregulate the TGF- β signaling, inhibiting cell migration by 10%. A reduced migration was also observed when the SW620 cells were incubated with the empty encapsulated-DNPs (not loaded with galunisertib), which showed a migration of $20 \pm 4\%$ after 120 h. The decreased migration of the cells treated with the encapsulated-DNPs could be due to the presence of the nanocarrier bound on the cell surface and interacting with the antigen L1-CAM. Recent studies have shown that the L1-CAM has a binding site to several integrins (*i.e.*, $\alpha 5\beta 1$, $\alpha \nu\beta 1$, and $\alpha \nu\beta 3$) and triggers cell migration through an integrin-dependent pathway.^[165] The main integrin binding site was mapped in the sixth immunoglobulin (Ig) domain of the surface antigen. The inactivation of the integrin binding site on L1-CAM using antibodies or site-directed mutagenesis prevented the nuclear translocation of the L1-CAM signal, reducing cell-cell adhesion and migration.^[166] Hence, we suppose that the anchoring of the antibody-labeled DNPs to the L1-CAM on SW620 cells blocked the main integrin binding site, inhibiting their interaction with L1-CAM and consequent migration. This hypothesis is based on the evidence that L1-CAM and L1-CAM-binding integrins are often expressed by the same cell.^[138]

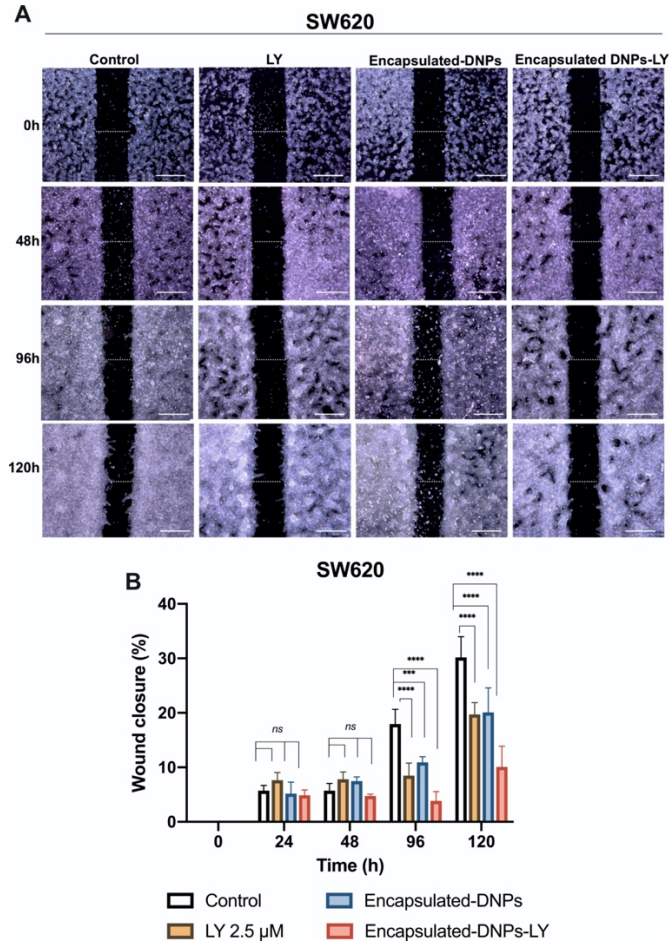


Figure 7. (A) Migration assay of SW620 cells. Migration of the cells incubated with DMEM 0.5% FBS (control), LY 2.5 μ M, encapsulated-DNPs 26 μ g mL⁻¹, and drug-loaded encapsulated-DNPs 26 μ g mL⁻¹ in DMEM 0.5% FBS for 120 h. Images of the wound closure were taken at 0, 24, 48, 96, and 120 h. The size of the closure at time t=0 is 500 μ m. The scale bars are 500 μ m. Images were acquired with a Leica Microscope and analyzed by the ImageJ software. (B) Results are reported as mean \pm standard deviation. The level of significance was set at probabilities of * $p < 0.05$, ** $p < 0.01$ and *** $p < 0.001$.

The inhibition of the migratory properties of SW620 was even stronger when encapsulated-DNPs were loaded with galunisertib. The cells treated with the drug-loaded encapsulated-DNPs showed a migration of $10 \pm 3\%$, which is 11% lower than the migration of cells treated with the free drug, demonstrating an enhanced effect of the delivered galunisertib (**Fig. 29 A-B**). The improved effect of galunisertib delivered by the encapsulated-DNPs in CRC was already validated in previous works, in which we reported a 3-fold increase of the gene downregulation by the delivered drug compared to the free molecule.^[29] Here, the increased therapeutic effect was provided by both the drug local release and blocking of L1-CAM on cell membrane. The binding of the NPs to the L1-CAM inhibited the interactions between integrins and the surface antigen, thus hindering the migration signaling. Therefore, the active-targeted approach not only improved the uptake of NPs in the targeted cell line but also inhibited the EMT process mediated by the engagement of integrins by the surface antigen. Overall, the synergistic effect of the drug and L1-CAM blocking produced a therapeutic outcome that was greater than the inhibition of migration induced by the free form of galunisertib.

4.4 Development of redox-responsive DNPs for on-demand intracellular release of an anticancer antisense peptide nucleic acid

This section describes the results reported in the following manuscript. The supporting information (SI) of the published paper can be accessed here: <https://doi.org/10.1002/smll.202204732>

M. Terracciano, F. Fontana, C. Tramontano, I. Rea, L. De Stefano, G. Oliviero, N. Borbone and H. A. Santos; Development of Surface Chemical Strategies for Synthesizing Redox-Responsive Diatomite Nanoparticles as a Green Platform for On-Demand Intracellular Release of an Antisense Peptide Nucleic Acid Anticancer Agent, *Small* 2022, 2204732.

4.4.1 Multistep chemical approach for the development of redox-responsive DNPs

The tumor microenvironment has unique physiological features, such as altered pH, hypoxia, increased redox potential, and enzymatic upregulation, which can be exploited to develop *stimuli*-responsive systems for localized drug release and reduced toxicity. Among these approaches, responsiveness to redox environments has emerged as an appealing trigger due to the four-fold increase in the concentration of the GSH in cancer microenvironment. The significant difference in the levels of GSH in tumor and health tissues can trigger the release and accumulation of the drug in the tumor, thus improving its therapeutic effect. To address the release of an antisense PNA inhibiting the PD-1/PD-L1 pathway in cancer cells, we developed redox-responsive PNA-loaded DNPs. PNA is a neutral-charged artificial oligonucleotide remarkably

similar to DNA and RNA but with unique resistance to enzymatic digestion, stability and excellent hybridization affinity.^[167]

To synthesize the redox-responsive DNPs with the highest surface functionalization yield, two different chemical approaches were explored. The former was based on a conventional multistep procedure that introduces the required reactive groups through chemical reactions until the desired NPs are obtained. The latter is, instead, a one-pot chemical strategy of surface functionalization. The precise quantification of available surface functional groups on the DNPs' surface is fundamental to adequately control the surface chemical processes, and, therefore the available functional groups were quantified by 1D solution-phase proton NMR, colorimetric assays, and DLS.

As extensively described, the DNPs were obtained by crushing, sonication and acid purification of raw diatomaceous earth powder and further silanized with APTES.^[52] The introduced $-NH_2$ groups allowed for the covalent conjugation of a 5000 Da PEG to APTES-modified DNPs, which provides DNPs with higher stability than 2000–500 Da PEG. High MW PEGs have longer side chains than lower MW PEGs, thus acting more effectively as steric stabilizers.^[168] The 1H NMR spectrum of APTES-modified DNPs (**Fig. 30 A**) shows the characteristic peaks of the protons of the aminopropyl chain from 0.60 to 2.90 ppm (peaks a–c), whereas the protons of ethoxy groups at 3.80 and 1.18 ppm were not detected, confirming the complete grafting of the APTES on the DNPs.^[169] Then, the number of APTES molecules on the NPs' surface was measured by quantitative NMR (qNMR). This technique is widely used for the quantification of small molecules in solution but it has been also explored

to quantify chemical moieties on modified NPs. The silanization yield of DNPs was quantified by integrating the peak area of ^1H spectrum of the NPs solution with the internal standard fumaric acid. The number of APTES grafted on the DNPs was measured to be $5.2 \pm 0.5 \mu\text{mol mg}^{-1}$ of NPs. Then, the free $-\text{NH}_2$ groups on the DNPs were confirmed and quantified by the ninhydrin assay.

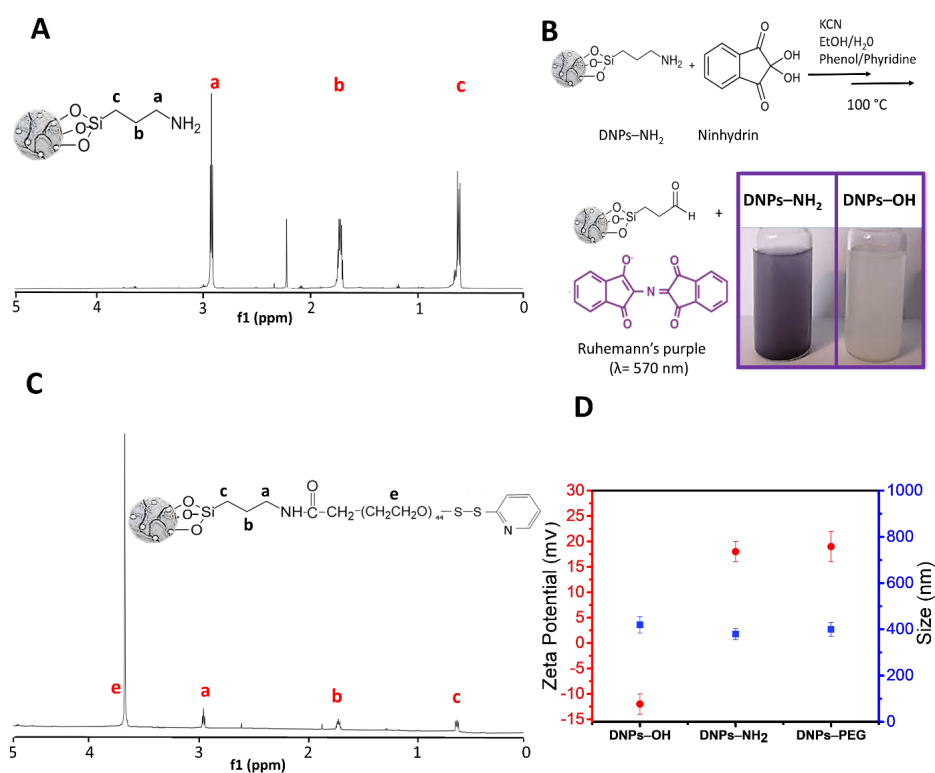


Figure 30. (A) ^1H NMR spectrum of APTES-modified DNPs (DNPs-NH₂). (B) Reaction of ninhydrin with DNPs-NH₂ followed by generation of Ruhemann purple product. (C) ^1H NMR spectrum of PEG-modified DNPs. (D) Size and ζ -potential of DNPs before and after the multi-step functionalization approach by DLS.

The reaction of primary -NH_2 with ninhydrin generated a colored product known as Ruhemann's purple (**Fig. 30 B**) that was measured spectrophotometrically at 570 nm. The amount of accessible -NH_2 on DNPs' surface was $0.20 \pm 0.06 \mu\text{mol mg}^{-1}$. Free APTES in the range from 0.06 to 5×10^{-3} M was used as internal calibration method. Finally, the PEGylation of the APTES-modified DNPs was performed by promoting a peptide bond between the NHS esters of the OPSS-PEG-NHS and the -NH_2 of the APTES-modified DNPs. The ^1H NMR spectrum of PEGylated DNPs showed a very weak signal of the large backbone $(\text{OCH}_2\text{CH}_2)_{44}$ from 3.6 to 3.7 ppm, suggesting a low functionalization yield. The qNMR analysis confirmed that only 0.002–0.005 $\mu\text{mol mg}^{-1}$ of PEG were bound to the NPs, corresponding to 1–2.5 % functionalization yield (**Fig. 30 C**). The silanization process caused a decrease in the DNPs' size from 420 ± 70 to 380 ± 50 nm due to an increase in the DNPs' surface repulsion forces passing from -12 ± 2 to 18 ± 2 mV (**Fig. 30 D**). However, no significant changes in size and surface charge were observed after PEGylation (400 ± 70 nm; 19 ± 2 mV), ruling out a successful NPs' modification (**Fig. 30 D**). The low functionalization yield obtained by the standard multistep functionalization strategy could be due to the APTES susceptibility to hydrolysis in aqueous solutions, high temperature, and sonication, leading to loss of *ca.* 10–60% of functional -NH_2 .^[170] Washings and sonication are mandatory procedures to remove adsorbed excess reagents from the NPs for maintaining *in vitro/ in vivo* safety of the material. However, due to the loss of functional -NH_2 groups and low yield of functionalization efficiency, the one-pot functionalization approach was preferred to the multistep method.

4.4.2 One-pot chemical strategy for the development of redox-responsive DNPs

The easy wet chemistry based on a one-pot strategy allows for the silanization and PEGylation of the DNPs through one step, preventing the loss of functional groups. This strategy included the synthesis of a complex of APTES–PEG that was further bound to the DNPs, avoiding intermediate purification steps that could impact the functionalization yield. The complex formation was monitored by ^1H NMR for up to 24 h and the obtained spectrum was compared to free APTES molecules. The formation of an amide bond between the $-\text{NH}_2$ of APTES and ester groups of the PEG was confirmed by the disappearing signal at 2.6 ppm and the shift of b from 1.47 to 1.58 ppm (**Fig. 31 A**). The presence of the ethoxy group protons at 1.2 (**Fig. 31 A-e**), which, instead, were no longer visible in **Fig. 30 A**, demonstrated that the one-pot strategy preserved APTES from hydrolysis and allowed for DNPs' silanization. After functionalizing the DNPs with the synthesized complex APTES-PEG (DNPs-PEG), the yield of the reaction was evaluated by qualitative and quantitative analysis. ^1H NMR spectrum of DNPs-PEG showed an intense signal of protons of the large PEG backbone $(\text{OCH}_2\text{CH}_2)_{44}$ from 3.7 to 3.9 ppm, confirming the successful PEGylation of DNPs with $6.5 \pm 1 \mu\text{mol mg}^{-1}$, corresponding to $\sim 80\%$ of functionalization yield (**Fig. 31 A**). The number of available $-\text{SH}$ groups on the DNPs-PEG was quantified by mixing the DNPs with 20×10^{-3} M dithiothreitol (DTT) to deprotect thiols from orthopyridyl disulfide (OPSS), and measuring the absorbance by a colorimetric assay. In this assay, $-\text{SH}$ groups reduced a disulfide-inhibited derivative of papain (papain– SSCH_3) releasing the active enzyme (papain– SH). The enzyme

cleaved the chromogenic papain substrate (L-BANPA) and released a yellow nitroaniline chromophore that was measured at 405 nm. The measured absorbance corresponded to an amount of PEG of 0.615 ± 0.065 $\mu\text{mol mg}^{-1}$ of the NPs. To evaluate the morphology of the developed NPs before and after functionalization, TEM images were acquired (**Fig. 31 B**). The analysis showed the typical irregular shape and porous morphology ($10 \text{ nm} < \text{pores diameter} < 50 \text{ nm}$) of the bare DNPs, highlighting a dense polymeric layer onto DNPs' external surface and inside the pores due to the PEGylation. The process resulted in an increase in the particles' size from 420 ± 70 to 480 ± 85 nm and a change of surface charge from 12 ± 2 mV to 20 ± 5 mV (**Fig. 31 C**).

Once assessed which was the functionalization strategy with the highest yield, the PNA sequence was conjugated to the DNPs-PEG by S–S bond between the –SH side chains of the cysteine (Cys) residues of the PNAs and the OPSS of PEG-modified DNPs. The selected PNA sequence targets the PD-1/PD-L1 axis, a well-known immunological checkpoint in the treatment of cancer. PD-1/PD-L1-targeting antibodies are already in clinical use but they are expensive and beneficial only for a small subset of patients.^[171] PNAs, instead, are nucleic acid mimics made of a polyamide backbone of repeating N-(2-aminoethyl)glycine units. PNAs preserve high affinity towards the target and remarkable stability, being far less expensive than antibodies. The antisense PNA was designed to bind to a specific region of the mRNA target, which was selected by computational tools.^[65] For the conjugation of the PNA to the PEG-DNPs, the PNAs were dispersed in DTT to avoid the formation of intramolecular S–S and then conjugated to the DNPs. The PNA conjugation increased the

surface charge of DNPs-PEG-PNA to 27 ± 3 mV due to the positive poly-Lys chains of the PNA (**Fig. 31 C**). Furthermore, the successful PNA-conjugation to the NPs surface was confirmed by absorbance spectroscopy due to the appearance of an absorbance peak at 260 nm in the UV-Vis spectrum of the DNPs-PNA (**Fig. 31 D**).

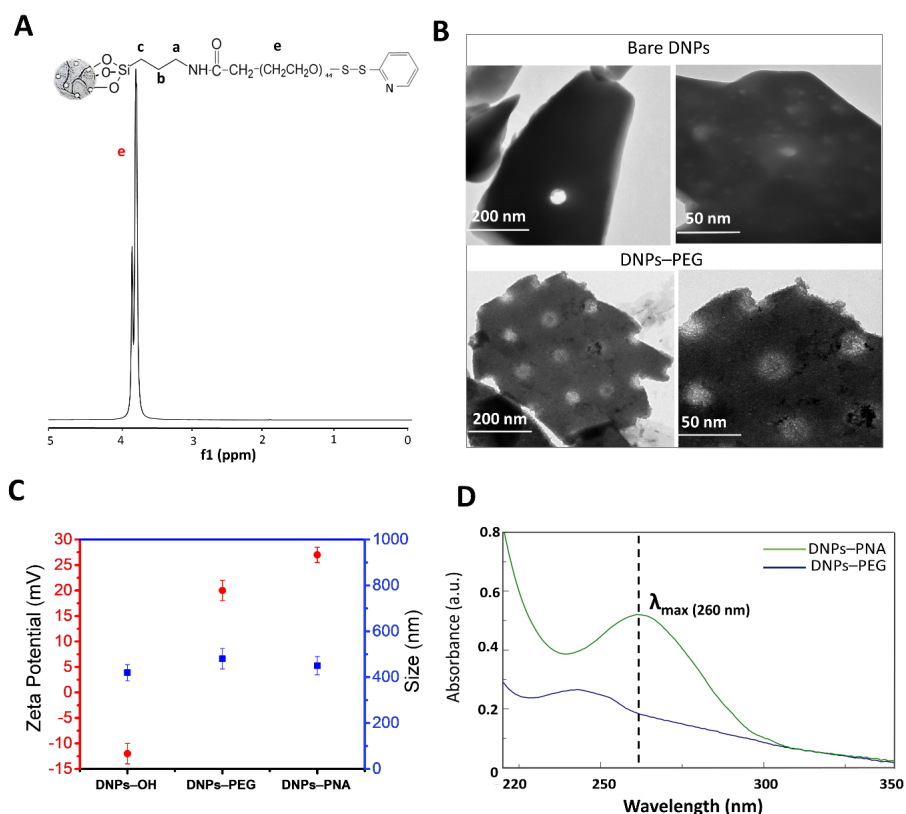


Figure 31. (A) ¹H NMR spectrum of one-pot functionalized DNPs-PEG. (B) TEM images of bare DNPs and DNPs-PEG and increasing zoom of DNPs' surface. (C) DNPs' size and ζ -potential before and after functionalization and PNA conjugation. (D) UV-Vis spectrum of DNPs before (DNPs-PEG) and after the bioconjugation (DNPs-PNA).

4.4.3 PNA loading and release and cell viability studies

Due to their peculiar porous nature and specific surface area of $23.6 \pm 0.1 \text{ m}^2 \text{ g}^{-1}$, DNPs are ideal for the loading of a wide range of molecules, including both small molecules and oligonucleotides. Since the disulfide bond onto modified-DNPs acts as a redox-responsive linkage, the release of the loaded FITC-labeled PNA (PNA*) from the DNPs was investigated and quantified after 48 h of treatment with 20 mM DTT by fluorescence spectroscopy. The loading capacity of the DNPs was $0.0485 \pm 0.004 \text{ } \mu\text{mol mg}^{-1}$ (corresponding to ~48 % and $306 \pm 25 \text{ } \mu\text{g}$ of PNA per mg of DNPs). When the DNPs-PNA were exposed to 100 mM DTT, no further PNA was released, suggesting that the maximum amount of drug was released by the DNPs-PNA. The release behavior of the redox-responsive DNPs was monitored under physiological conditions (PBS, pH 7.4), and in conditions mimicking the reducing tumor environment (PBS, 20 mM DTT, pH 5.5). The tumor environment is highly reducing and hypoxic, with the intracellular GSH concentration at least four-fold higher than normal cells. Therefore, the DTT was added to the release medium to mimic the composition of the cancer microenvironment. **Figure 32 A** shows that the DNPs-PNA treated with the reducing agent DTT released ~98% of PNA within a few minutes and a reaching a plateau after 24 h. On the contrary, the quantified PNA was ~4% in the absence of the DTT (CTR), showing that the disulfide bond breaking can be controlled by the increased concentration of GSH in cancer tissues. The obtained results confirmed that the nanosystem allows for on-demand PNA release in the tumor specifically.

To test the biocompatibility of the DNPs-PNA, their interaction with the main cellular constituents of blood (*i.e.*, red blood cells, RBCs) was investigated and the feasibility of therapeutic applications was evaluated. The hemolytic activity of the DNPs-PNA was based on the quantification of the lysed RBCs after cell exposure to 25, 50, 100, and 200 $\mu\text{g mL}^{-1}$ of DNPs-PNA for 1, 4, 24, and 48 h. The hemoglobin released from RBCs was quantified by UV-Vis at 577 nm and the amount (%) of hemolysis was calculated (Eq. 4). The number of lysed RBCs after 48 h of incubation at the maximum concentration of modified-DNPs (200 $\mu\text{g mL}^{-1}$) was 5 ± 2 % for the DNPs-PNA, confirming the biocompatibility of the developed redox-responsive DNPs. The hemolytic activity of the free PNA molecules (0.01 μmol) was 30 ± 5 %, whereas 200 $\mu\text{g mL}^{-1}$ DNP-PEG caused hemolysis of 8 ± 2.5 %. The reduced toxicity of DNPs-PNA compared to PNA demonstrated that its bioconjugation to the DNPs' surface reduced the hemotoxicity of PNA (**Fig. 32 B**). The PNA-induced hemotoxicity was due to the -SH groups of the Cys, which were introduced for the conjugation of PNA to the DNPs-PEG *via* S-S bond. In the bonded Cys-PNA, the -SH interacted with the membrane of the RBCs and activated the mechanisms leading to cell hemolysis. When the PNAs were bound to the DNPs-PEG by S-S, instead, the -SH groups were not available for interacting with the RBC membrane, and, therefore, the overall toxicity was reduced.

To further assess the safety of the developed NPs, we carried out cytotoxicity studies of MD-MBA 231 triple-negative breast cancer cells and A549 lung cancer cells exposed to different concentrations of the modified DNPs and PNA up to 72 h. The physiological state of the cells

incubated with the samples was compared with the negative control, represented by cells incubated with complete medium (10 % FBS RPMI or DMEM, respectively). The DNPs–PNA did not alter the cell viability of both the cell lines, even at high concentrations and longer incubation times, confirming the safety of the DNPs for PNA delivery (**Fig. 32 C-D**). The cytotoxicity of the DNPs-PEG (up to 200 $\mu\text{g mL}^{-1}$) and free PNAs (up to 0.01 μmol) after 72 h confirmed the biocompatibility of the DNPs-PEG and showed that cell defense mechanisms can contrast the PNA-induced toxicity, overcoming the irreversible toxicity of the free –SH observed in the RBCs (**Fig. 32 C-D**).

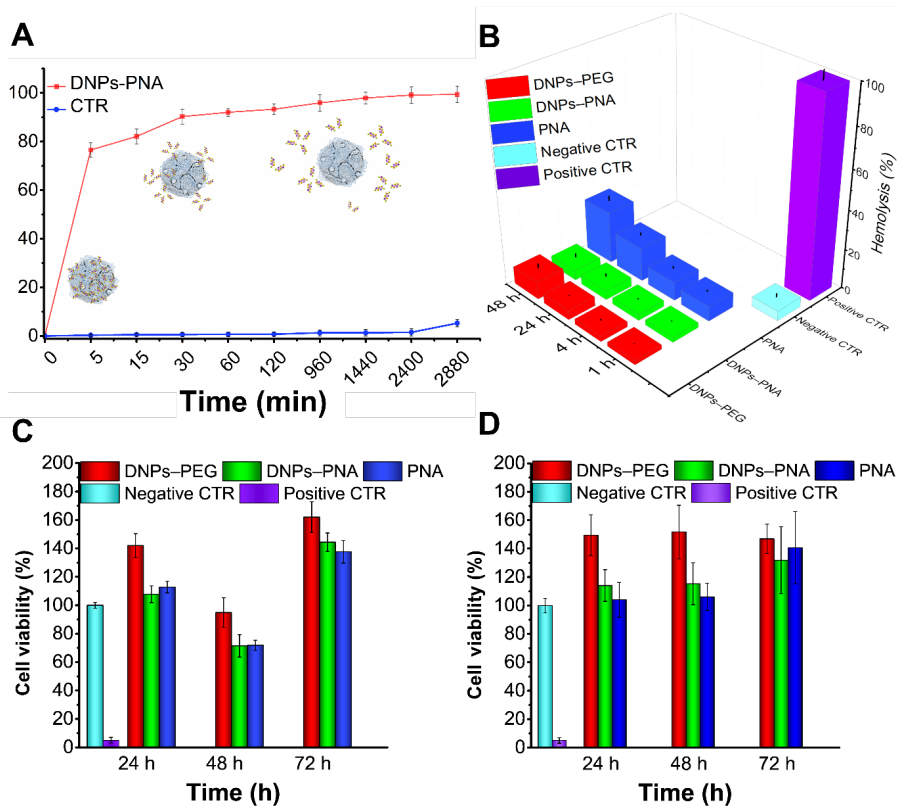


Figure 32. (A) Drug release profile of the DNP-PNA in DTT/PBS reducing solution and in PBS without DTT (CTR) at 37 °C. (B) Hemocompatibility of the modified-DNPs and free PNA estimated by spectrophotometric methods (577 nm). (C) Cell viability of MDA-MB-231 and (D) A549 cells after exposure to 200 μg mL⁻¹ modified-DNPs and 0.01 μmol PNA. Complete medium (10% FBS RPMI) and Triton X-100 (1%) were used as negative and positive controls, respectively. The data are presented as mean ± s.d. (n=3). Statistical analysis was made by one-way ANOVA comparing all data sets to the negative control. The level of significance was set at the probabilities of * $p \leq 0.05$, ** $p \leq 0.01$, and *** $p \leq 0.001$.

4.4.4 Cell uptake and activity studies of the developed DNPs-PNA

The cell uptake of the developed DNPs was investigated by flow cytometry at two different incubation times (6 and 12 h) to evaluate the internalization of the PNA released by DNPs-PNA and free PNA. A complete internalization of the DNPs-PNA was observed after 6 h of incubation in both cell lines, while free PNAs were internalized only after 12 h (**Fig. 33 A-B; Fig. 34 A-B**). The cell uptake of 50 $\mu\text{g mL}^{-1}$ DNPs-PNA* in both cancer cells was further investigated by confocal microscopy up to 24 h, confirming that the developed nanocarrier improved the internalization and intercellular accumulation of the PNA (**Fig. 33 C; Fig. 34 C**). Despite the PNA being synthesized with the poly-Lys chain, the positive groups did not improve its internalization, as shown by the little uptake of PNA in the cells. On the contrary, the DNPs-PNA improved the intracellular uptake of PNA, facilitating the cell membrane barrier crossing and accumulation.

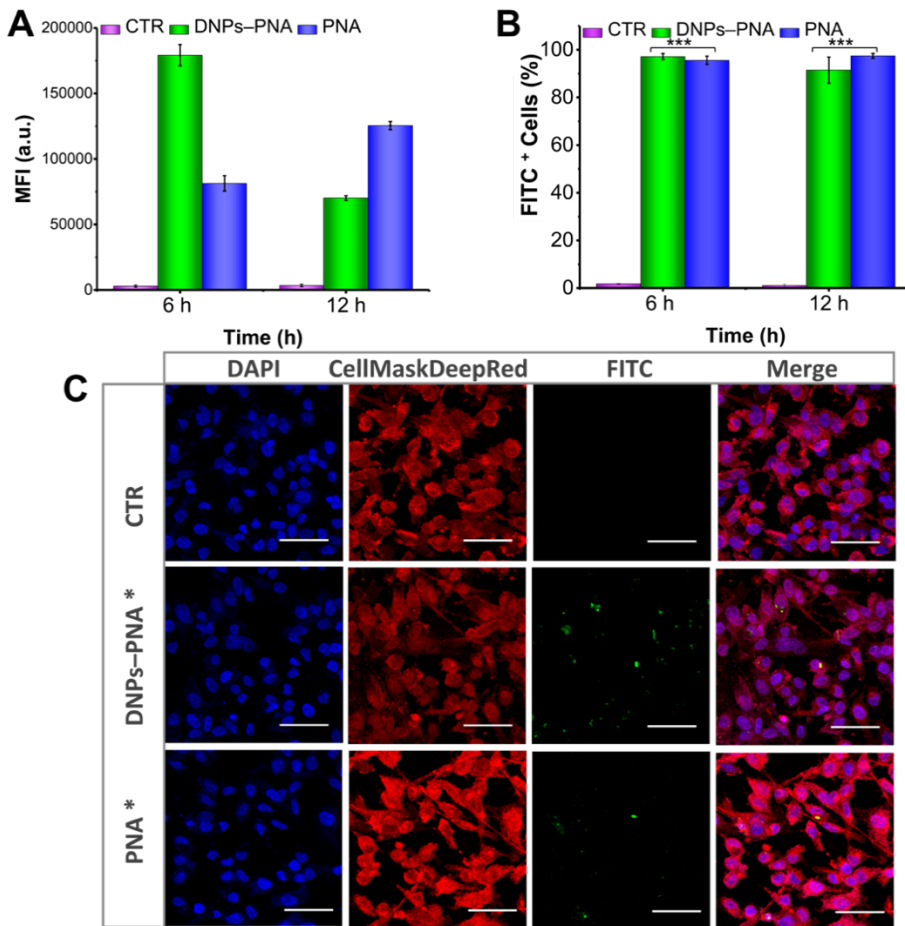


Figure 33. (A) Mean fluorescence Intensity (MFI) and (B) percentage of MDA-MB-231 incubated with DNP-PNA* ($50 \mu\text{g mL}^{-1}$) or free PNA* ($0.005 \mu\text{mol}$) for 6 or 12 h. The samples were then incubated with 0.005% Trypan Blue to quench the FITC fluorescence outside the cells. The data are presented as mean \pm s.d. ($n=3$) and were analyzed with one-way ANOVA. The level of significance from negative control was set at the probabilities of * $p \leq 0.05$ ** $p \leq 0.01$ and *** $p \leq 0.001$. (C) Confocal microscopy analysis of MDA-MB-231 cells incubated with DNPs-PNA* or PNA* for 24 h. The cell membranes were stained with Cell Mask

deep red, while nuclei were stained with DAPI. The images were acquired using a 63× objective.

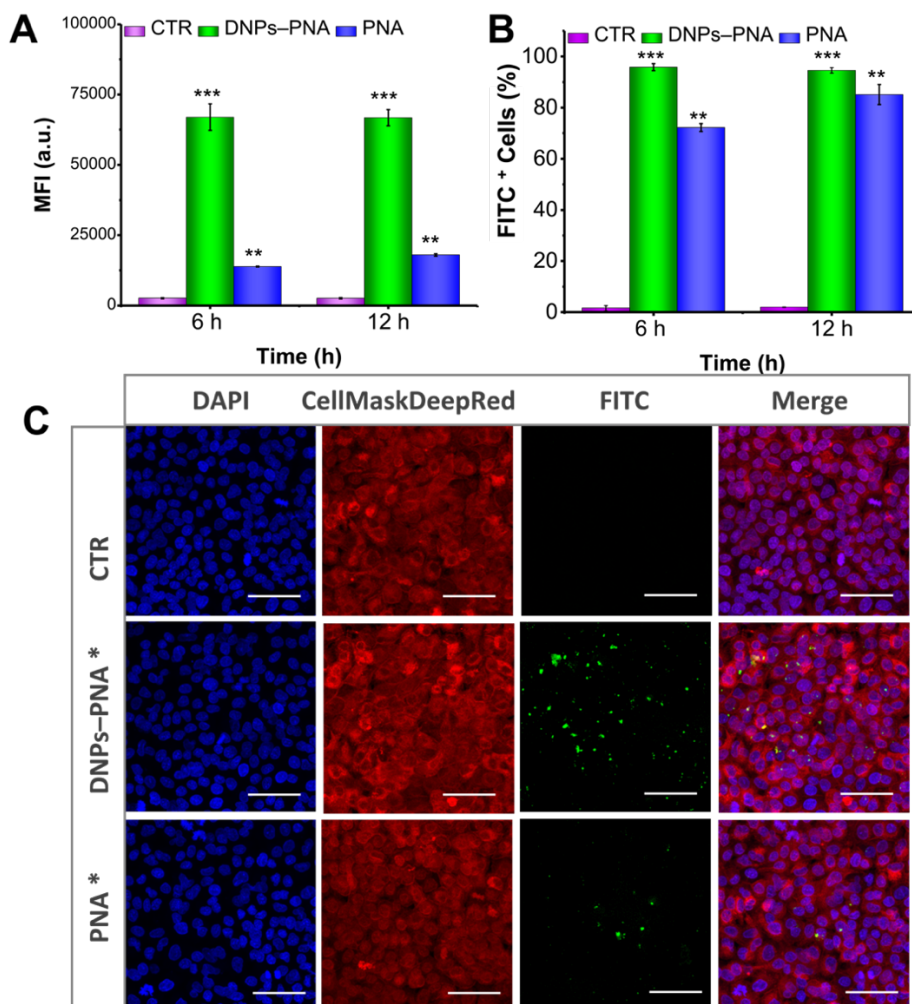


Figure 34. (A) MFI and (B) percentage of A549 incubated with DNPs–PNA* ($50 \mu\text{g mL}^{-1}$) or PNA* ($0.005 \mu\text{mol mL}^{-1}$) for 6 or 12 h. The samples were then incubated with 0.005% Trypan Blue to quench the FITC fluorescence outside the cells. The fluorescence was then analyzed by flow cytometry. The data are presented as mean \pm s.d. ($n=3$) and were analyzed

with one-way ANOVA. The level of significance from negative control was set at the probabilities of * $p \leq 0.05$ ** $p < 0.01$ and *** $p \leq 0.001$. (C) Confocal microscope images of A549 cells incubated with DNPs–PNA* or PNA* for 24 h. The cell membrane was stained with Cell Mask deep red, while the cell nuclei were stained with DAPI. The images were acquired using a 63× objective.

The ability of the developed DNPs-PNA of downregulating the PD-L1-mediated pathway was evaluated by flow cytometry quantifying the expression of PD-L1 upon cell incubation with 50 $\mu\text{g mL}^{-1}$ DNPs–PNA up to 72 h. The MD-MBA 231 and A549 lung cancer and U87 glioblastoma cells were chosen for their high expression of PD-L1.^[172] The downregulation of PD-L1 by the developed DNPs was observed only in MDA-MB-231 cells with a reduction of about 30 % after 72 h (**Fig. 35 A**), compared to *ca.* 90% of the control MDA-MB-231 cells. The treatment of A549 cells with the DNPs-PNA did not reduce the expression of PD-L1, which was reported to be between 40 and 60% before and after the treatment (**Fig. 35 B**). The U87 control cells exhibited a high expression of PD-L1 (between 70 and 90%), which was decreased by the treatment with the DNPs-PNA (**Fig. 35 C**). Importantly, the downregulation of PD-L1 on MDA-MB-231 was achieved by the DNPs-PNA, while the free oligonucleotide had any outcome. Furthermore, the DNPs-PNA carrying the scrambled (SC) PNA sequence (DNPs–PNA-SC) did not show any effect, confirming the specificity of the PNA sequence towards PD-L1. Despite the immune checkpoint blockade being an effective strategy for cancer treatment, the response to checkpoint blockade is not universal and varies significantly from tumor type, as demonstrated by the different

significance of the PDL-1 downregulation in cancer cells (**Fig. 35**). Therefore, many open questions need to be addressed in future research to support their emerging therapeutic approaches.

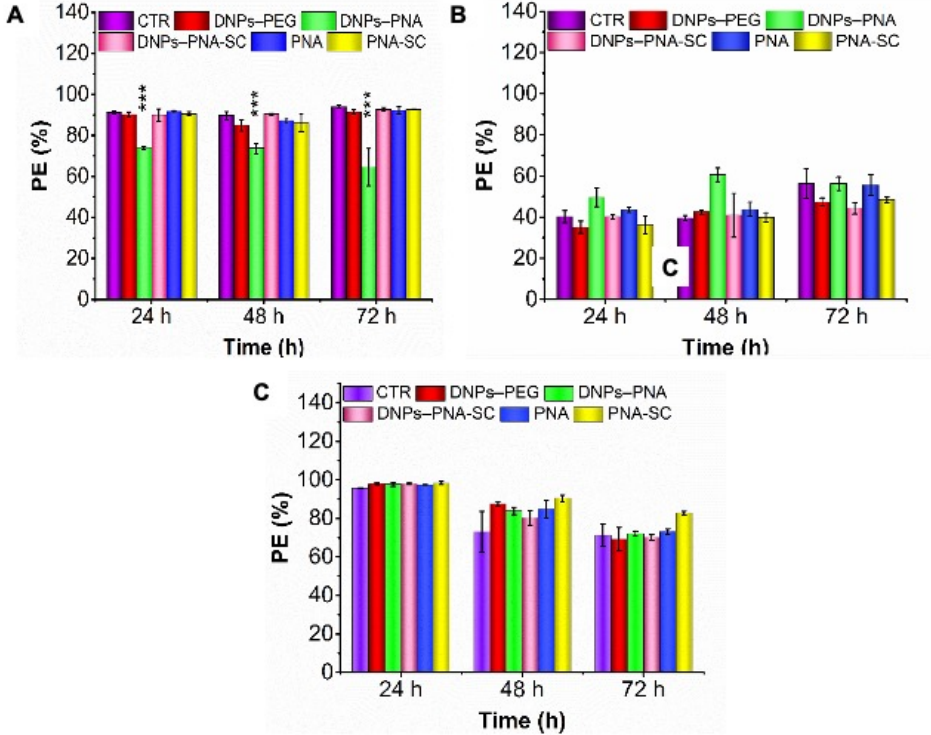


Figure 35. (A) percentage of PE⁺ MDA-MB-231 cells; (B) percentage of PE⁺ A549 cells; (C) percentage of PE⁺ U87 cells. All the cells were incubated with the modified DNPs and free PNAs for 24, 48, or 72 h and stained with PE anti-CD274 antibody. DNPs-PEG, DNPs-PNA, and DNPs-PNA-SC were added to the cells at a concentration of 50 $\mu\text{g mL}^{-1}$ in a complete medium, while PNA and PNA-SC were added at 0.005 $\mu\text{mol mL}^{-1}$. Data are presented as mean \pm s.d. ($n=3$). The statistical analysis was made by ANOVA comparing all data sets to the control represented by

cells incubated in a complete medium. The level of significance was set at the probabilities of $*p \leq 0.05$, $**p \leq 0.01$, and $***p \leq 0.001$.

5. Conclusions and future perspective

Nanomedicine is an ever-growing field bringing chemistry, engineering, physics, biology, and biotechnology together to overcome the shortcomings of conventional therapies. Over the years, nanomedicine has revolutionized the clinical landscape, with over 50 nanotechnology-based products already on the market, and an estimated 100 more under clinical trials. The use of NPs has opened up new avenues in the treatment of cancer, offering solutions to the limits of conventional chemotherapeutic drugs, such as unspecificity, systemic toxicity, and frequent administrations. The increasing number of publications and patents in the field demonstrates that both organic and inorganic NPs can load and deliver anti-cancer drugs in a controlled manner. The possibility to create advanced drug delivery systems holds the promise to provide cancer patients with a specific and non-invasive treatment, improving the efficacy of drugs and patients' quality of life. Among the inorganic NPs proposed for the treatment of cancer, diatomite nanoparticles (DNPs) secured their seat in the global race of nanomedicine, due to their natural porosity, biocompatibility, ease of production, and highly reactive surface chemistry. The porous structure of DNPs was shown to be able to load and release galunisertib in colon cancer cells with a release profile depending on the polymer coating. The cross-linked gelatin matrix improved the galunisertib loading capacity of the DNPs by up to 6% and provided them with a *stimuli*-responsive drug release in cancer cells. The combination of gold NPs (AuNPs) and DNPs allowed for the development of a hybrid

nanoplatfrom for the real-time monitoring and quantification of drug release in living cells. The enhancement of the Raman drug signal provided by the AuNPs enabled us to quantify the released drug with a sub-femtogram scale resolution and without under/overestimation caused by fluorescence issues. The in-situ synthesis of AuNPs on the DNPs was performed by using either polyethylene glycol or gelatin as a stabilizer, which promoted the formation of a stable complex DNP-AuNPs (or AuDNPs). The plasmonic nanosystem composed of DNPs and gelatin-stabilized AuNPs (AuDNPs) allowed for the design of a theoretical model to predict the thickness of the gelatin shell and correlate that to the DNPs' drug-loading capacity. The plasmonic features of the AuDNPs further enabled us to monitor gelatin formation, degradation and consequent drug release by absorbance measurements, thus overcoming the need of more sophisticated and expensive equipment. The ability of the galunisertib-loaded DNPs to block the mesenchymal to epithelial transition (MET) was demonstrated in the colorectal cancer (CRC) cells LS-174T, SW620, whereas any effect was observed in the non-metastatic cells Caco-2, and HT29-MTX, or normal colon cells CRL-1970. The delivered galunisertib increased the expression levels of epithelial genes, downregulating the metastatic pathway driven by the transforming growth factor- β receptor. The therapeutic outcome of the developed galunisertib nanocarrier was shown to be 2.5-fold stronger than the free drug, allowing for reducing the administered dose of the drug to revert the metastatic process in CRC. Furthermore, the expanding knowledge of DNPs' surface functionalization approaches allowed for the development of nanocarriers capable of targeting metastatic cells specifically and increasing the local

accumulation of galunisertib. The overexpression of L1-CAM on metastatic CRC cells was successfully exploited for the development of antibody-labeled DNPs-Gel delivering galunisertib to CRC cells with greater efficiency than the untargeted nanocarriers. The therapeutic outcome of the active-targeted formulation (DNPs-Gel-Ab) was tested both in monolayer and organoid-like structures of SW620 cells, confirming the potentiality of the DNPs for the treatment of metastatic CRC. The uptake of DNPs-Gel-Ab was studied in colon cancer cells expressing basal (Caco-2 and HT29-MTX) or high levels of L1-CAM (SW620). The antibody-antigen interactions increased the uptake of the DNPs-Gel-Ab in the SW620 cells by 13% compared to Caco-2 and HT29-MTX, outlining the possibility to increase the specificity of NPs' uptake and drug accumulation in the tumor site. Overall, the proposed DNPs were tested in both cancer and healthy cell lines at a concentration of up to 200 $\mu\text{g mL}^{-1}$ and for up to 72 h, confirming their safety and ability to penetrate cancer cells.

The formulation described herein showed an average size of 400 nm, which makes DNPs suitable for oral administration but not suitable for intravenous injection. For this reason, herein, we proposed a microfluidic approach for the production of gastro-resistant galunisertib-loaded DNPs for oral administration and drug accumulation in the colon. The microfluidic encapsulation of DNPs-Gel-Ab in the enteric coating hydroxypropyl methylcellulose allowed for the production of nanocarriers with improved size distribution and gastro-resistant features. The controlled flow rates of reagents in the micrometer channels favored the production of encapsulated-DNPs with a batch-to-batch reproducibility

and stability higher than by bulk mixing approaches. The enteric coating protected gelatin from degradation in the stomach and provided the nanocarrier with the capability of releasing galunisertib at the lower intestine pH.

Moreover, the overexpression of glutathione (GSH) in the tumor microenvironment was successfully exploited for the development of redox-responsive DNPs carrying an anti-cancer peptide nucleic acid (PNA). The conjugation of PNA to DNPs (DNPs-PNA) by disulfide bond was shown to be a valid alternative to common loading strategies and, above all, allowed for an on-demand drug release triggered by the excess of GSH in cancer cells. The capability of DNPs-PNA to deliver the drug inside cancer cells and increase the uptake of the PNA was further demonstrated in MD-MBA 231 triple-negative breast and A549 lung cancer cells.

The different loading strategies, functionalization approaches, and polymer coatings described throughout this work demonstrated that DNPs can be engineered for targeting cancer cells and releasing anti-cancer agents with tumor environment-triggered profiles. The *in vitro* results obtained with different cell lines shed a light on the potentiality of DNP-based nanocarriers for other drugs or drug combinations' delivery, and consequently, for a variety of other therapeutic purposes. Nonetheless, *in vivo* studies will be crucial to determine the success of the developed DNPs in a living organism, investigate their distribution within the body, and evaluate accumulation in crucial organs. For the therapeutic evaluation of the galunisertib-loaded DNPs, we considered injecting the CRC cell line SW620 in mice to produce multiple metastatic lesions within the body and

mimic the metastatic outbreak of CRC. Animal testing of galunisertib-loaded DNPs is under investigation in our group and the results concerning the efficacy of the formulation *in vivo* are yet to come in the next months. In conclusion, the present thesis provides new insights into the study of cancer-targeted nanomedicine approaches. The advanced DNPs described herein showed great potential as multifunctional platforms for efficient drug delivery and monitoring in cancer cells, while fostering the discussion on the emerging opportunities to improve the treatments of cancer.

Funding and grants

C.T. acknowledges UniNa and Compagnia San Paolo for the financial sponsorship in the frame of a joint project called STAR Plus 2020.

References

- [1] K. E. Drexler, *Bulletin of Science, Technology & Society* **2004**, 24, 21.
- [2] K. Riehemann, S. W. Schneider, T. A. Luger, B. Godin, M. Ferrari, H. Fuchs, *Angew. Chem. Int. Ed.* **2009**, 48, 872.
- [3] S. Soares, J. Sousa, A. Pais, C. Vitorino, *Front. Chem.* **2018**, 6, 360.
- [4] M. Germain, F. Caputo, S. Metcalfe, G. Tosi, K. Spring, A. K. O. Åslund, A. Pottier, R. Schiffelers, A. Ceccaldi, R. Schmid, *Journal of Controlled Release* **2020**, 326, 164.
- [5] S. Chen, Q. Zhang, Y. Hou, J. Zhang, X.-J. Liang, **2013**, 5, 61.
- [6] B. Flühmann, I. Ntai, G. Borchard, S. Simoens, S. Mühlebach, *European Journal of Pharmaceutical Sciences* **2019**, 128, 73.
- [7] F. Man, T. Lammers, R. T. M. de Rosales, *Molecular Imaging and Biology* **2018**, 20, 683.
- [8] Eric Lagally, *Microfluidics and Nanotechnology: Biosensing to the Single Molecule Limit*, 1st ed., Eric Lagally, Boca Raton, **2017**.
- [9] S. S. Suri, H. Fenniri, B. Singh, *Journal of Occupational Medicine and Toxicology* **2007**, 2, 16.
- [10] Y. Dang, J. Guan, *Smart Materials in Medicine* **2020**, 1, 10.
- [11] J. K. Patra, G. Das, L. F. Fraceto, E. V. R. Campos, M. del P.

- Rodriguez-Torres, L. S. Acosta-Torres, L. A. Diaz-Torres, R. Grillo, M. K. Swamy, S. Sharma, S. Habtemariam, H.-S. Shin, *Journal of Nanobiotechnology* **2018**, *16*, 71.
- [12] T. C. Jackson, B. O. Patani, D. E. Ekpa, *ANP* **2017**, *06*, 93.
- [13] P. Moskal, E. Ł. Stępień, **2021**, *17*, 199.
- [14] J. A. Hubbell, A. Chilkoti, **2012**, 337, 4.
- [15] R. Bosetti, S. L. Jones, *Nanomedicine* **2019**, *14*, 1367.
- [16] M. Holzinger, A. Le Goff, S. Cosnier, *Front. Chem.* **2014**, *2*.
- [17] I. S. Kucherenko, O. O. Soldatkin, D. Yu. Kucherenko, O. V. Soldatkina, S. V. Dzyadevych, *Nanoscale Adv.* **2019**, *1*, 4560.
- [18] A. I. Barbosa, R. Rebelo, R. L. Reis, M. Bhattacharya, V. M. Correlo, *MEDICAL DEVICES & SENSORS* **2021**, *4*, e10156.
- [19] V. Nocerino, B. Miranda, C. Tramontano, G. Chianese, P. Dardano, I. Rea, L. De Stefano, *Chemosensors* **2022**, *10*, 150.
- [20] N. Strambeanu, L. Demetrovici, D. Dragos, M. Lungu, In *Nanoparticles' Promises and Risks* (Eds.: Lungu, M.; Neculae, A.; Bunoiu, M.; Biris, C.), Springer International Publishing, Cham, **2015**, pp. 3–8.
- [21] I. Khan, K. Saeed, I. Khan, *Arabian Journal of Chemistry* **2019**, *12*, 908.
- [22] M. J. Mitchell, M. M. Billingsley, R. M. Haley, M. E. Wechsler, N. A. Peppas, R. Langer, *Nat Rev Drug Discov* **2021**, *20*, 101.
- [23] D. C. Ferreira Soares, S. C. Domingues, D. B. Viana, M. L. Tebaldi, *Biomedicine & Pharmacotherapy* **2020**, *131*, 110695.
- [24] A. C. Anselmo, S. Mitragotri, *Bioengineering & Translational Medicine* **2021**, *6*, e10246.
- [25] A. Alsuraifi, A. Curtis, D. Lamprou, C. Hoskins, *Pharmaceutics* **2018**, *10*, 136.
- [26] S. E. Krown, D. W. Northfelt, D. Osoba, J. S. Stewart, *Seminars in Oncology* **2004**, *31*, 36.
- [27] R. Tenchov, R. Bird, A. E. Curtze, Q. Zhou, *ACS Nano* **2021**, *15*, 16982.
- [28] C. J. Batty, E. M. Bachelder, K. M. Ainslie, *Trends in Molecular Medicine* **2021**, *27*, 516.
- [29] S. Managò, C. Tramontano, D. Delle Cave, G. Chianese, G. Zito, L. De Stefano, M. Terracciano, E. Lonardo, A. C. De Luca, I. Rea, *Small* **2021**, *17*, 2101711.
- [30] J. Conde, J. T. Dias, V. Graça, M. Moros, P. V. Baptista, J. M. de la Fuente, *Front. Chem.* **2014**, *2*.

- [31] L. T. Canham, D. Ferguson, In *Handbook of Porous Silicon* (Ed.: Canham, L.), Springer International Publishing, Cham, **2021**, pp. 1–7.
- [32] S. Bayda, M. Hadla, S. Palazzolo, P. Riello, G. Corona, G. Toffoli, F. Rizzolio, *Current Medicinal Chemistry* **2018**, *25*, 4269.
- [33] A. C. Anselmo, S. Mitragotri, *The AAPS Journal* **2015**, *17*, 1041.
- [34] L. R. Hirsch, R. J. Stafford, J. A. Bankson, S. R. Sershen, B. Rivera, R. E. Price, J. D. Hazle, N. J. Halas, J. L. West, *Proceedings of the National Academy of Sciences* **2003**, *100*, 13549.
- [35] I. Rea, P. Dardano, R. Moretta, C. Schiattarella, M. Terracciano, M. Casalino, M. Gioffrè, T. Crisci, G. Chianese, C. Tramontano, N. Borbone, L. De Stefano, In *Sensors and Microsystems* (Eds.: Di Francia, G.; Di Natale, C.), Springer International Publishing, Cham, **2021**, pp. 93–99.
- [36] C. He, J. Lu, W. Lin, *Journal of Controlled Release* **2015**, *219*, 224.
- [37] M. Manzano, M. Vallet-Regí, *Adv. Funct. Mater.* **2020**, *30*, 1902634.
- [38] S. Jafari, H. Derakhshankhah, L. Alaei, A. Fattahi, B. S. Varnamkhasti, A. A. Saboury, *Biomedicine & Pharmacotherapy* **2019**, *109*, 1100.
- [39] Y. Zhou, G. Quan, Q. Wu, X. Zhang, B. Niu, B. Wu, Y. Huang, X. Pan, C. Wu, *Acta Pharmaceutica Sinica B* **2018**, *8*, 165.
- [40] F. Farjadian, A. Roointan, S. Mohammadi-Samani, M. Hosseini, *Chemical Engineering Journal* **2019**, *359*, 684.
- [41] X. Pang, F. Tang, *Microporous and Mesoporous Materials* **2005**, *85*, 1.
- [42] L. Ernawati, T. Ogi, R. Balgis, K. Okuyama, M. Stucki, S. C. Hess, W. J. Stark, *Langmuir* **2016**, *32*, 338.
- [43] H. Nakashima, K. Omae, T. Takebayashi, C. Ishizuka, T. Uemura, *Jrnl of Occup Health* **1998**, *40*, 270.
- [44] N. Rabiee, M. Khatami, G. Jamalipour Soufi, Y. Fatahi, S. Irvani, R. S. Varma, *ACS Biomater. Sci. Eng.* **2021**, *7*, 3053.
- [45] C. Tramontano, G. Chianese, M. Terracciano, L. de Stefano, I. Rea, *Applied Sciences* **2020**, *10*, 6811.
- [46] S. Cicco, D. Vona, R. Gristina, E. Sardella, R. Ragni, M. Lo Presti, G. Farinola, *Bioengineering* **2016**, *3*, 35.
- [47] N. Sharma, D. P. Simon, A. M. Diaz-Garza, E. Fantino, A. Messaabi, F. Meddeb-Mouelhi, H. Germain, I. Desgagné-Penix, *Front. Mar. Sci.* **2021**, *8*, 636613.

- [48] L. M. Jurkić, I. Capanec, S. K. Pavelić, K. Pavelić, *Nutrition & Metabolism* **2013**, *10*, 2.
- [49] J. Delasoie, F. Zobi, *Pharmaceutics* **2019**, *11*, 537.
- [50] I. Rea, M. Terracciano, S. Chandrasekaran, N. H. Voelcker, P. Dardano, N. M. Martucci, A. Lamberti, L. De Stefano, *Nanoscale Research Letters* **2016**, *11*, 405.
- [51] S. Maher, M. Alsawat, T. Kumeria, D. Fathalla, G. Fetih, A. Santos, F. Habib, D. Losic, *Adv. Funct. Mater.* **2015**, *25*, 5107.
- [52] C. Tramontano, L. De Stefano, M. Terracciano, G. Chianese, I. Rea, In *Algal Biotechnology* (Eds.: Ahmad, A.; Banat, F.; Taher, H.), Elsevier, **2022**, pp. 427–446.
- [53] D. Losic, *Diatom Nanotechnology*, The Royal Society of Chemistry, **2018**, p. 270.
- [54] A. Ahmad, F. Banat, H. Taher, *Algal biotechnology: integrated algal engineering for bioenergy, bioremediation, and biomedical applications*, **2022**.
- [55] M. Terracciano, M. Napolitano, L. D. Stefano, A. C. D. Luca, I. Rea, *Nanotechnology* **2018**, *29*, 235601.
- [56] T. Chen, F. Wu, Y. Li, H. E. Rozan, X. Chen, C. Feng, *Front. Bioeng. Biotechnol.* **2022**, *10*, 894636.
- [57] E. De Tommasi, A. C. De Luca, *Biomed. Opt. Express* **2022**, *13*, 3080.
- [58] J. Delasoie, P. Schiel, S. Vojnovic, J. Nikodinovic-Runic, F. Zobi, *Photoactivatable Surface-Functionalized Diatom Microalgae for Colorectal Cancer Targeted Delivery and Enhanced Cytotoxicity of Anticancer Complexes*, **2020**.
- [59] I. Rea, N. M. Martucci, L. D. Stefano, I. Ruggiero, M. Terracciano, P. Dardano, N. Migliaccio, P. Arcari, R. Taté, I. Rendina, A. Lamberti, *Biochimica et Biophysica Acta (BBA) - General Subjects* **2014**, *1840*, 3393.
- [60] S. Managò, N. Migliaccio, M. Terracciano, M. Napolitano, N. M. Martucci, L. De Stefano, I. Rendina, A. C. De Luca, A. Lamberti, I. Rea, *J. Biophotonics* **2018**, *11*, e201700207.
- [61] C. Tramontano, B. Miranda, G. Chianese, L. De Stefano, C. Forestiere, M. Pirozzi, I. Rea, *IJMS* **2021**, *22*, 10755.
- [62] I. Ruggiero, M. Terracciano, N. M. Martucci, L. De Stefano, N. Migliaccio, R. Tatè, I. Rendina, P. Arcari, A. Lamberti, I. Rea, *Nanoscale Research Letters* **2014**, *9*, 329.
- [63] N. Bouazizi, J. Vieillard, R. Bargougui, N. Couvrat, O. Thoumire,

- S. Morin, G. Ladam, N. Mofaddel, N. Brun, A. Azzouz, F. Le Derf, *Journal of Alloys and Compounds* **2019**, 771, 1090.
- [64] M. Terracciano, M.-A. Shahbazi, A. Correia, I. Rea, A. Lamberti, L. De Stefano, H. A. Santos, *Nanoscale* **2015**, 7, 20063.
- [65] M. Terracciano, F. Fontana, A. P. Falanga, S. D'Errico, G. Torrieri, F. Greco, C. Tramontano, I. Rea, G. Piccialli, L. De Stefano, G. Oliviero, H. A. Santos, N. Borbone, *Small* **2022**, n/a, 2204732.
- [66] H. Goodman, G. S. Banker, *Journal of Pharmaceutical Sciences* **1970**, 59, 1131.
- [67] J. Delasoie, J. Rossier, L. Haeni, B. Rothen-Rutishauser, F. Zobi, *Dalton Trans.* **2018**, 47, 17221.
- [68] E. Dekker, P. J. Tanis, J. L. A. Vleugels, P. M. Kasi, M. B. Wallace, *The Lancet* **2019**, 394, 1467.
- [69] F. Di Nicolantonio, P. P. Vitiello, S. Marsoni, S. Siena, J. Tabernero, L. Trusolino, R. Bernards, A. Bardelli, *Nature Reviews Clinical Oncology* **2021**, 18, 506.
- [70] Y. Itatani, K. Kawada, Y. Sakai, *Int. J. Mol. Sci.* **2019**, 16.
- [71] Y. Xu, B. Pasche, *Human Molecular Genetics* **2007**, 16, R14.
- [72] C. De Pascalis, S. Etienne-Manneville, *MBoC* **2017**, 28, 1833.
- [73] E. E. Er, M. Valiente, K. Ganesh, Y. Zou, S. Agrawal, J. Hu, B. Griscom, M. Rosenblum, A. Boire, E. Brogi, F. G. Giancotti, M. Schachner, S. Malladi, J. Massagué, *Nat Cell Biol* **2018**, 20, 966.
- [74] K. Ganesh, H. Basnet, Y. Kaygusuz, A. M. Laughney, L. He, R. Sharma, K. P. O'Rourke, V. P. Reuter, Y.-H. Huang, M. Turkekul, E. E. Er, I. Masilionis, K. Manova-Todorova, M. R. Weiser, L. B. Saltz, J. Garcia-Aguilar, R. Koche, S. W. Lowe, D. Pe'er, J. Shia, J. Massagué, *Nat Cancer* **2020**, 1, 28.
- [75] H. Schäfer, B. Struck, E.-M. Feldmann, F. Bergmann, E. Grage-Griebenow, C. Geismann, S. Ehlers, P. Altevogt, S. Sebens, *Oncogene* **2013**, 32, 180.
- [76] D. D. Cave, X. Hernando-Momblona, M. Sevillano, G. Minchiotti, E. Lonardo, *Theranostics* **2021**, 11, 5686.
- [77] A. Calon, E. Espinet, S. Palomo-Ponce, D. V. F. Tauriello, M. Iglesias, M. V. Céspedes, M. Sevillano, C. Nadal, P. Jung, X. H.-F. Zhang, D. Byrom, A. Riera, D. Rossell, R. Mangués, J. Massagué, E. Sancho, E. Batlle, *Cancer Cell* **2012**, 22, 571.
- [78] A. T. Malik, J. H. Alexander, J. L. Mayerson, S. N. Khan, T. J. Scharschmidt, *Clinical Orthopaedics and Related Research®* **2020**, 478.
- [79] A. Tiwari, S. Saraf, A. Verma, P. K. Panda, S. K. Jain, *World J*

Gastroenterol **2018**, *24*, 4428.

- [80] D. R. Rivas, M. V. C. Dela Cerna, C. N. Smith, S. Sampathi, B. G. Patty, D. Lee, J. S. Blackburn, *Sci Rep* **2021**, *11*, 10302.
- [81] B. Rani, A. Malfettone, F. Dituri, J. Soukupova, L. Lupo, S. Mancarella, I. Fabregat, G. Giannelli, *Cell Death & Disease* **2018**, *9*, 373.
- [82] A. de Gramont, S. Faivre, E. Raymond, *null* **2017**, *6*, e1257453.
- [83] J. Chen, Z. Ding, S. Li, S. Liu, C. Xiao, Z. Li, B. Zhang, X. Chen, X. Yang, *Theranostics* **2021**, *11*, 1345.
- [84] M.-J. Goumans, Z. Liu, P. ten Dijke, *Cell Research* **2009**, *19*, 116.
- [85] G. Yan, M. Dai, C. Zhang, S. Poulet, A. Moamer, N. Wang, J. Boudreault, S. Ali, J.-J. Lebrun, *Oncogenesis* **2021**, *10*, 21.
- [86] D. Melisi, D.-Y. Oh, A. Hollebecque, E. Calvo, A. Varghese, E. Borazanci, T. Macarulla, V. Merz, C. Zecchetto, Y. Zhao, I. Gueorguieva, M. Man, L. Gandhi, S. T. Estrem, K. A. Benhadji, M. C. Lanasa, E. Avsar, S. C. Guba, R. Garcia-Carbonero, *J Immunother Cancer* **2021**, *9*, e002068.
- [87] K. C. Cassidy, I. Gueorguieva, C. Miles, J. Rehmel, P. Yi, W. J. Ehlhardt, *Xenobiotica* **2018**, *48*, 382.
- [88] R. B. Mokhtari, T. S. Homayouni, N. Baluch, E. Morgatskaya, S. Kumar, B. Das, H. Yeger, *Oncotarget; Vol 8, No 23* **2017**.
- [89] Y. Nilssen, O. T. Brustugun, M. T. Eriksen, M. G. Guren, E. S. Haug, B. Naume, E. Schlichting, B. Møller, *BMC Cancer* **2022**, *22*, 220.
- [90] S. Shen, Y. Wu, Y. Liu, D. Wu, *IJN* **2017**, *Volume 12*, 4085.
- [91] N. Kamaly, B. Yameen, J. Wu, O. C. Farokhzad, *Chem. Rev.* **2016**, *116*, 2602.
- [92] D. Yang, W. Chen, J. Hu, *J. Phys. Chem. B* **2014**, *118*, 12311.
- [93] Z. Ji, H. Liu, L. Yu, Q. Duan, Y. Chen, L. Chen, *Food Hydrocolloids* **2020**, *104*, 105733.
- [94] J. P. Martins, G. Torrieri, H. A. Santos, *Expert Opinion on Drug Delivery* **2018**, *15*, 469.
- [95] M. H. Shoaib, R. I. Yousuf, F. R. Ahmed, F. R. Ali, F. Qazi, K. Ahmed, F. Zafar, In *Polymer Coatings*, **2020**, pp. 275–317.
- [96] D. T. Friesen, R. Shanker, M. Crew, D. T. Smithey, W. J. Curatolo, J. A. S. Nightingale, *Mol. Pharmaceutics* **2008**, *5*, 1003.
- [97] A. COURTS, *Biochem J* **1955**, *59*, 382.
- [98] S. Wang, Y. Song, K. Cao, L. Zhang, X. Fang, F. Chen, S. Feng, F. Yan, *Acta Biomaterialia* **2021**, *134*, 621.
- [99] M. Santoro, A. M. Tataru, A. G. Mikos, *Journal of Controlled Release* **2014**, *190*, 210.

- [100] S. Lu, X. Fan, H. Wang, Y. Zhao, W. Zhao, M. Li, R. Lv, T. Wang, T. Sun, *ACS Appl. Bio Mater.* **2020**, *3*, 3518.
- [101] N. Shafagh, *J Polym Res* **2018**, *8*.
- [102] F. Danişman-Kalındemirtaş, İ. A. Kariper, G. Erdemir, E. Sert, S. Erdem-Kuruca, *Scientific Reports* **2022**, *12*, 10686.
- [103] E. Boedtkjer, S. F. Pedersen, **2020**, 27.
- [104] F. A. Osorio, E. Bilbao, R. Bustos, F. Alvarez, *null* **2007**, *10*, 841.
- [105] E. Ugarte-Berzal, J. Vandooren, E. Bailón, G. Opdenakker, A. García-Pardo, *Journal of Biological Chemistry* **2016**, *291*, 11751.
- [106] M. Quintanilla, 37.
- [107] M. Mahmoudi Saber, *Colloids and Surfaces B: Biointerfaces* **2019**, *183*, 110407.
- [108] F. M. Brodsky, *Pharmaceutical Research* **1988**, *5*, 1.
- [109] F. Schulz, D. Lutz, N. Rusche, N. G. Bastús, M. Stieben, M. Höltig, F. Grüner, H. Weller, M. Schachner, T. Vossmeier, G. Loers, *Nanoscale* **2013**, *5*, 10605.
- [110] S.-Y. Sung, I.-H. Wu, P.-H. Chuang, J. A. Petros, H.-C. Wu, H.-J. Zeng, W.-C. Huang, L. W. K. Chung, C.-L. Hsieh, *Oncotarget; Vol 5, No 20* **2014**.
- [111] W. Choe, T. A. Durgannavar, S. J. Chung, *Materials (Basel)* **2016**, *9*, 994.
- [112] A. K. Pearce, R. K. O'Reilly, *Bioconjugate Chem.* **2019**, *30*, 2300.
- [113] M. M. Al-Tabakha, *J Pharm Pharm Sci* **2010**, *13*, 428.
- [114] J. Siepmann, N. A. Peppas, *Advanced Drug Delivery Reviews* **2001**, *48*, 139.
- [115] J. P. Martins, D. Liu, F. Fontana, M. P. A. Ferreira, A. Correia, S. Valentino, M. Kemell, K. Moslova, E. Mäkilä, J. Salonen, J. Hirvonen, B. Sarmiento, H. A. Santos, *ACS Appl. Mater. Interfaces* **2018**, *10*, 44354.
- [116] C. Costa, Z. Liu, J. P. Martins, A. Correia, P. Figueiredo, A. Rahikkala, W. Li, J. Seitsonen, J. Ruokolainen, S.-P. Hirvonen, A. Aguiar-Ricardo, M. L. Corvo, H. A. Santos, *Biomater. Sci.* **2020**, *8*, 3270.
- [117] F. Araújo, N. Shrestha, M.-A. Shahbazi, D. Liu, B. Herranz-Blanco, E. M. Mäkilä, J. J. Salonen, J. T. Hirvonen, P. L. Granja, B. Sarmiento, H. A. Santos, *ACS Nano* **2015**, *9*, 8291.
- [118] W. Li, D. Liu, H. Zhang, A. Correia, E. Mäkilä, J. Salonen, J. Hirvonen, H. A. Santos, *Acta Biomaterialia* **2017**, *48*, 238.
- [119] D. Chenthamara, S. Subramaniam, S. G. Ramakrishnan, S. Krishnaswamy, M. M. Essa, F.-H. Lin, M. W. Qoronfleh, *Biomaterials*

- Research* **2019**, *23*, 20.
- [120] Y. Wei, L. Zhao, *null* **2014**, *19*, 129.
- [121] H. Cheng, S. Huang, G. Huang, *J Enzyme Inhib Med Chem* **2019**, *34*, 1590.
- [122] C. Tramontano, J. P. Martins, L. De Stefano, M. Kemell, A. Correia, M. Terracciano, N. Borbone, I. Rea, H. A. Santos, *Adv Healthcare Materials* **2022**, 2202672.
- [123] C.-B. Gaucher ArianeAU-Bonetti, JustineAU-Clarot, IgorAU-Leroy, PierreAU-Parent, MarianneTI-Glutathione: Antioxidant Properties Dedicated to Nanotechnologies, *Antioxidants* **2018**, *7*.
- [124] K. Aquilano, S. Baldelli, M. R. Ciriolo, *Frontiers in Pharmacology* **2014**, *5*.
- [125] A. Bansal, M. C. Simon, *Journal of Cell Biology* **2018**, *217*, 2291.
- [126] S. P. Hadipour Moghaddam, M. Yazdimamaghani, H. Ghandehari, *Journal of Controlled Release* **2018**, *282*, 62.
- [127] J. Niu, R. M. Straubinger, D. E. Mager, *Clinical Pharmacology & Therapeutics* **2019**, *105*, 1395.
- [128] S. Shakeel, S. Karim, A. Ali, *Journal of Chemical Technology & Biotechnology* **2006**, *81*, 892.
- [129] E. Cesaro, A. P. Falanga, R. Catapano, F. Greco, S. Romano, N. Borbone, A. Pastore, M. Marzano, F. Chiurazzi, S. D'Errico, G. Piccialli, G. Oliviero, P. Costanzo, M. Grosso, *PLOS ONE* **2022**, *17*, e0266090.
- [130] N. Köhler, D. A. Ruess, R. Kesselring, R. Zeiser, *Frontiers in Immunology* **2021**, *12*.
- [131] A. Verde, M. Mangini, S. Managò, C. Tramontano, I. Rea, D. Boraschi, P. Italiani, A. C. De Luca, *Front. Immunol.* **2021**, *12*, 758410.
- [132] J. Cao, T. Sun, K. T. V. Grattan, *Sensors and Actuators B: Chemical* **2014**, *195*, 332.
- [133] G. M. A.-M. Das StefanoAU-Mangini, MariaAU-De Luca, Anna C. TI-Biosensing Using SERS Active Gold Nanostructures, *Biosensing Using SERS Active Gold Nanostructures* **2021**, *11*.
- [134] N. S. White, R. J. Errington, *Advanced Drug Delivery Reviews* **2005**, *57*, 17.
- [135] S. Managò, G. Zito, A. Rogato, M. Casalino, E. Esposito, A. C. De Luca, E. De Tommasi, *ACS Appl. Mater. Interfaces* **2018**, *10*, 12406.
- [136] L. Woythe, P. Madhikar, N. Feiner-Gracia, C. Storm, L. Albertazzi, *ACS Nano* **2022**, *16*, 3785.
- [137] A. Schroeder, D. A. Heller, M. M. Winslow, J. E. Dahlman, G. W. Pratt, R. Langer, T. Jacks, D. G. Anderson, *Nature Reviews Cancer*

2012, *12*, 39.

- [138] D. Gast, S. Riedle, H. Kiefel, S. S. Mürköster, H. Schäfer, M. K. E. Schäfer, P. Altevogt, *Experimental Cell Research* **2008**, *314*, 2411.
- [139] J.-J. Zhang, M.-M. Gu, T.-T. Zheng, J.-J. Zhu, *Anal. Chem.* **2009**, *81*, 6641.
- [140] S. Wang, A. Wang, Y. Ma, Q. Han, Y. Chen, X. Li, S. Wu, J. Li, S. Bai, J. Yin, *Biomater. Sci.* **2021**, *9*, 774.
- [141] A. Baseer, A. Koenneke, J. Zapp, S. A. Khan, M. Schneider, *Macromolecular Chemistry and Physics* **2019**, *220*, 1900260.
- [142] P. Chen, N. T. Tran, X. Wen, Q. Xiong, B. Liedberg, *ACS Sens.* **2017**, *2*, 235.
- [143] N. A. Metheny, B. J. Stewart, L. Smith, Hua Yan, M. Diebold, R. E. Clouse, *JPEN J Parenter Enteral Nutr* **1997**, *21*, 279.
- [144] D. Chenthamara, S. Subramaniam, S. G. Ramakrishnan, S. Krishnaswamy, M. M. Essa, F.-H. Lin, M. W. Qoronfleh, *Biomaterials Research* **2019**, *23*, 20.
- [145] P. Jani, G. W. Halbert, J. Langridge, A. T. Florence, *Journal of Pharmacy and Pharmacology* **1989**, *41*, 809.
- [146] W. Yu, R. Liu, Y. Zhou, H. Gao, *ACS Cent. Sci.* **2020**, *6*, 100.
- [147] H. Luo, L. Kong, F. Zhang, C. Huang, J. Chen, H. Zhang, H. Yu, S. Zheng, H. Xu, Y. Zhang, L. Deng, G. Chen, H. A. Santos, W. Cui, *Advanced Functional Materials* **2021**, *31*, 2101262.
- [148] C. Cha, J. Oh, K. Kim, Y. Qiu, M. Joh, S. R. Shin, X. Wang, G. Camci-Unal, K. Wan, R. Liao, A. Khademhosseini, *Biomacromolecules* **2014**, *15*, 283.
- [149] S. Van Vlierberghe, *Journal of Materials Science* **2016**, *51*, 4349.
- [150] F. Tian, L. Cai, C. Liu, J. Sun, *Lab Chip* **2022**, *22*, 512.
- [151] V. Balasubramanian, A. Domanskyi, J.-M. Renko, M. Sarparanta, C.-F. Wang, A. Correia, E. Mäkilä, O. S. Alanen, J. Salonen, A. J. Airaksinen, R. Tuominen, J. Hirvonen, M. Airavaara, H. A. Santos, *Biomaterials* **2020**, *227*, 119556.
- [152] J. P. Martins, D. Liu, F. Fontana, M. P. A. Ferreira, A. Correia, S. Valentino, M. Kemell, K. Moslova, E. Mäkilä, J. Salonen, J. Hirvonen, B. Sarmiento, H. A. Santos, *ACS Appl. Mater. Interfaces* **2018**, *10*, 44354.
- [153] John F. Reinus, Douglas Simon, *Gastrointestinal anatomy and physiology: The essentials*, Wiley-Blackwell.
- [154] A. J. Coupe, S. S. Davis, I. R. Wilding, *Pharmaceutical Research* **1991**, *8*, 360.
- [155] S. Buhmann, C. Kirchhoff, R. Ladurner, T. Mussack, M. F.

- Reiser, A. Lienemann, *European Radiology* **2007**, *17*, 669.
- [156] S. Tiburcius, K. Krishnan, L. Jose, V. Patel, A. Ghosh, C. I. Sathish, J. Weidenhofer, J.-H. Yang, N. M. Verrills, A. Karakoti, A. Vinu, *Nanoscale* **2022**, *14*, 6830.
- [157] C. G. Bavnhøj, M. M. Knopp, C. M. Madsen, K. Löbmann, *International Journal of Pharmaceutics: X* **2019**, *1*, 100008.
- [158] P. Altevogt, A. Ben-Ze'ev, N. Gavert, U. Schumacher, H. Schäfer, S. Sebens, *Int. J. Cancer* **2020**, *147*, 3292.
- [159] R. E. Hewitt, A. McMarlin, D. Kleiner, R. Wersto, P. Martin, M. Tsoskas, G. W. H. Stamp, W. G. Stetler-Stevenson, *The Journal of Pathology* **2000**, *192*, 446.
- [160] M. Hekmati, Y. Ben-Shaul, S. Polak-Charcon, *Cell Differentiation and Development* **1990**, *31*, 207.
- [161] T. Lea, In *The Impact of Food Bioactives on Health: in vitro and ex vivo models* (Eds.: Verhoeckx, K.; Cotter, P.; López-Expósito, I.; Kleiveland, C.; Lea, T.; Mackie, A.; Requena, T.; Swiatecka, D.; Wichers, H.), Springer International Publishing, Cham, **2015**, pp. 103–111.
- [162] C. Pontier, J. Pachot, R. Botham, B. Lenfant, P. Arnaud, *Journal of Pharmaceutical Sciences* **2001**, *90*, 1608.
- [163] S. Hua, *Front Pharmacol* **2020**, *11*, 524.
- [164] M. Terracciano, L. Stefano, C. Tortiglione, A. Tino, I. Rea, *Adv. Biosys.* **2019**, *3*, 1800247.
- [165] S. Silletti, M. Yebra, B. Perez, V. Cirulli, M. McMahon, A. M. P. Montgomery, *Journal of Biological Chemistry* **2004**, *279*, 28880.
- [166] H. Kiefel, S. Bondong, J. Hazin, J. Ridinger, U. Schirmer, S. Riedle, P. Altevogt, *Cell Adh Migr* **2012**, *6*, 374.
- [167] A. P. Falanga, V. Cerullo, M. Marzano, S. Feola, G. Oliviero, G. Piccialli, N. Borbone, *Bioconjugate Chem.* **2019**, *30*, 572.
- [168] J. S. Suk, Q. Xu, N. Kim, J. Hanes, L. M. Ensign, *Advanced Drug Delivery Reviews* **2016**, *99*, 28.
- [169] F. Kunc, V. Balhara, A. Brinkmann, Y. Sun, D. M. Leek, L. J. Johnston, *Anal. Chem.* **2018**, *90*, 13322.
- [170] F. Kunc, O. Kodra, A. Brinkmann, G. P. Lopinski, L. J. Johnston, *Nanomaterials* **2020**, *10*.
- [171] J. Middelburg, K. Kemper, P. Engelberts, A. F. Labrijn, J. Schuurman, T. van Hall, *Cancers* **2021**, *13*.
- [172] Y.-J. Kwon, E.-B. Seo, A. J. Jeong, S.-H. Lee, K. H. Noh, S. Lee, C.-H. Cho, C.-H. Lee, H. M. Shin, H.-R. Kim, H.-G. Moon, S.-K. Ye,

BMC Cancer **2022**, *22*, 852.